Production of light nuclei and antinuclei in Pb–Pb collisions at the LHC

Dissertation
zur Erlangung des Doktorgrades
der Naturwissenschaften

vorgelegt beim Fachbereich Physik
der Johann Wolfgang Goethe-Universität
in Frankfurt am Main

von

Esther Bartsch
aus Frankfurt am Main

Frankfurt 2021

(D 30)

Vom Fachbereich Physik der Johann Wolfgang Goethe-Universität als Dissertation angenommen.

Dekan:	Prof. Dr. Harald Appelshäuser
Gutachter:	Prof. Dr. Harald Appelshäuser PD Dr. Benjamin Dönigus

Datum der Disputation: 21.02.2022

Nobody ever figures out what life is all about, and it doesn't matter. Explore the world. Nearly everything is really interesting if you go into it deeply enough.

– **Richard P. Feynman**

Zusammenfassung

Das Feld der Hochenergie-Schwerionenforschung hat sich der Untersuchung des Quark-Gluon-Plasmas (QGP) gewidmet. Ein QGP ist ein sehr heißer und dichter Materiezustand, der kurz nach dem Urknall für einige Mikrosekunden das Universum füllte. Unter diesen extremen Bedingungen sind die fundamentalen Bausteine der Materie – die Quarks und Gluonen – quasi frei, also nicht in Hadronen eingeschlossen, wie es unter normalen Bedingungen der Fall ist. Hadronen sind Teilchen, die aus Quarks und Gluonen bestehen. Die bekanntesten Hadronen sind Protonen und Neutronen, die Bestandteile von Atomkernen, aus denen, zusammen mit Elektronen, die gesamte bekannte Materie aufgebaut ist. Quarks und Gluonen unterliegen der starken Wechselwirkung. Die Theorie, die diese beschreibt, ist die Quantenchromodynamik, welche ein Teil des Standardmodells der Teilchenphysik ist.

Die einzige bekannte Möglichkeit, ein QGP im Labor zu erzeugen, um es zu untersuchen, sind ultrarelativistische Schwerionenkollisionen. Ein QGP existiert nur sehr kurz, da es aufgrund von hohen inneren Druckgradienten schnell expandiert und abkühlt. Es kann deshalb nicht direkt beobachtet werden. Es können jedoch zahlreiche Observablen im Endzustand der Kollision, wie die nach der Kollision in den Detektoren registrierten Teilchen und deren Eigenschaften, gemessen werden. Indem man die Daten mit theoretischen Modellen vergleicht, können dann Rückschlüsse auf die Eigenschaften des QGP gezogen werden. Nach heutigem Wissensstand geht man davon aus, dass bei hohen Kollisionsenergien bei der kritischen Temperatur T_c ein *Crossover* Phasenübergang von einem QGP zu einem Hadrongas stattfindet. Dies bedeutet, dass sich die Eigenschaften des Systems beim Phasenübergang nicht abrupt, sondern kontinuierlich ändern. Kurz darauf, eventuell auch gleichzeitig, beim Erreichen der chemischen Ausfriertemperatur T_ch, hören alle inelastischen Wechselwirkungen zwischen den Teilchen auf und die Anzahl der verschiedenen Teilchensorten ändert sich nicht mehr. Kühlt das Medium weiter ab, wird die kinetische Ausfriertemperatur T_kin erreicht, bei der auch die elastischen Interaktionen zwischen den Teilchen ein Ende finden und die Impulsspektren festgelegt sind.

Ein QGP entsteht, wenn man hochenergetische, genauer gesagt ultrarelativistische, schwere Ionen, wie zum Beispiel ^{208}Pb-Kerne, aufeinander prallen lässt. Dies geschieht am CERN, dem größten Kernforschungszentrum der Welt, wo ungefähr einen Monat pro Jahr Pb–Pb Kollisionen aufgezeichnet werden, während das restliche Jahr über Proto-

nen zur Kollision gebracht werden. Der Teilchenbeschleuniger, welcher die Protonen und Pb-Kerne beschleunigt und zur Kollision bringt, heißt *Large Hadron Collider* (LHC). Er ist mit einem Umfang von 27 km der größte der Welt und erreichte die bis heute höchstmöglichen Schwerpunktsenergien von 5,02 TeV pro Nukleonpaar in Pb–Pb Kollisionen und 13 TeV in Proton-Proton (pp) Kollisionen. Bei einer einzigen Pb–Pb Kollision am LHC werden mehrere Tausend Teilchen und Antiteilchen erzeugt. Das dedizierte Experiment zur Untersuchung von Schwerionenkollisionen am LHC ist ALICE. ALICE ist mit mehreren Teilchendetektoren ausgerüstet, die innerhalb eines großen Magneten konzentrisch um den Kollisionspunkt herum angeordnet sind und verschiedene Techniken verwenden, um möglichst effizient über einen breiten Impulsbereich tausende Teilchenspuren gleichzeitig zu messen und dabei die Teilchen zu identifizieren.

Unter den produzierten Teilchen befinden sich auch leichte Atomkerne, wenngleich diese nur sehr selten erzeugt werden. Die Anzahl der produzierten Teilchen pro Teilchensorte hängt nämlich von deren Masse ab. In Pb–Pb Kollisionen am LHC sinkt die Anzahl der produzierten (Anti)kerne exponentiell um einen Faktor $\frac{1}{330}$ bei Hinzufügen jedes weiteren Protons oder Neutrons. In pp Kollisionen beträgt dieser Faktor sogar $\frac{1}{1000}$. Die Menge an produzierten Teilchen pro Spezies stellt Informationen über den Produktionsmechanismus beim Übergang vom QGP zum Hadrongas zur Verfügung. Hierbei sind leichte (Anti)kerne von besonderem Interesse, da ihre Größe einen signifikanten Anteil der Größe des erzeugten QGP darstellt und zugleich ihre Bindungsenergie bis zu zwei Größenordnungen kleiner ist als die Temperaturen, die bei der Erzeugung der Hadronen vorherrschen. Es ist bis heute noch nicht verstanden, wie leichte (Anti)kerne bei diesen Bedingungen erzeugt werden und überleben können. Es gibt zwei Klassen von Modellen, welche die Produktion leichter (Anti)kerne beschreiben, das statistische Hadronisierungsmodell (SHM), welches auch thermisches Modell genannt wird, und das Koaleszenzmodell. Beim SHM werden die (Anti)kerne während des chemischen Ausfrierens im statistischen Gleichgewicht mit allen anderen Teilchen produziert und ihre Produktion hängt exponentiell von der Teilchenmasse ab. Beim Koaleszenzmodell werden die Kerne während des kinetischen Ausfrierens, bei manchen Varianten auch schon vorher, von Protonen und Neutronen geformt, welche sich im Orts- und Impulsraum nah beieinander befinden. Die Produktion hängt hier von der Größe des Kerns und des QGPs ab.

Für diese Arbeit wurden ungefähr 270 Millionen Pb–Pb Kollisionen bei einer Schwerpunktsenergie von 5,02 TeV, die von der ALICE Kollaboration im November 2018 aufgezeichnet wurden, analysiert. Es wurde die Produktion von (Anti)triton und (Anti)^{4}He-Kernen untersucht. Wegen ihrer großen Masse werden beide Kerne – jedoch besonders

(Anti)^{4}He – sehr selten produziert, bei weitem nicht bei jeder Kollision. Anti^{4}He ($^4\overline{\mathrm{He}}$) ist der schwerste Antikern, der jemals gemessen wurde. Aufgrund dieser Seltenheit ist die Größe des zur Verfügung stehenden Datensatzes entscheidend. Deshalb wurde für die Analyse, die ursprünglich in dem Pb–Pb Datensatz von 2015 durchgeführt worden war, letztendlich der Datensatz von 2018 verwendet. Im gesamten Datensatz von 2015 wurden nur 16 $^4\overline{\mathrm{He}}$-Kerne identifiziert. Der Datensatz von 2018 enthält ungefähr zehn mal so viele zentrale Kollisionen. Dies ermöglichte es, das erste jemals gemessene $^4\overline{\mathrm{He}}$-Transversalimpulsspektrum zu extrahieren. Auch für (Anti)triton und ^{4}He wurden Transversalimpulsspektren bestimmt.

Das entscheidende Kriterium dieser Analyse ist die Teilchenidentifikation, um die leichten (Anti)kerne von den signifikant öfter produzierten leichteren Teilchen zu unterscheiden. In der Spurendriftkammer (auch: *Time Projection Chamber*, TPC), dem wichtigsten Spurfindungsdetektor von ALICE, wird der spezifische Energieverlust der Teilchen pro Wegstrecke in einem Driftgas bestimmt. Bei niedrigen Impulsen sind die unterschiedlichen Teilchensorten in der TPC getrennt. Ab ca. $2\,\mathrm{GeV}/c$ jedoch befinden sich die Teilchen im relativistischen Anstieg und der Energieverlust der verschiedenen Teilchensorten gleicht sich an, sodass sie in der TPC nicht mehr voneinander zu unterscheiden sind. Deshalb wird zusätzlich die Flugzeitmessung des *Time-of-Flight* (TOF) Detektors verwendet, nachdem die Teilchen in der TPC vorselektiert wurden. Aus der Flugzeit und der Impulsmessung aus der Krümmung der Teilchenspuren im Magnetfeld kann die Teilchenmasse berechnet werden. In der Massenmessung des TOF-Detektors sitzt das (Anti)tritonsignal auf einem riesigen Untergrund, der sich über den gesamten Massenbereich erstreckt. Der Ursprung dieses Untergrundes sind Spuren, die dem falschen TOF-Signal zugeordnet werden, sodass sich aus einem nicht zusammengehörenden Paar aus Impuls- und Zeitmessung eine unphysikalische Masse ergibt. Aus diesem Grund konnten die Transversalimpulsspektren der (Anti)tritonen nur bis ungefähr $3\,\mathrm{GeV}/c$ bestimmt werden.

(Anti)^{4}He wird noch um einiges seltener produziert als (Anti)triton, allerdings ist es zweifach geladen. Da der spezifische Energieverlust quadratisch von der Ladung abhängt, ist er viermal so groß wie für einfach geladene Teilchen. (Anti)^{4}He liegt also in der TPC gut von den einfach geladenen Teilchen getrennt. Eine TOF-Messung wird jedoch trotzdem benötigt, um (Anti)^{4}He von (Anti)^{3}He zu separieren. Die (Anti)^{4}He-Transversalimpulsspektren konnten bis $6\,\mathrm{GeV}/c$ bestimmt werden.

An die Transversalimpulsspektren von (Anti)tritonen und (Anti)^{4}He wurde ein *Blast-Wave* (BW) Modell angepasst. Das BW-Modell ist ein vereinfachter hydrodynamischer Ansatz, der stationäre thermische Quellen annimmt, die in radiale Richtung geschoben

werden und so einen expandierenden Feuerball, das QGP, darstellen. Damit lassen sich die Transversalimpulsspektren aller Teilchen aus Schwerionenkollisionen mit nur drei freien Parametern, der kinetischen Ausfriertemperatur T_{kin}, der Expansionsgeschwindigkeit des Feuerballs β und einem Skalierungsparameter, beschreiben. Für alle gemessenen Spektren wurden T_{kin} und β bestimmt. Zusätzlich wurde die angepasste Funktion dafür verwendet, die Spektren zu hohen und niedrigen Transversalimpulsen (p_{T}) zu extrapolieren und durch Integration über p_{T} die Gesamtzahl an produzierten Teilchen $\mathrm{d}N/\mathrm{d}y$ sowie den mittleren Transversalimpuls $\langle p_{\mathrm{T}} \rangle$ zu bestimmen. In zentralen Pb–Pb Kollisionen werden ca. zwei bis drei Antitritonen pro 10.000 Kollisionen produziert. Ein $^4\overline{\mathrm{He}}$ wird sogar nur in jeder millionsten Kollision erzeugt. Das $\langle p_{\mathrm{T}} \rangle$ steigt mit der Teilchenmasse und ist daher für (Anti)^{4}He größer als für (Anti)triton.

Die (Anti)tritonspektren wurden auch mit einer vorläufigen ALICE Messung des (Anti)^{3}He verglichen. Die Spektren beider Teilchen stimmen gut miteinander überein, was aufgrund ihrer ähnlichen Masse auch zu erwarten ist.

Eine kombinierte Blast-Wave-Anpassung an die Transversalimpulsspektren leichter Teilchen (Pion, Kaon) bis hin zu leichten Kernen (Proton, Deuteron, Triton, ^{3}He und ^{4}He) wurde ebenfalls durchgeführt. Alle Spektren, inklusive der leichten Kerne, konnten sehr gut mit einem Satz von Parametern beschrieben werden. Es ergab sich eine kinetische Ausfriertemperatur von $T_{\mathrm{kin}} = (98 \pm 1)\,\mathrm{MeV}$ und eine mittlere Expansionsgeschwindigkeit des Feuerballs von $\langle \beta \rangle = 0.661 \pm 0.003$.

Die Gesamtzahl an produzierten Teilchen $\mathrm{d}N/\mathrm{d}y$ wurde für verschiedene Teilchensorten mit verschiedenen Varianten des thermischen Modells verglichen. Die $\mathrm{d}N/\mathrm{d}y$ werden über neun Größenordnungen hinweg gut beschrieben, von oft produzierten leichten Pionen bis hin zu den seltenen (Anti)^{4}He. Es ergab sich bei fast allen Modellvarianten eine chemische Ausfriertemperatur von etwa 150 MeV. Es ist recht bemerkenswert, dass die Produktion von (Anti)^{4}He, obwohl es nur in einer von einer Millionen Kollisionen erzeugt wird, trotzdem einer statistischen Verteilung folgt.

Das Verhältnis des $\mathrm{d}N/\mathrm{d}y$ von Kernen zu dem $\mathrm{d}N/\mathrm{d}y$ von Protonen im gleichen Kollisionssystem und bei gleicher Schwerpunktsenergie kann ebenfalls untersucht werden, um Rückschlüsse auf die Produktion der Kerne zu ziehen. Dies ist naheliegend, da Kerne aus Protonen und Neutronen zusammengesetzt sind. Neutronen können zwar von ALICE nicht gemessen werden, man geht aber davon aus, dass Protonen und Neutronen in gleicher Menge erzeugt werden. Das Verhältnis wurde für $A = 3$ Kerne, also (Anti)tritonen und (Anti)^{3}He, für pp, p–Pb und Pb–Pb Kollisionen bei verschiedenen Energien untersucht. Für die verschiedenen Kollisionssysteme und Schwerpunktsenergien wurde die mittlere Anzahl an produzierten geladenen Teilchen $\langle \mathrm{d}N_{\mathrm{ch}}/\mathrm{d}\eta \rangle$ angegeben, welche mit

Größe des Kollisionssystems und der Kollisionsenergie steigt. Das besagte Verhältnis wurde dann in Abhängigkeit von $\langle \mathrm{d}N_{\mathrm{ch}}/\mathrm{d}\eta \rangle$ aufgetragen. Die Daten wurden mit den Vorhersagen von SHM und Koaleszenzmodell verglichen. Mit steigendem $\langle \mathrm{d}N_{\mathrm{ch}}/\mathrm{d}\eta \rangle$ steigt die Anzahl der produzierten Kerne pro Protonen zunächst an, saturiert dann aber bei großen Kollisionssystemen. Dieser Trend wird sowohl vom SHM, als auch vom Koaleszenzmodell gut beschrieben und es lässt sich anhand dessen keine Unterscheidung zwischen den Modellen vornehmen, geschweige denn eines ausschließen.

Letztendlich wurden noch die Koaleszenzparameter B_3 für (Anti)tritonen und B_4 für (Anti)^{4}He berechnet. Diese sind mit der Wahrscheinlichkeit verknüpft, einen Kern durch Koaleszenz zu formen. Die Koaleszenzparameter sind kleiner bei größerer Quellengröße und größer bei kleinerer Quellengröße. Dies ergibt Sinn, da bei einem kleineren Quellvolumen die Wahrscheinlichkeit, dass die Protonen und Neutronen sich soweit annähern, um einen Kern zu bilden, größer ist. Desweiteren sinkt die Wahrscheinlichkeit einen Kern zu bilden mit jedem hinzugefügten Nukleon, weshalb B_4 viel kleiner ist als B_3. B_3 und B_4 wurden ebenfalls mit dem SHM und dem Koaleszenzmodell verglichen. Die Datenpunkte liegen etwas näher am statistischen Hadronisierungsmodell, aber der Gesamtverlauf wird von beiden Modellen beschrieben.

Am Ende wird in einem Ausblick auf das kürzlich durchgeführte Upgrade der ALICE TPC eingegangen. In der nächsten, bald startenden Datennahmeperiode wird der LHC seine Kollisionsrate erheblich erhöhen, was es ermöglichen wird, mehr als 100 mal so viele Daten wie bisher aufzuzeichnen. Hiervon werden die in dieser Arbeit beschriebenen (Anti)triton- und (Anti)^{4}He-Analysen beachtlich profitieren. Um mit den erheblich höheren Kollisionsraten zurecht zu kommen, mussten einige Detektoren, unter anderem die TPC, maßgeblich erneuert werden. In den ersten beiden Datennahmeperioden wurde die TPC mit Vieldrahtproportionalkammern betrieben. Diese sind allerdings viel zu langsam für die geplanten Kollisionsraten. Deshalb wurden sie im Jahr 2019, während einer langen Betriebspause des LHC, durch Quadrupel-GEM (*Gas Electron Multiplier*) Folien basierte Auslesekammern ersetzt, welche eine kontinuierliche Auslese der TPC ermöglichen, was mit den Vieldrahtproportionalkammern nicht der Fall war. Da es sich um die erste jemals gebaute GEM TPC handelt, war ein umfangreiches Forschungs- und Entwicklungs- (F&E) Programm notwendig, um die GEM Auslesekammern zu charakterisieren und zu testen. Im Rahmen dieses F&E Programms wurden am Anfang dieser Promotion systematische Messungen an einer kleinen Test TPC mit Quadrupel-GEM Auslese, die extra zu diesem Zweck gebaut worden war, durchgeführt. Hierbei wurde der Rückfluss der bei der Gasverstärkung erzeugten Ionen in das Driftvolumen der TPC und die Energieauflösung mit verschiedenen GEM Folien Typen und unterschiedlicher

Anordnung gemessen. Das Ziel war, möglichst kleine Ionenrückflüsse bei möglichst guter Energieauflösung zu erreichen. Hierbei musste ein Kompromiss gefunden werden, da die beiden Größen sich gegenläufig verhalten. Es war jedoch möglich, mit mehreren GEM Konfigurationen Spannungseinstellungen zu identifizieren, bei denen beide Größen den gewünschten Anforderungen entsprachen.

Contents

1 Introduction

Shortly after the Big Bang a hot and dense medium filled the universe for a few microseconds. From this medium all matter we know today was created. This medium is called quark-gluon plasma, or short QGP. The high-energy heavy-ion physics community is devoted to the investigation of QGP, as heavy-ion collisions at ultrarelativistic energies are the unique possibility to create QGP in the laboratory. QGP only exists under extreme conditions under which the fundamental particles matter consists of – the quarks and gluons – are moving freely, they are deconfined. Under normal conditions, like in our every-day life, quarks and gluons are confined in hadrons. The most familiar hadrons are protons and neutrons, the nucleons atomic nuclei are built of. But a variety of many more hadrons exists of which most people never heard of. The theory that describes the interaction between quarks and gluons is called quantum chromodynamics (QCD), quarks and gluons are governed by the strong force.

In this chapter it will be discussed what happens to matter under extreme conditions and how these extreme conditions can be created in the lab. In addition, an overview of the theory that describes strongly-interacting matter will be given.

1.1 Quark-gluon plasma

Theory predicts at very high temperatures and/or densities a phase transition from the hadronic phase to a nearly free gas of quarks and gluons, the quark-gluon plasma. By considering an ideal gas in thermal equilibrium the phase transition and the QGP can be described by thermodynamics. Although this is only a static approximation which cannot describe the time evolution of the QGP, it proofed to be quite revealing.

There are phase transitions of different order. In our every-day life we are most familiar with the phase transitions of water [1]. The phase transitions in water at atmospheric pressure are of first order. First-order phase transitions are characterized by latent heat and that the two phases between which the transition takes place can coexist. In a first-order phase transition temperature, pressure and chemical potential of the system do not change at the phase boundary until the whole medium has changed the phase, the volume can increase though. The latent heat is a measure of the entropy difference of the

two systems and manifests itself in a discontinuity, a jump in the energy density. Phase transitions without a discontinuity in the energy density are not first order. The order of the phase transition is determined by the lowest-order derivative of the free energy which has a discontinuity at the phase boundary. At a second-order phase transition the second derivative of the free energy has a discontinuity. Phase transitions that have higher order than first are also called continuous phase transitions [2].

Figure 1.1 shows a schematic phase diagram of strongly-interacting matter. The y axis represents the temperature T, the x axis represents the baryochemical potential μ_B. The baryochemical potential is a measure for the net baryon density or in other words the matter-antimatter asymmetry. If the amount of matter and antimatter is equal, μ_B is zero.

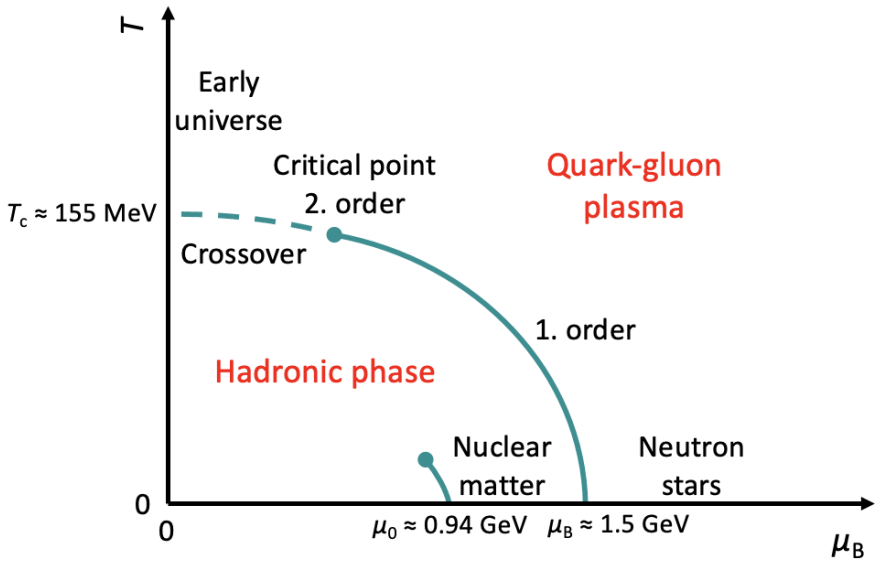

Figure 1.1: Schematic phase diagram of strongly-interacting matter.

At small temperature and baryochemical potential matter is in the hadronic phase. By compressing the matter (moving along the x axis) or heating up the vacuum (moving along the y axis) a transition to a quark-gluon plasma takes place. At low temperature the transition is believed to be first order, indicated by a solid line. With increasing temperature the discontinuity in the energy density becomes smaller until it becomes continuous and the first order phase transition eventually ends in a critical point of second order. Beyond the critical point at low baryochemical potential the phase transition could either be second order or a smooth crossover, indicated by the dashed line. The location of the critical point and whether the transition beyond is second order or a crossover

depends on the quark masses [3]. The experimentally accessible region could be on either side of the critical point. Experimentally a crossover is not favourable, as there are no clear changes, like a jump in the energy density, visible in the observables which makes it very difficult to draw conclusions about the phase transition and its order.

QGP at low temperatures and high baryon densities is expected to exist in the core of neutron stars, while QGP at high temperatures and low baryon densities is believed to have existed in the early universe for several microseconds after its creation in the Big Bang.

Nuclear matter is located on the x axis at zero temperature at a baryochemical potential of about 0.94 GeV which is the nucleon mass. Below this value at $T = 0$ there is vacuum. Indicated as solid line is the liquid-gas phase transition of nuclear matter which is a phase transition of first order [4]. At lower μ_B is the gas and at higher μ_B the liquid phase of nuclear matter, respectively. With higher temperatures the phase transition bends to slightly lower baryochemical potentials, as the nuclear matter can be excited. This phase transition then also ends in a point of second order.

Experimental results showed that the QGP rather behaves like a strongly interacting, nearly ideal fluid than a weakly interacting gas of quarks and gluons [5]. The time evolution of the system and how it changes in space can be described by hydrodynamics.

1.2 Heavy-ion collisions

A unique possibility to create a QGP in the laboratory are heavy-ion collisions. In a heavy-ion collision two heavy nuclei are smashed against each other with ultrarelativistic energies. In doing so, thousands of particles are created. These collisions can take place in collider or fixed-target mode. In collider mode two beams of heavy nuclei which are completely stripped off their electrons are accelerated in circles in opposite directions. When the desired energy is reached, the beams are crossed and the nuclei are brought to collision. The center-of-mass energy is the sum of both beam energies. In a collider experiment the detectors are installed more or less symmetrically in concentric cylinders around the collision point and the beam axis. Collisions at a collider are characterized by high center-of-mass energies and low baryochemical potential. Collider experiments probe the upper left region in the phase diagram of strongly-interacting matter.

In fixed-target mode a single beam of heavy nuclei stripped off their electrons is accelerated and directed on a fixed target which could for example be a thin gold foil. The center-of-mass energy in fixed-target mode only increases with the square root of the beam energy. In a fixed-target experiment the detectors are mainly located behind the

target and installed behind each other. A fixed-target collision is typically characterized by lower energies but high baryochemical potential. The lower right region in the phase diagram of strongly-interacting matter is probed.

1.2.1 Geometry of a heavy-ion collision

Not only the collision system, i.e. the type of nuclei that are collided, and the center-of-mass energy define the initial conditions of a heavy-ion collision but also the overlap of the two nuclei as illustrated in figure 1.2. The minimal distance between the centers of the two colliding nuclei is called impact parameter b. The impact parameter determines the centrality of a collision. The smaller the impact parameter, the more central is the collision. The impact parameter can have values between zero and two times the radius of the colliding nuclei ($0 < b < 2R$). The more nucleons are involved in the collision, so the more central the collisions is, the larger and long-lived is the created medium, the QGP. The nucleons that take part in the collision and interact with each other are called participants, the nucleons that are not interacting are called spectators. The maximal number of participants in a central collision is the sum of the mass numbers of the colliding ions, in case of ^{208}Pb$-^{208}$Pb it is 416.

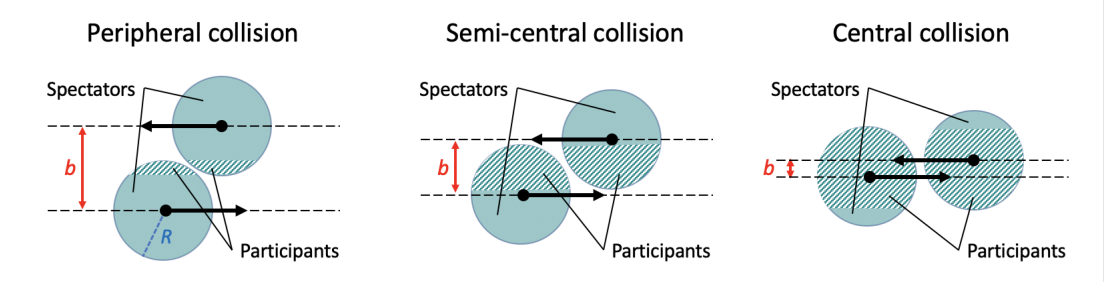

Figure 1.2: Illustration of the different centrality regions of a heavy-ion collision.

The probability for a collision with a certain impact parameter is linearly increasing with increasing impact parameter, peripheral collisions are much more likely than central collisions. This is illustrated in figure 1.3, collisions of a centrality with impact parameter b are realized on a circle with radius b. The probability of a collision with impact parameter zero, and thus the number of events, is going towards zero. At an impact parameter of two times the nuclear radius the number of events drops to zero again.

Neither the impact parameter nor the number of participants can be measured in the experiment. Therefore Glauber Monte Carlo (MC) simulations are employed to connect these geometric quantities with observables that can be measured [6]. In the Glauber

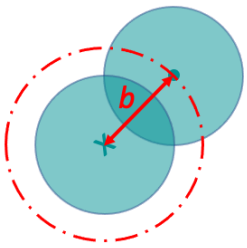

Figure 1.3: Illustration of the impact parameter of a heavy-ion collision. One nucleus is moving out of the paper plane, one is moving into the paper plane. Events with a given impact parameter b are realized on the dashed circle.

model it is assumed that the nucleons inside the nucleus are hard spheres which move along parallel straight trajectories, being treated as uncorrelated free particles. They are distributed according to a nuclear-density function, for example the Woods-Saxon density-distribution, which is a sphere with a diffuse edge. Two nuclei are collided with a certain displacement, the impact parameter. The nucleons interact with the nucleons of the other nucleus according to cross sections that are known from elementary processes. The exact position of the nucleons in the nucleus is subject to event-by-event fluctuations. In a Monte Carlo simulation nuclei are collided and the number of participants N_{part}, the number of spectators N_{spec} and also the number of binary collisions of the participants N_{coll}, as the nucleons can interact several times, for different impact parameters are calculated. Using N_{part} and N_{coll} the distribution of events as a function of produced particles in the collision can be estimated which provides a connection to experimentally measurable quantities.

There are two different methods to estimate the centrality experimentally. Either to measure the spectator nucleons, that move on along the beam axis or only slightly deflected, or to measure the produced particles, for example the charged-particle multiplicity N_{ch} [7, 8]. The number of produced charged particles increases in good approximation monotonically with collision centrality. Thus the number of events can be plotted versus the signal of a detector that is directly proportional to the number of produced particles in the collision. In figure 1.4 this is as an example shown for the ALICE V0 detector. The data is fitted with a Glauber Monte Carlo calculation. The number of events is larger at small amplitudes, as the peripheral collisions are more frequent, and is then decreasing to higher V0 amplitudes. The total integral of the distribution is then divided into centrality classes or intervals according to the area under the curve. The 5 % of the area with the highest V0 amplitude represent the 0-5 % most central collisions and so

on. This can be done for different detectors and compared. It is of course not an exact determination of the impact parameter, that defines the centrality, but it is nevertheless a good experimental approximation.

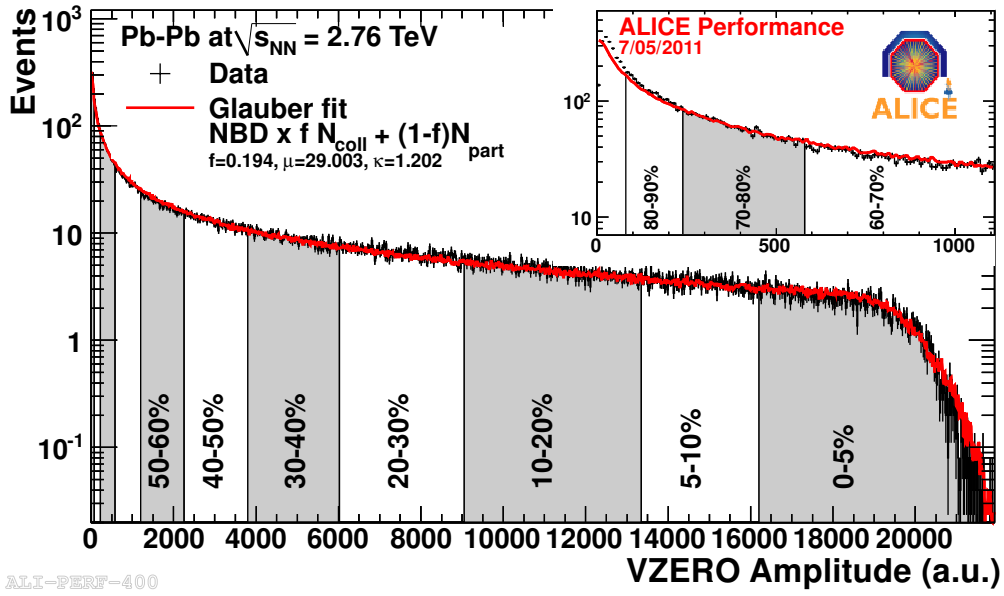

Figure 1.4: Number of events versus V0 amplitude compared to a Glauber MC fit. The area below the distribution is divided in centrality intervals [6, 9].

1.2.2 Evolution of a heavy-ion collision

A heavy-ion collision passes through several consecutive phases, which are characterized through different physical processes. Figure 1.5 shows the chronological sequence of a heavy-ion collision. On the left the two ultrarelativistic and thus Lorentz-contracted nuclei are approaching each other. After the collision, which is characterized through initial hard scattering of the partons, a short pre-equilibrium phase occurs, before thermodynamic equilibrium sets in and a hot and dense medium, the QGP, is created. The QGP features an energy density several times the normal nuclear matter density and a temperature above 150 MeV, which corresponds to about 10^{12} K. In the QGP quarks and gluons move freely, they are deconfined. Because of the very high inner pressure it expands and at the same time cools down until the critical temperature is reached, the quarks combine, and hadronization takes place. The lifetime of the QGP is very short in the order of 3 to 4 fm/c, which corresponds to 10^{-23} s, so it can only be examined indirectly. After the freeze-out the hadrons can be observed in the detectors creating

thousands of tracks per collision.

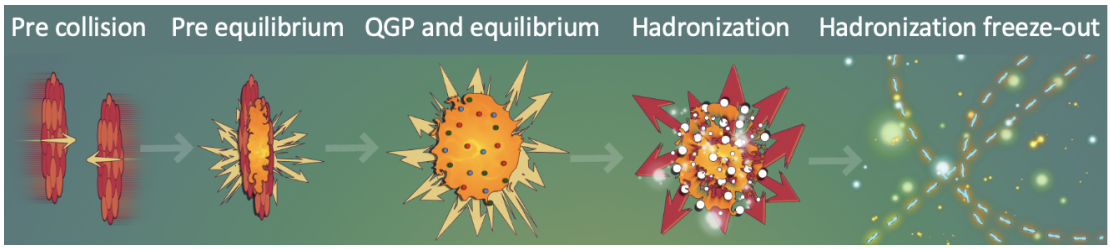

Figure 1.5: Chronological sequence of a heavy-ion collision [8].

Figure 1.6 shows the space-time evolution of a heavy-ion collision at ultrarelativistic energies in the center-of-mass system. The horizontal axis represents the space dimension z in beam direction, while the vertical axis represents the time dimension t. The collision takes place at the origin of the coordinate system at $z = t = 0$, so the lower half is before and the upper half after the collision. One ion is moving from the left ($z < 0$) to the right, and the other ion is moving from the right ($z > 0$) to the left. The diagonal lines where $z^2 = t^2$ along the trajectory of the ions define the light cone. Inside the light cone at $t > 0$ particle production occurs. Directly after the collision the system is in a pre-equilibrium phase, marked in gray in the figure. After about $1\,\mathrm{fm}/c$ thermodynamical equilibrium is reached and a QGP is formed. The system expands and cools down and when a critical temperature T_c is reached, a phase transition to a hadron gas occurs. This phase transition could be first order characterized through a mixed phase or a fast crossover indicated by the yellow area in the figure. In case of a first-order phase transition the system stays at T_c until the phase transition is completed, in case of a crossover the system will only be at T_c for a very short period of time. The blue area represents a gas of hadrons that still interact with each other while the system further expands. At the chemical freeze-out temperature T_ch, which could be at T_c or a bit later, the hadron yields are fixed, so there are no inelastic interactions between the hadrons anymore. Finally, at the kinetic freeze-out temperature T_kin also the momentum spectra of the particles are fixed, the mean free path has become that large that the elastic interactions stop and the hadrons stream freely in the detectors. Around the time axis is the midrapidity region, where the particles are produced transverse to the original direction of the colliding ions. As the system expands ultrarelativistically the points in time where phase changes happen are along hyperbolas. This is due to the time dilatation. The phase transition happens at the same eigentime for the system but from the center-of-mass system it happens later in an away-moving part of the source.

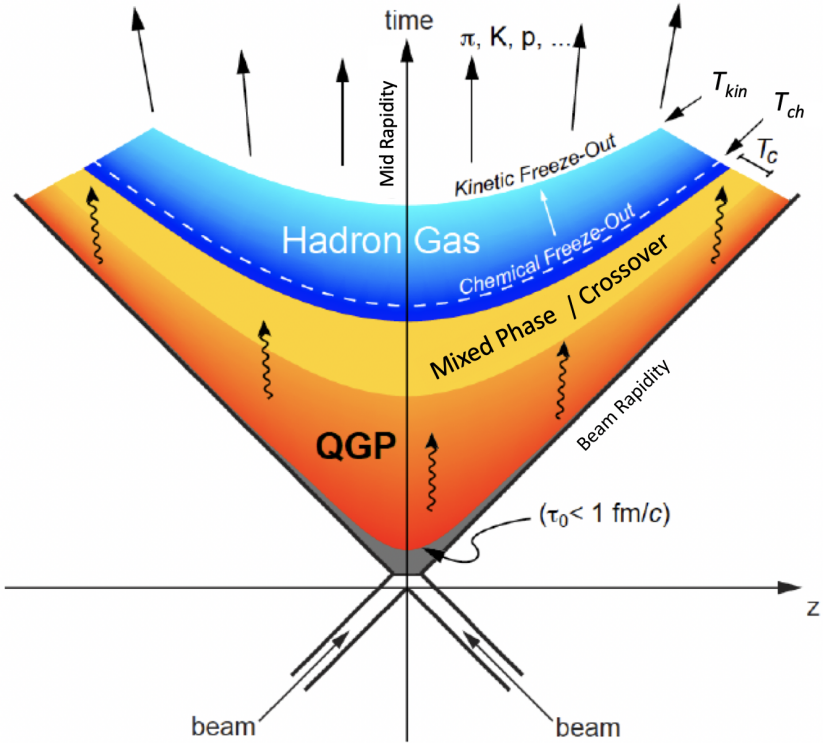

Figure 1.6: Space-time diagram of a heavy-ion collision in the center-of-mass system [10].

1.2.3 Collective behaviour and Blast-Wave model

During the expansion of the fireball the particles experience a strong collective flow field in radial direction caused by pressure gradients transverse to the beam. This flow field leads to a characteristic shape of the transverse-momentum spectra of all particles. As the particles are boosted with a common flow velocity, the mean momentum of the different particle species is shifted to higher values for heavier particles. This is called mass ordering. A simplified hydrodynamic approach that can describe the particles' p_{T} spectra in heavy-ion collisions with just three free parameters is the Blast-Wave (BW) model [10, 11]. The free parameters are the kinetic freeze-out temperature T_{kin}, a velocity parameter β_{max}, measured in units of the light speed, and a scale parameter n. The BW model assumes thermal sources that are boosted in radial direction with a velocity profile for $0 < r < R$ [11]:

$$\beta_r = \beta_{\mathrm{max}} \left(\frac{r}{R} \right)^n \tag{1.1}$$

$\beta_{\max}$ is the velocity at the surface of the isotropically expanding fireball where the radius is R. In the center ($r = 0$) the velocity is zero and in between it is behaving according to the profile. If a linear profile is assumed, n is fixed to one, however, with n as a free parameter a better description of the spectra can be obtained. The spectral shape is a superposition of thermal components, that are boosted with $\rho = 1/\tanh \beta_r$ [11]:

$$\frac{\mathrm{d}N}{m_{\mathrm{T}}\,\mathrm{d}m_{\mathrm{T}}} \propto \int_0^R r\,\mathrm{d}r\, m_{\mathrm{T}}\, I_0\left(\frac{p_{\mathrm{T}} \sinh\rho}{T_{\mathrm{kin}}}\right) K_1\left(\frac{m_T \cosh\rho}{T_{\mathrm{kin}}}\right) \tag{1.2}$$

I_0 and K_1 are Bessel functions and $m_T = \sqrt{p_{\mathrm{T}}^2 + m^2}$.

Some publications also state $\langle\beta\rangle$ instead of $\beta_{\max}$. It can be calculated from the fit parameters according to:

$$\langle\beta\rangle = \frac{2}{2+n} \cdot \beta_{\max} \tag{1.3}$$

In figure 1.7 the p_{T} spectra of different particle species measured in Pb–Pb collisions are fitted with a combined Blast-Wave fit with a common set of parameters. Included are also light nuclei (d und ^{3}He) while triton and ^{4}He are still missing. The fit describes the data quite well with a mean collective radial flow velocity $\langle\beta\rangle = 0.63 \pm 0.01$, a kinetic freeze-out temperature $T_{\mathrm{kin}} = 113 \pm 12\,\mathrm{MeV}$ and $n = 0.72 \pm 0.03$ [12]. A clear mass ordering can also be observed, i. e. the maximum of the peak is shifted to higher momenta with higher particle mass. The two lower panels show the deviation of the data from the fit.

T_{kin} and $\beta_{\max}$ are usually anticorrelated. In more central collisions, where the QGP is assumed to be larger, the fits yield larger velocities $\beta_{\max}$ and lower kinetic freeze-out temperatures. So, the medium seems to freeze out later, if it is larger.

Blast-Wave fits are also used to extrapolate p_{T} spectra to the not measured low- and high-p_{T} region, if one wants to determine the p_{T}-integrated production yield.

1.3 Quantum chromodynamics and strongly-interacting matter

Quantum chromodynamics (QCD) is the theory that describes the interaction between quarks and gluons. There are six quark flavors (u, d, c, s, t, b) and three color charges (red, blue, green) together with the corresponding antiflavors ($\overline{\mathrm{u}}$, $\overline{\mathrm{d}}$, $\overline{\mathrm{c}}$, $\overline{\mathrm{s}}$, $\overline{\mathrm{t}}$, $\overline{\mathrm{b}}$) and anticolors ($\overline{\mathrm{red}}$, $\overline{\mathrm{blue}}$, $\overline{\mathrm{green}}$). Each quark carries a color charge, while each gluon carries one color and one anticolor of a different kind, so that they always carry a net color charge. However only color neutral objects exist in nature. Color neutrality is obtained by

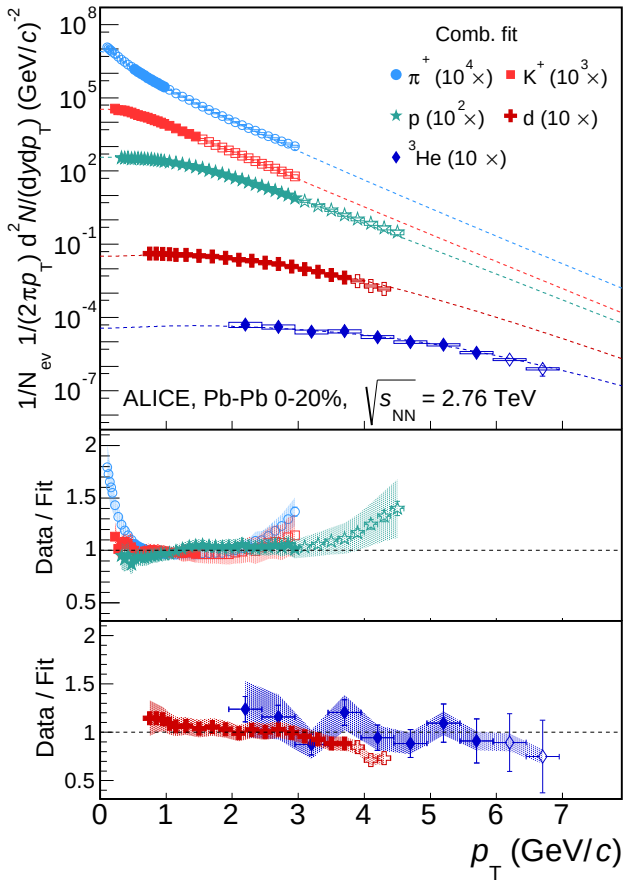

Figure 1.7: Combined Blast-Wave fit of the p_{T} spectra of different particle species including light nuclei with a common set of parameters [12].

combining three different colors, three different anticolors, or one color and one anticolor of the same kind. Anticolor is carried by antiquarks. Hadrons (baryons and mesons) are composed of quarks and gluons. Baryons consist of three valence quarks, which determine their quantum numbers and of which each has a different color. Mesons consist of one valence quark and one valence antiquark carrying one colour and one anticolor of the same kind. However, the valence quarks are only responsible for a small fraction of the hadron's mass. A large part comes from the binding energy, which manifests itself in a cloud of gluons and virtual quark-antiquark pairs, that surrounds the valence quarks, enhances the attractive force at distances of the nucleon size (10^{-15} m) and prevents the constituents from leaving the hadron.

QCD is a non-abelian gauge theory based on the SU(3) symmetry group, as there are three color charges. The degrees of freedom are the spin $\frac{1}{2}$ quarks and antiquarks, that interact by the exchange of vector bosons with spin 1, the gluons. SU(3) is the Special Unitary group of unitary 3×3 matrices, whose determinant is one. SU(3) has eight dimensions, there are eight hermitian, traceless, linearly independent matrices that form the basis and are the generators of the SU(3) group. Accordingly there are eight different gluons, which are the gauge bosons of the strong interaction, they have mass zero and spin one. Non-abelian means that gluons can not only interact with (anti)quarks but also with each other, as they carry color charge themselves. This is one major difference between QCD and QED, where the gauge boson, the photon, does not carry an electric charge.

Another huge difference is that the coupling constant α_s of the strong interaction is in the order of one and not small like in QED, where it is in the order of $\frac{1}{137}$. This makes it very difficult to calculate QCD processes. In fact, the coupling constant is not constant but depends on the momentum transfer Q. For large momentum transfer, which is equivalent to small distances, the coupling constant is small, while for small momentum transfer or large distances the coupling constant becomes large. Equation 1.4 shows that the coupling constant is logarithmically dependent on Q^2 and Λ^2_{QCD} [7]:

$$\alpha_s(Q^2) \propto \frac{1}{\ln(Q^2/\Lambda^2_{\mathrm{QCD}})} \tag{1.4}$$

Λ_{QCD} is a constant in the order of 200 MeV defining the scale. The running of the coupling constant is responsible for a possible separation into two regions. At large momentum transfer, so called hard processes, where α_s is small, is the region of the perturbative QCD. At small momentum transfer, so called soft processes, where α_s is large, is the region of the non-perturbative QCD . In the perturbative region calculations using methods developed for QED can be performed. While in the non-perturbative region only complicated numerical methods using Lattice QCD (LQCD) can be employed and exact calculations are not possible. In LQCD a discrete set of spacetime points (the lattice) is used to reduce the analytically not solvable equations of the QCD Lagrangian to a still very difficult numerical evaluation employing Monte Carlo methods that can be carried out by supercomputers. System parameters are then determined in the continuum extrapolation.

The QCD potential has, in addition to the QED potential, a linearly increasing part depending on the distance [7]:

$$V(r) = -\frac{\alpha_s}{r} + \sigma r \tag{1.5}$$

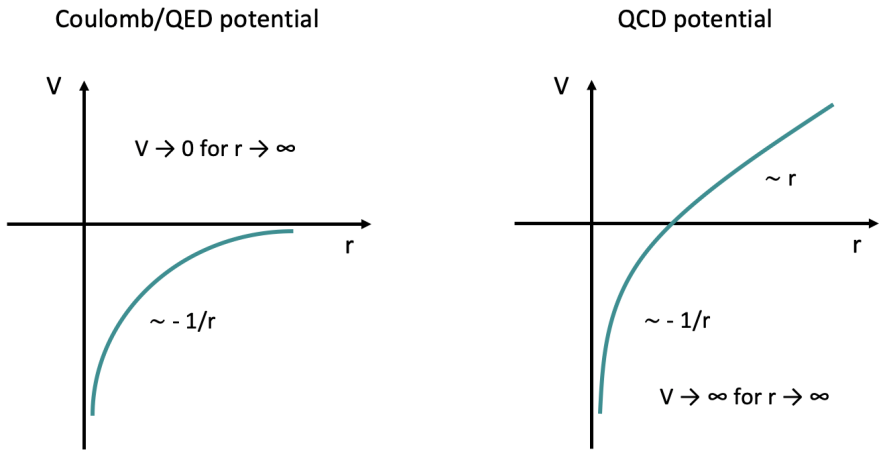

Figure 1.8: Sketch of the coulomb potential (left) and the QCD potential (right).

This can also be seen in figure 1.8. For large distances it is going towards infinity. If one tries to remove one quark from a hadron the attractive force increases. This is called confinement and it means that experimentally no free quarks or color charges can be observed. It is believed that when the energy becomes larger than two quark masses a quark-antiquark pair is produced and a new meson is created.

For small distances though, much smaller than the nucleon size, the coupling constant and the attractive force is very small and quarks and gluons are asymptotically free. This is confirmed by deep inelastic scattering experiments [13]. It leads to the conclusion that in very dense matter quarks and gluons could be free and there would be color deconfinement. A phase transition to a new, plasma-like state of matter, the quark-gluon plasma (QGP), at very high energy densities or/and temperatures was predicted. This phase transition lies in the non-perturbative region of QCD, where momentum transfer is small, so no exact calculations, only numerical simulations are possible [7, 14].

LQCD indeed predicts a phase transition to a QGP. Figure 1.9 shows a LQCD calculation at vanishing baryochemical potential [15]. The normalized pressure, energy density and entropy density are plotted as a function of temperature. The factor T^4 of the normalization is coming from the Stefan-Boltzmann law. The crossover temperature, where the phase transition takes place, is calculated to be $T_c = (154 \pm 9)\,\mathrm{MeV}$ and indicated as yellow vertical band. The solid lines show the predictions of the Hadron Resonance Gas (HRG) model. The HRG is a variant of the thermal model. The thermal model is described in more detail in section 2.1. The limit for a non-interacting ideal gas is indicated as dotted line. The energy density at the crossover region is calculated to be between 0.18 and $0.5\,\mathrm{GeV/fm^3}$, which is 1.2 to 3.1 times the nuclear-matter density.

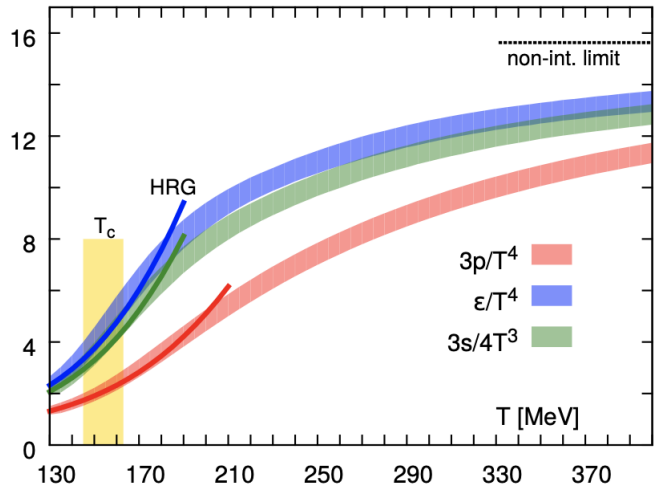

Figure 1.9: LQCD calculation showing normalized pressure, energy density and entropy density as a function of temperature at vanishing baryochemical potential. The yellow vertical band indicates the crossover region, where the phase transition takes place. The solid lines show the predictions of the HRG model. The limit for an ideal gas is indicated as dotted line [15].

In more recent calculations the crossover temperature was determined more precisely and is, for a limited region up to $\mu_B \approx 300\,\text{MeV}$, also calculated as a function of baryochemical potential. At vanishing baryochemical potential μ_B the crossover temperature was calculated to be $T_c = (156.5 \pm 1.5)\,\text{MeV}$ [16] and $T_c = (158.0 \pm 0.6)\,\text{MeV}$ [17] with a slight decrease towards larger μ_B up to about 300 MeV without observing a critical point. The crossover temperatures of all three calculations are in agreement with each other.

2 Production of light (anti)nuclei

In each heavy-ion collision at ultrarelativistic energies thousands of particles are produced. The majority of these particles are pions, few are (anti)protons. But in some collisions also a light (anti)nucleus, like an (anti)deuteron, (anti)triton, (anti)^{3}He or even an (anti)^{4}He is among these particles. Light (anti)nuclei are special objects because their size is comparable to the system created in high-energy pp and p–Pb collisions and to a significant fraction of it in Pb–Pb collisions. At high collision energies the baryochemical potential is zero and therefore particles and antiparticles are produced in equal amounts at midrapidity. The heavier a particle is, the less often it is produced. Because of this light (anti)nuclei are produced very rarely. Therefore a clean particle identification (PID) is needed to separate them from the much more abundantly produced lighter particles. The $^4\overline{\mathrm{He}}$ is the heaviest antiparticle observed so far at a collider. It was first measured by the STAR collaboration at the Relativistic Heavy-Ion Collider (RHIC) in 2011 [18] and later also at the Large Hadron Collider (LHC) [19]. In Pb–Pb collisions at the LHC an exponential decrease of the yields of light (anti)nuclei is observed, if the number of nucleons is increased. This can be seen in figure 2.1 for protons, deuterons, ^{3}He, ^{4}He and the corresponding antinuclei (negative mass number A). With each additional nucleon the yield decreases by about a factor $\frac{1}{330}$. This factor is called penalty factor. In pp collisions the penalty factor is even larger, it is about $\frac{1}{1000}$ [10].

The abundances of the different particle species provide information about the particle-production mechanism at the transition from a QGP to hadrons. Light (anti)nuclei are of special interest, as they are loosely-bound objects with very small binding energies of only 1-10 MeV compared to the system temperature in the order of 100 MeV and it is not understood yet how they can survive the hadronic phase. There are two classes of models to describe nuclei production, the statistical-hadronization model and the coalescence model. They will be described in the following sections [20, 21].

2.1 Statistical-hadronization model

In the statistical-hadronization model (SHM), also called thermal model, light (anti)nuclei are produced at the chemical freeze-out in statistical equilibrium with all other particles.

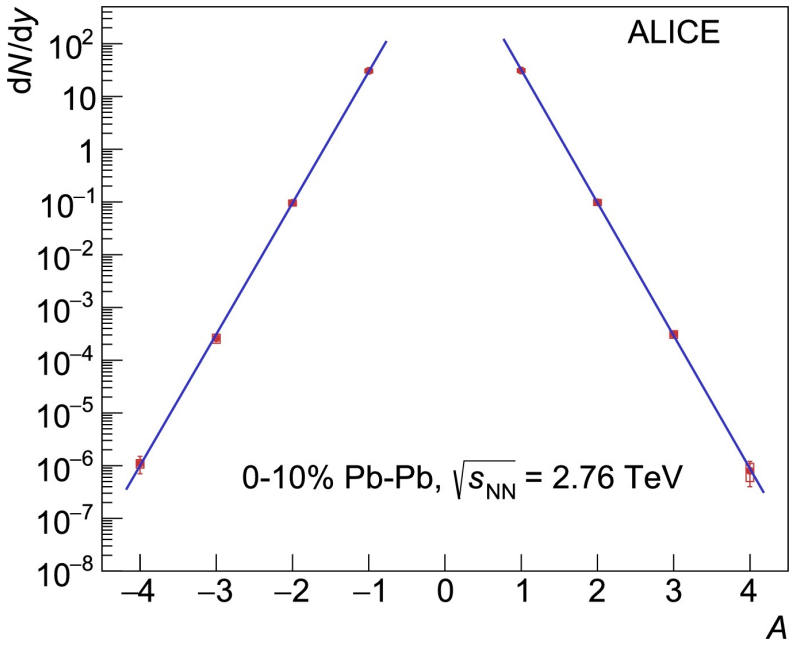

Figure 2.1: Exponential dependence of the yield for (anti)nuclei ((anti)proton, (anti)deuteron, (anti)^{3}He and (anti)^{4}He). The negative values for A represent the antinuclei [19].

The production depends on the particle mass. In heavy-ion collisions, the system can be described by a grand-canonical ensemble, while for small systems like pp or p–Pb a canonical ensemble is employed. Both ensembles assume a heat reservoir of temperature T with which the system can exchange energy. In the canonical approach the quantum numbers are locally conserved and no particles are exchanged, the free parameters are the particle number N, the source volume V and the temperature at chemical freeze-out T_{ch}. In the grand-canonical ensemble, the system exchanges particles. The free parameters are the average particle number $\langle N \rangle$, the source volume V and the temperature at chemical freeze-out T_{ch}. To ensure the average conservation of particle numbers an introduction of the baryochemical potential μ_{B} is necessary. However, at LHC energies the production of particles and antiparticles is equal and so μ_{B} is zero.

The grand canonical partition function Z of QCD thermodynamics can be well approximated for the different hadron species i, as long the temperature stays below the crossover temperature T_{c} [21, 22, 23]:

$$\ln Z_i = \frac{V g_i}{2\pi^2} \int_0^\infty \pm p^2 \, \mathrm{d}p \ln \left[1 \pm \exp(-(E_i - \mu_i)/T)\right] \tag{2.1}$$

Here the + has to be applied for fermions and the - for bosons. $g_i = (2J_i + 1)$ is the spin degeneracy factor, V the volume, T the temperature and E_i the total energy. $\mu_i = \mu_B B_i + \mu_{I_3} I_{3i} + \mu_S S_i + \mu_C C_i$ is the sum of the chemical potentials to conserve on average the baryon, isospin, strangeness and charm quantum numbers. As there is no initial strangeness and charm, the strangeness and charm parts of the chemical potential drop out. Also I_{3i} can be fixed by initial conditions, as the isospin stopping is identical to the baryon stopping. With a fit to measured particle production yields the parameters V, T_{ch} and μ_{B} at chemical freeze-out can be determined. Therefore the complete hadron spectrum must be known.

Figure 2.2 shows p_{T}-integrated hadron yields $\mathrm{d}N/\mathrm{d}y$ measured at midrapidity in central Pb–Pb collisions by the ALICE experiment. Also shown are the fits of the SHM to these data points. The fit is in very good agreement with the hadron yields over nine orders of magnitudes in abundance from pions up to light nuclei. It includes particles and antiparticles, strange and non-strange mesons and baryons, as well as hyper-nuclei. The lower panel shows the ratio between the data and the model. The error bars represent the quadratic sum of statistical and systematic uncertainties of the data.

As one can see the (anti)triton is still missing in this comparison and the (anti)^{4}He has quite large uncertainties.

The best fit to the particle yields is obtained with $T_{\mathrm{ch}} = 156.6 \pm 1.7\,\mathrm{MeV}$, $\mu_{\mathrm{B}} = 0.7 \pm 3.8\,\mathrm{MeV}$ and $V = 4175 \pm 380\,\mathrm{fm}^3$ [22]. μ_{B} is consistent with zero as it should be at LHC energies. The good description of the particle yields, exponentially depending on their mass, shows that they all seem to have a thermal origin. This also includes the light (anti)nuclei, which is especially remarkable as their binding energy is nearly two orders of magnitude smaller than the determined chemical freeze-out temperature. Because of the nuclei's large mass and the exponential dependence of the yield ($\mathrm{d}N/\mathrm{d}y \sim \exp(-m/T_{\mathrm{ch}})$), they are especially sensitive to the freeze-out temperature. Taking only the light (anti)nuclei into account for the fit yields $T_{\mathrm{ch_{nuclei}}} = 159 \pm 5\,\mathrm{MeV}$ [24], which is consistent with T_{ch} determined with all particle yields. The detailed production mechanism of light nuclei and how they can survive at such high temperatures is still not understood. It implies though that the further evolution of the fireball after chemical freeze-out happens without major interactions and should be nearly isentropic.

T_{ch} is also consistent with the crossover temperature T_{c} determined by LQCD calculations, which indicates that the chemical freeze-out might happen only shortly after or at the phase transition.

The SHM can not only be applied at LHC energies but can also describe measured particle yields in nuclear collisions at lower energies where the baryochemical potential

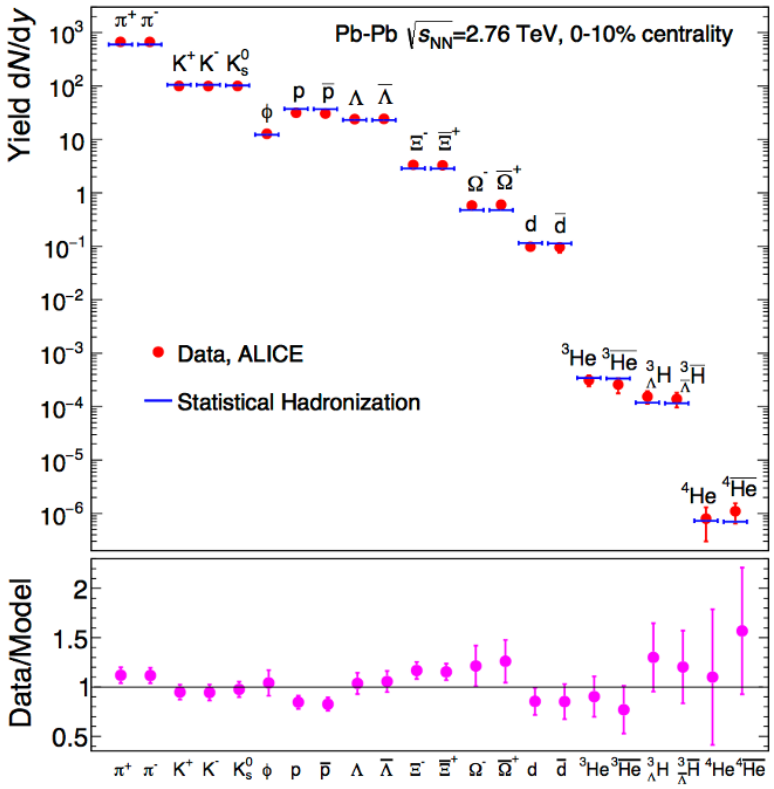

Figure 2.2: p_{T}-integrated hadron yields $\mathrm{d}N/\mathrm{d}y$ measured at midrapidity in central Pb–Pb collisions by the ALICE experiment and fit with the SHM. The lower panel shows the ratio between the data and the model. The error bars represent the quadratic sum of statistical and systematic uncertainties of the data [24].

does not vanish. At very low collision energies the particle yields are much smaller and thus the canonical ensemble has to be applied, as the quantum numbers cannot be conserved only on average but have to be conserved exactly. From each fit to different sets of particle yields at various collision energies a pair of T_{ch} and μ_{B} can be determined. While μ_{B} decreases with collision energy, T_{ch} shows an increase with a saturation at high collision energies larger than $\sqrt{s_{\mathrm{NN}}} = 20\,\mathrm{GeV}$.

In figure 2.3 T_{ch} versus μ_{B} determined in central collisions at different energies is plotted, revealing a phenomenological phase diagram of strongly-interacting matter. The data is compared to predictions for T_{c} from LQCD shown as blue band. The black triangle marks nuclear matter at ground state. The fact that at low energies, i.e. larger baryochemical potentials, the data points seem to converge towards the nuclear matter at ground state shows that T_{ch} is not necessarily connected to a phase transition, as we

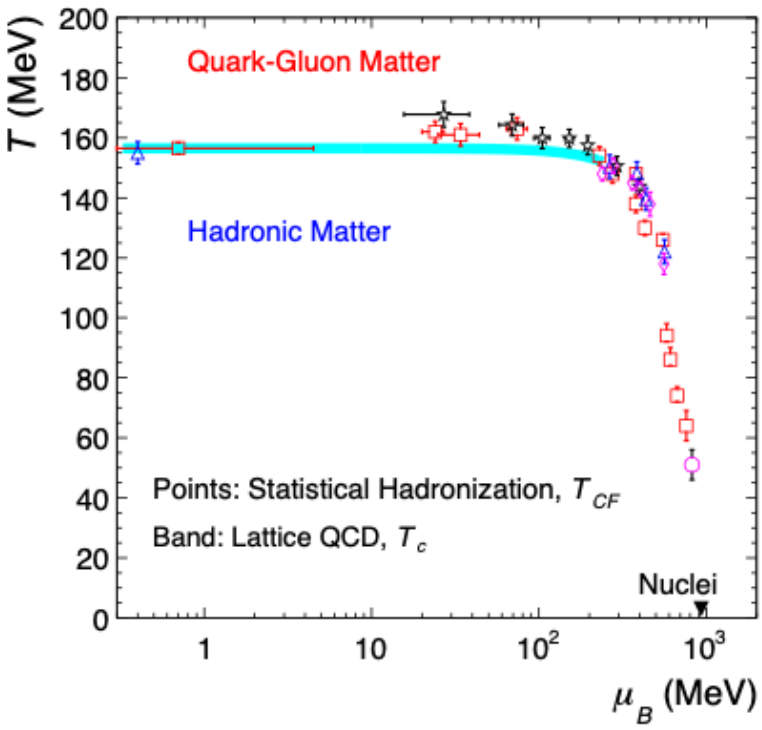

Figure 2.3: Phenomenological phase diagram of strongly-interacting matter. The data points are determined by SHM fits to hadron yields produced in central nuclear collisions at differnt energies and are compared to predictions of T_c from LQCD (blue band). As black triangle nuclear matter at ground state is shown [22].

saw in the schematic picture of the phase diagram (figure 1.1) that the phase transition is expected to be at higher μ_B than nuclear matter. Nevertheless, this could also be due to experimental uncertainties or the gap in the data to low energies. At high energies, i.e. low baryochemical potentials, however, T_{ch} shows a plateau and is well in agreement with T_c expected from LQCD.

2.2 Coalescence model

In the coalescence model nuclei are formed at the kinetic freeze-out by protons and neutrons, which are nearby in space and also have similar velocities. The production rate depends on the wave function of the nucleus and is thus connected to the size of the bound state. The nuclei can also break apart and be recreated by final-state coalescence. The main parameter of the coalescence model is the coalescence parameter B_A, which is

related to the probability to form a nucleus with mass number A via coalescence. B_A is approximated as the ratio of the invariant yield of a given nucleus with mass number A to the nucleon invariant yield to the power of A [10]:

$$B_A = \frac{E_A \frac{\mathrm{d}^3 N_A}{\mathrm{d}^3 p_A}}{\left(E_\mathrm{p} \frac{\mathrm{d}^3 N_\mathrm{p}}{\mathrm{d}^3 p_\mathrm{p}}\right)^A} \tag{2.2}$$

E_A and E_p are the nucleus' and the proton's energy and p_A and p_p their momenta. The proton yield is measured at the corresponding fraction of the nucleus momentum, $p_\mathrm{p} = p_A/A$. It is assumed and expected that the proton and neutron yield and their momentum distribution are the same at midrapidity at the LHC. As neutrons are not charged, they cannot be measured in most heavy-ion experiments. The coalescence probability of creating a nucleus is calculated by the overlap of the wave function with the phase-space distribution of its constituent nucleons [25]. In a simple coalescence approach B_A is independent of momentum and of the size of the emitting volume. This has proven to be incorrect for Pb–Pb collisions where a strong dependence on the collision centrality is observed. B_A is decreasing towards more central collisions, where the source volume is larger. This makes perfectly sense if one considers that the nucleons, even if near in momentum space, can be much further apart in configuration space in a larger source volume. In figure 2.4 a calculation is shown where the source volume is explicitly taken into account [26]. B_A was calculated for $A = 2$, 3 and 4 for different (hyper)nuclei as a function of the source radius R for a given momentum ($p_\mathrm{T}/A = 0.75\,\mathrm{GeV}/c$). The radius r of the nucleus used for the calculation is indicated in the legend. The calculations are also valid for the antimatter counterparts of the mentioned nuclei.

As one would assume, the coalescence probability is smaller for larger A, as the number of constituent nucleons of the nucleus is larger. Furthermore, B_A is decreasing with the source radius R as was already discussed before. However, not only the size of the source, but also the size of the produced nucleus, or more precisely, the ratio of the size of the produced nucleus to the source size is important. The larger the radius of the produced nucleus the smaller B_A. However, while this difference is vanishing at large source sizes, where the difference in the nuclei' radii is much smaller than the source size, it is more distinct for small source sizes like in pp and pA collisions. This can be seen in the case of triton (^{3}H) and ^{3}He (dark blue and light blue lines). As their difference in size is not extremely huge, the difference in B_A arises only at small source radii. For the hypertriton (green dashed line), which has a much larger size, B_A is smaller over the whole range of R, but much more pronounced at small R.

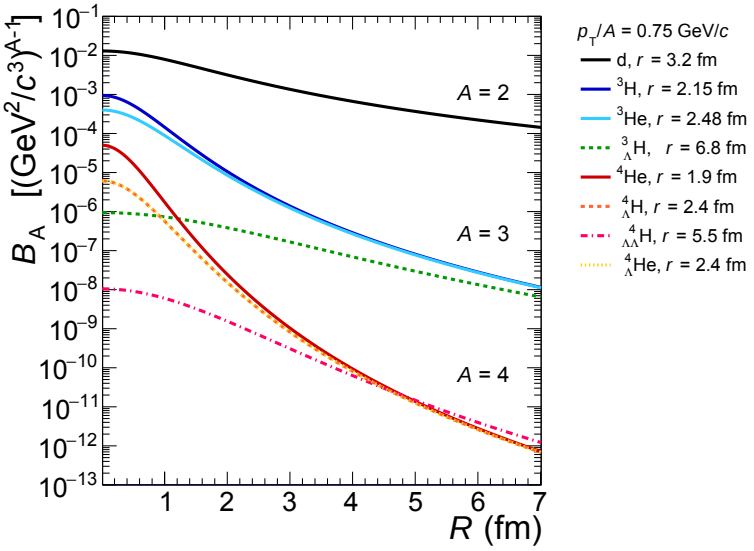

Figure 2.4: B_A calculation for $A = 2$, 3 and 4 for various (hyper)nuclei as a funtion of the source radius for $p_\mathrm{T}/A = 0.75\,\mathrm{GeV}/c$. The radius of the nucleus used for the calculation is indicated in the legend [26].

To compare these coalescence predictions to measured data, it is more practical to calculate B_A versus the mean charged-particle multiplicity $\langle \mathrm{d}N_\mathrm{ch}/\mathrm{d}\eta_\mathrm{lab} \rangle$. This quantity is directly related to the source radius but can be determined in experiments. The mapping of the source radius to the event multiplicity can be done according to the following parametrization [25]:

$$R = a \cdot \langle \mathrm{d}N_\mathrm{ch}/\mathrm{d}\eta_\mathrm{lab} \rangle^{1/3} \tag{2.3}$$

The empirical parameter $a = 0.473\,\mathrm{fm}$ is determined such that the measured (anti)-deuteron B_2 in the most central centrality interval lies on the coalescence prediction.

Figure 2.5 shows coalescence calculations versus $\langle \mathrm{d}N_\mathrm{ch}/\mathrm{d}\eta_\mathrm{lab} \rangle$ exemplarily for triton and ^{4}He [26, 27]. Besides the coalescence predictions of B_3 and B_4 (black solid lines), also the predictions of the statistical-hadronization model (blue dashed lines) that was discussed in the previous section 2.1 is shown. The SHM actually only provides predictions for p_T-integrated yields, as it assumes a static source. To take the p_T dependence of the coalescence parameter into account, it was complemented by a hydrodynamic description of a rapidly expanding source, the Blast-Wave model, which was discussed in subsection 1.2.3. The B_3 predictions of the two models are rather close to each other,

while for B_4 the difference is larger, especially at small multiplicities. It would give great insights to compare the predictions to measured data points as will be done later (see section 5.9).

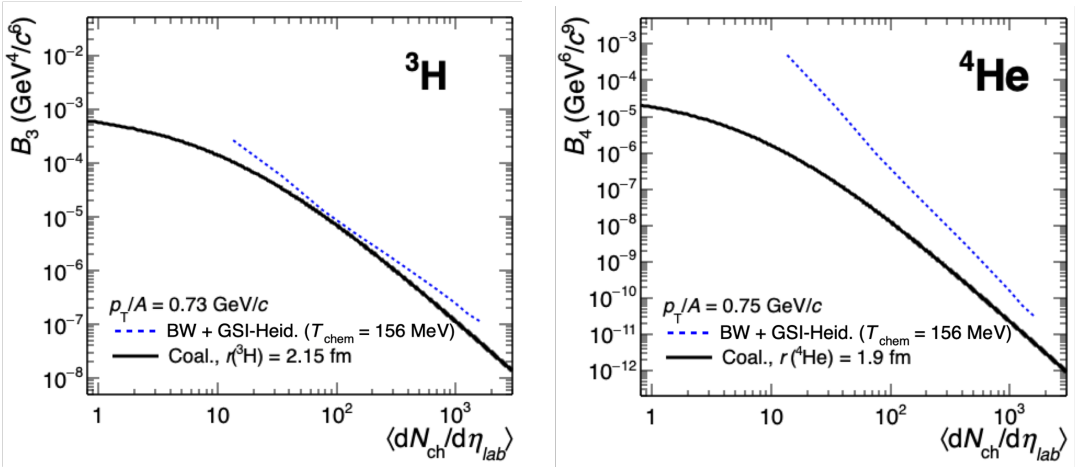

(a) B_3 calculation for (anti)triton.

(b) B_4 calculation for (anti)^{4}He.

Figure 2.5: Coalescence model and SHM+BW predictions for B_3 of triton (left) and B_4 of ^{4}He (right) as a function of mean charged-particle multiplicity [26].

For (hyper)nuclei made out of three baryons it is possible to calculate two-body and three-body coalescence. For ^{3}He for example two-body coalescence is the coalescence between a deuteron and a proton, while three-body coalescence is the coalescence between one neutron and two protons. These calculations usually give slightly different results. Comparisons of these model calculations and data will also be shown later (see section 5.8).

2.3 Objective of this work

From the Run 1 data-taking period (2009-2013) of the LHC there is an inclusive measurement of the (anti)^{4}He yield in Pb–Pb collisions available [19], albeit with large uncertainties, and no measurement of the (anti)triton at all. The much larger data set from the Run 2 data-taking period (2015-2018) where Pb–Pb collisions were recorded in 2015 and, with even more statistics, in 2018 allows for a first differential measurement of the (anti)triton production and of the (anti)^{4}He transverse-momentum distribution. The corresponding analyses are the main focus of this work.

After a description of the experimental site and apparatus in chapter 3, the analyses are described in detail in chapter 4, before the results are presented and discussed in

chapter 5.

The obtained differential production yields of (anti)triton and (anti)^{4}He in Pb–Pb can be included into a combined analysis with other hadron and light nuclei species, testing their compatibility with statistical-hadronization and coalescence approaches for particle production. Aspects of collectivity can be explored in the framework of the Blast-Wave model where the (anti)triton and $^4\overline{\mathrm{He}}$ results are included in the existing data set. For the first time in Pb–Pb collisions, the coalescence parameters B_3 and B_4 for (anti)triton and (anti)^{4}He, respectively, are extracted from the presented data and compared to model predictions.

3 Experimental site and apparatus

The data analyzed within this thesis was collected by the ALICE Collaboration. ALICE (*A Large Ion Collider Experiment*) is an experiment at the LHC that is dedicated to the measurement of particles created in heavy-ion collisions. The LHC is with 26.7 km circumference the world's largest and most powerful particle collider and is located at CERN.

3.1 CERN

CERN is the European Organization for Nuclear Research and is located near Geneva. It was founded in 1954 by twelve European countries with the aim to bring scientific excellence and technological progress and leadership back to Europe after many scientists had left Europe before and during the second world war. In addition, a huge project like this was supposed to strengthen international collaboration. The founding countries were Germany, Switzerland, Belgium, Denmark, France, Greece, United Kingdom, Italy, Yugoslavia (until 1961), Netherlands, Norway and Sweden [28]. More countries followed, today CERN counts 23 member states, with the last member Serbia joining in 2018. However, the collaboration also goes beyond Europe, as there are associated member states, countries with observation status and collaboration agreements with more than 50 countries all over the world. The name CERN is an acronym of the french name of the council that was commissioned with its foundation (*Conseil Européen pour la Recherche Nucléaire*).

Over the years a huge accelerator complex was built at CERN (see figure 3.1). In 1957, the first accelerator, the *Synchro-Cyclotron* (SC), was put into operation. It was able to accelerate protons up to an energy of 600 MeV and was in operation for more than 33 years. In the end of 1959 the *Proton-Synchrotron* (PS) followed. It can accelerate protons to an at that time world's highest energy of 28 GeV. The PS is still running today and is used as a pre-accelerator of the LHC but also to provide dedicated test beams. In 1965, an agreement with France made it possible to extend the accelerators also on French territory. The *Super-Proton-Synchrotron* (SPS) with a circumference of 7 km was put into operation in 1976 and is today also used as a pre-accelerator for the

LHC. It reaches proton energies of up to 450 GeV. Over the years several accelerators were built of whom some are still in operation and some were shut down to make space for more powerful machines.

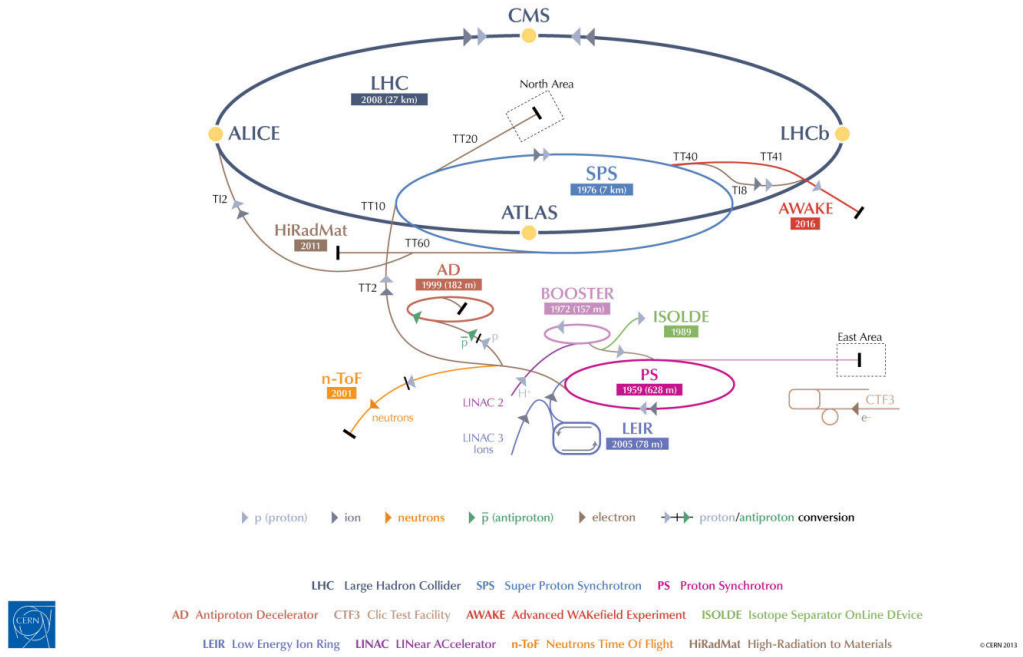

Figure 3.1: CERN's Accelerator Complex [29].

Between 1984 and 1989 a 26.7 km long tunnel was build beneath Switzerland and France, 45 to 170 m below the surface, for the *Large Electron-Positron Collider* (LEP), at that time the world's largest accelerator ever built. The LEP was in operation between 1989 and 2000 and was colliding electrons and positrons with center-of-mass energies up to 209 GeV. In 2000, the LEP was finally shut down and disassembled to make room for the LHC.

Three Nobel Prizes in Physics were achieved at CERN. The first one was awarded in 1984 to Carlo Rubbia and Simon van der Meer for their important role in the discovery of the W- and Z-Boson in 1983 [30]. The second one was awarded to Georges Charpak in 1992 for his invention of the multi-wire proportional chamber in 1968 [31]. The discovery of the Higgs-Boson in 2012 [32, 33] led to the Nobel Prize of 2013 awarded to François Englert and Peter Higgs for their theoretical description of the Higgs mechanism published in 1964 [34].

However, countless not only physical discoveries but also technological developments

and innovations ware achieved in the constant strive to upgrade and improve the accelerators, detectors and data storage and flow, that are now commonly used in industry and everyday life and of which humanity benefits from. The best-known example is the World Wide Web [35].

3.2 LHC

The LHC was designed to accelerate protons to an energy of up to 7 TeV leading to a center-of-mass energy of 14 TeV in pp collisions. For $^{208}Pb^{82+}$ ions this corresponds to a maximal beam energy of 2.76 TeV per nucleon and a center-of-mass energy of 5.52 TeV in Pb–Pb collisions, i.e. smaller by a factor Z/A.

The LHC was built inside the existing 26.7 km long underground tunnel which had been constructed in the 1980s for the former LEP. This was done in order to significantly reduce the costs and was also a crucial factor at the approval of the LHC project in 1994. As the tunnel was originally designed for an electron-positron machine, some compromises and adaptations had to be found for the hadron machine. The tunnel has eight arcs and eight long straight sections (approximately 528 m) in between that were meant to reduce the high synchrotron radiation losses of the electrons and positrons. As hadrons suffer much less from these radiation losses a hadron machine would ideally have shorter straight sections and therefore longer and smoother-bended arcs, as the limiting factor in order to reach the highest possible energies is the magnetic field of the dipole magnets that bend the beam to keep it on its path.

The LHC has four crossing points where the four large Experiments ATLAS, CMS, ALICE and LHCb are located. The underground caverns for ATLAS and CMS were newly built while for ALICE and LHCb caverns from former LEP experiments were reused. Two transfer tunnels of about 2.5 km in length connect the LHC to the CERN Accelerator Complex that is used as injector for the beams. The injection elements for one ring is located in the ALICE cavern, for the other ring in the LHCb cavern.

As the LHC is a particle-particle collider there have to be two separate rings with counter-rotating beams in contrast to particle-antiparticle machines where the beams can share one ring. The internal diameter in the arc sections of the tunnel measures only 3.7 m, which made it basically impossible to fit two completely separate tubes. So, a twin-bore-magnet design was chosen that has the disadvantage that the two rings are magnetically coupled, but was the only solution to fit in the limited space [36].

The peak magnetic dipole field in order to reach a proton energy of 7 TeV is 8.33 T. This is only possible with superconducting electromagnet technology. To keep the beams

on their path 1232 superconducting dipole magnets of 15 m length are used. To maintain the beams focused, in order to reach high collision rates, additional 392 superconducting quadrupole magnets of 5 to 7 m length are installed [37]. In superconducting state electricity can efficiently be conducted through the niobium-titanium (NbTi) coils the magnets are made of without resistance or energy loss. Therefore the magnets have to be cooled down using 120 tones of helium to an operating temperature of 1.9 K, which corresponds to -271.25 °C. The cooling process takes several weeks. It is done in three steps. First the helium is cooled down to 80 K using more than 10,000 tons of liquid Nitrogen, then to 4.5 K using turbines in a second step. Afterwards the helium is injected into the magnets where it is further cooled to the operating temperature of the magnets in the final step using refrigeration units [38].

To accelerate the particles in the beam 16 radiofrequency cavities are used, that also operate in superconducting state. The cavities create an electromagnetic field that oscillates at 400 MHz. Charged particles that are injected into this field receive an electrical impulse that accelerates them. The LHC's radiofrequency cavities accelerate protons from an injection energy of 450 GeV to a (currently) top energy of 6.5 TeV. The oscillation, i.e. the switch of direction of the electromagnetic field leads to the formation of bunches. A proton that has reached the desired energy will not be accelerated further, while a proton that is a bit too slow or too fast will be accelerated or decelerated, respectively. To accelerate the protons from 450 GeV to 6.5 TeV takes about 20 minutes and the bunches pass through the cavities more than 10 million times [39].

Inside the beam pipes an ultra-high vacuum with a residual pressure of only 10^{-14} to 10^{-13} bar exists to prevent the beam from colliding with residual gas atoms. Also the superconducting magnets and the helium distribution lines are surrounded by vacuum. Here it serves the purpose of thermal insulation. These are three separate vacuum systems with a total size of 104 km of pipes under vacuum of which 54 km are the beam pipes and the rest is the insulating vacuum [40].

The total energy of the beams and the electromagnetic energy stored in the magnets exceeds 1 GJ [36]. This energy has to be absorbed safely at the end of each run and in the case of beam instabilities. Therefore a beam-dumping system is installed in the cavern of a former LEP experiment. It consists of several concrete and graphite plates. To absorb the energy in the magnets, resistors can be connected, that turn the energy into heat. In case of problems a safety system can redirect the beam to the beam dump in less than 300 μs [41].

Before being injected in the LHC the proton and heavy-ion beams are preaccelerated by a chain of subsequent machines that accelerate the particles to increasingly higher

energies.

The proton source is a hydrogen gas bottle that injects hydrogen atoms in the source chamber of CERN's linear accelerator LINAC 2. There the electrons are stripped off, so the remaining protons can be accelerated using an electric field in the LINAC to an energy of 50 MeV. Afterwards they enter the *Proton Synchrotron Booster* (PSB or Booster). The Booster is a circular accelerator with a circumference of 157 m. It has four rings on top of each other and the proton packet is divided in four, one for each ring, in order to maximise the beam intensity. The Booster accelerates the protons to 1.4 GeV before the four packages are recombined and injected in the *Proton Synchrotron* (PS). It is 628 m in circumference and pushes the beams to an energy of 25 GeV. At this stage the protons cannot get any faster, as they are already too close to the speed of light and they are getting heavier instead. After the PS the protons enter the *Super Proton Synchrotron* (SPS), which is 7 km in circumference and accelerates the protons to 450 GeV. Afterwards, the protons are finally injected into the two beam pipes of the LHC. The SPS injects protons for about half an hour until 2808 proton bunches are circulating through the LHC [42].

To create a heavy-ion beam ^{208}Pb is heated and the resulting vaporized Pb is ionised in an ion source, which delivers Pb^{27+}. After this the Pb ions are accelerated in CERN's linear accelerator LINAC 3 to 4.2 MeV per nucleon before passing through a stripper foil where some more of their electrons are stripped off, resulting in Pb^{54+}. Afterwards they enter the *Low Energy Ion Ring* (LEIR), a circular accelerator with a circumference of 78.5 m. LEIR transforms the long bunches of Pb ions into short and dense bunches of 2.25×10^8 lead ions via electron cooling and then accelerates them to 72.2 MeV per nucleon. After LEIR the Pb ions are injected in the PS. From then on they pass the same accelerator chain as the proton beams. In the PS they are accelerated to 5.9 GeV per nucleon and then pass through a second stripper foil, a 0.8 mm thick aluminum foil, where they finally lose all remaining electrons becoming Pb^{82+}. These nuclei are then accelerated in the SPS to 177 GeV per nucleon before being injected in the LHC. In the nominal heavy-ion mode 1184 bunches are circulating through the LHC, however this number was even increased in the heavy-ion period of 2018 to 1296 bunches in order to increase the beam luminosity [43, 36, 44, 45].

One of the key indicators for the performance of an accelerator is the luminosity L. It is a measure of how many beam particles can be squeezed through a given space in a given time. The Luminosity is proportional to the collision rate, the number of collisions per second R_{event} [36]:

$$R_{\text{event}} = L \cdot \sigma_{\text{event}} \tag{3.1}$$

σ_{event} is the cross section for a collision, but it can also be the cross section for any (rare) physics process. Then R_{event} is the number of these physics processes per second. The higher the luminosity the more events can be measured and recorded by the experiments in a given time interval. This is especially important if rare processes or particles are examined. The luminosity is machine specific and depends on several beam parameters, like for example the number of particles per bunch, the number of bunches per beam, the revolution frequency and the focusing of the beams. The better focussed the beams are, the higher the probability of an interaction.

While ATLAS and CMS are high-luminosity experiments which aim at a peak luminosity of $L = 10^{34}\,\text{cm}^{-2}\text{s}^{-1}$ for proton beams, LHCb is a low luminosity experiment that aims at a peak luminosity of $L = 10^{32}\,\text{cm}^{-2}\text{s}^{-1}$. ALICE is a dedicated ion-beam experiment which aims at a peak luminosity of $L = 10^{27}\,\text{cm}^{-2}\text{s}^{-1}$ for Pb–Pb ion beams.

Experiments often also state the integrated luminosity. This is a measure on how much data was collected. It is obtained by integrating the luminosity over the time the beam is in operation. Multiplying the integrated luminosity with the cross section of any physics process results in the number of these processes in this data sample:

$$N_{\text{event}} = \sigma_{\text{event}} \cdot \int L dt \tag{3.2}$$

3.3 ALICE detector setup

The ALICE apparatus is a detector setup dedicated to the measurement of particles created in heavy-ion collisions at the LHC. It consists of several detector systems, working together to obtain excellent tracking and particle identification capabilities over a broad range in momentum even at the highest particle multiplicities. The aim is to learn more about QCD and strongly interacting matter at extreme temperatures and energy densities by creating a QGP. As ALICE is the only dedicated heavy-ion experiment at the LHC, it is built as a multi-purpose detector covering most known kinds of particle identification methods like specific energy loss, time-of-flight, transition and Cherenkov radiation, electromagnetic calorimery, topological decay reconstruction and muon filters. ALICE has a total size of $16 \times 16 \times 26\,\text{m}^3$ and a weight of about 10,000 t [46]. It has a cylindrical part, the so-called *central barrel* that consists of several detectors concentrically surrounding the collision point and the beam pipe in layers of increasing radius covering 360° around the beam line and ± 0.9 in pseudorapidity η. The central detectors

are inside a large red solenoid magnet that delivers a maximal magnetic field of 0.5 T. In addition, ALICE has a forward part on one side of the central barrel, the so-called *muon arm*, covering a pseudorapidity region of -4.0 $\leq \eta \leq$ -2.5. It is specialized to measure muons and consists of a dipole magnet, absorbers and tracking chambers.

3.3.1 Coordinate system

In the coordinate system used in ALICE the interaction point is defined as the origin (see figure 3.2). The z axis of the right-handed coordinate system runs with the beam line pointing in the direction opposite to the muon arm, while the x axis points to the LHC center and the y axis points to the Earth's surface. So, the x-y plane is the plane perpendicular to the beam pipe, it is also referred to as *transverse plane*. Also cylindrical coordinates are used. In this case the transverse plane is described with r-ϕ coordinates. r measures the distance from the beam line and ϕ is the azimuthal angle, measured from the x axis clockwise around the beam line, if one is looking in direction of the z axis. The polar angle θ is defined as the angle from the positive z axis and is also often referred to in terms of pseudorapidity η, with $\eta = -\ln(\tan(\frac{\theta}{2}))$. In the transverse plane, i.e. at $\theta = 90°$, the pseudorapidity is zero, this is also called *midrapidity*. In forward direction it is increasing to positive values on the side opposite to the muon arm and to negative values on the side of the muon arm until it becomes $\pm$ infinity in the direction of the positive and negative z axis, respectively. The side opposite to the muon arm is also referred to as A side, while the side where the muon arm is located is called C side.

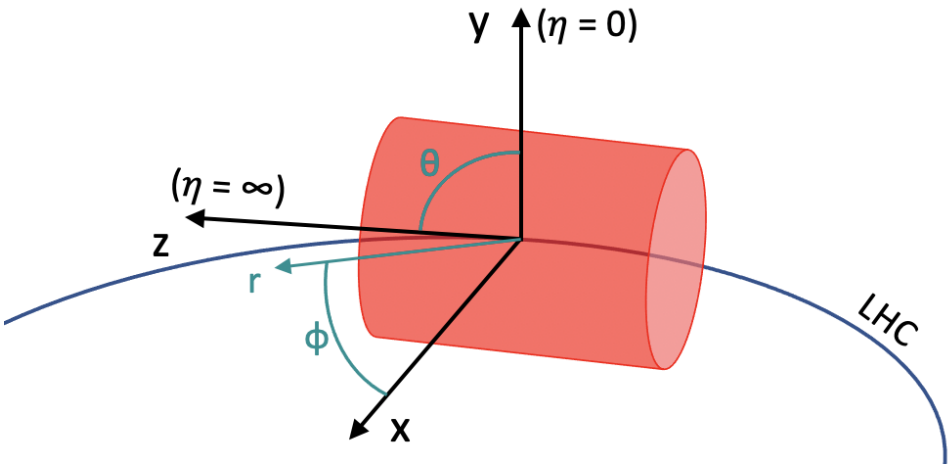

Figure 3.2: Coordinate system of ALICE.

3.3.2 Detector subsystems

In the following the different detector subsystems which are indicated in Figure 3.3 are explained and their functionality and purpose are described. If not indicated differently, the numerical values are taken from [46].

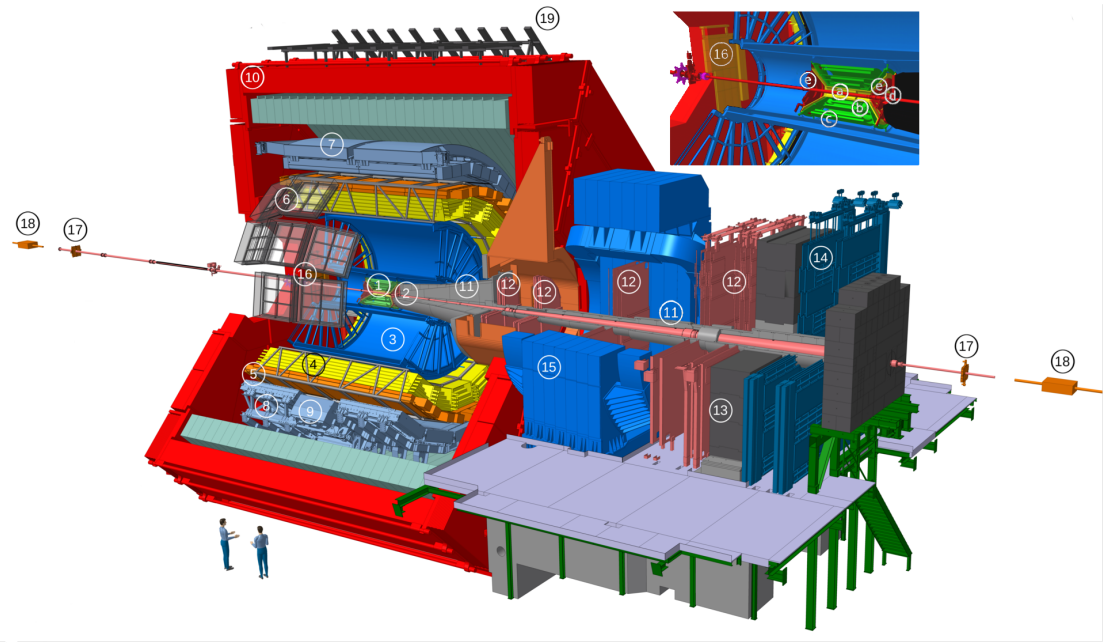

Figure 3.3: ALICE detector setup during the Run 2 period (2015-2018) [47]. The different detector subsystems indicated with the numbers are described in subsection 3.3.2.

(1) Inner Tracking System (ITS)

The ITS is the closest detector to the collision point and so its most important task is to determine the position of the primary vertex with a resolution of about 100 μm and also to find possible secondary vertices. It also helps to identify and track low-momentum particles with momenta below 200 MeV/c and improves the momentum and angle resolution of particles measured in the TPC. The ITS has an azimuthal acceptance of $2\,\pi$ and covers a pseudorapidity range of $|\eta| < 0.9$. It consists of six layers of silicon detectors around the beam pipe using three different technologies. The two innermost layers are made of silicon pixels (SPD), the next two layers are the Silicon Drift Detector (SDD) and the outer two layers of the ITS are using silicon strips (SSD). The average material budget for a particle coming from the primary vertex and perpendicularly traversing the

whole ITS is less than 8 % of radiation length X_0. This is crucial as the momentum resolution of low-p_{T} particles is dominated by multiple scattering in the detector material. Because of its important role the ITS is basically used for nearly all physics analyses.

(a) Silicon Pixel Detector (SPD)
Due to the high particle densities occurring in heavy-ion collisions at the LHC, in the order of 50 particles per cm^2 in the inner ITS layers, a detector with high granularity was necessary and so silicon pixels with binary readout were chosen for the two innermost layers of the ITS. The inner layer of the SPD starts at 3.9 cm away from the beam line and has, with a length of 28.2 cm in z direction, an extended pseudorapidity coverage of $|\eta| < 1.98$ to obtain together with the Forward Multiplicity Detectors (FMD) a continuous coverage for the measurement of the charged-particle multiplicity. The second layer starts at a radius of 7.6 cm also having a length of 28.2 cm in z direction. The first layer contains more than 3.2 million pixels and covers an area of $0.07\,\mathrm{m}^2$ while the second layer contains more than 6.5 million pixels covering an area of $0.14\,\mathrm{m}^2$.

(b) Silicon Drift Detector (SDD)
In the two middle layers of the ITS, where the particle density is still in the order of 10 particles per cm^2, Silicon Drift Detectors have been chosen. The sensitive area of each layer is divided into two drift regions by a central high voltage cathode. The drift velocity lies between 5.6 and 8.1 μm/ns. The third layer starts at a radius of 15.0 cm from the beam line with an extension in z direction of 44.4 cm, covering an area of $0.42\,\mathrm{m}^2$. The fourth layer starts at a radius of 23.9 cm with a length of 59.4 cm in z direction, covering an area of $0.89\,\mathrm{m}^2$. The third layer features 43008 channels and the fourth 90112 channels. The middle two as well as the outer two layers have analog readout and so can be used for particle identification via $\mathrm{d}E/\mathrm{d}x$ measurement for low-momentum, highly-ionizing particles in the non-relativistic region.

(c) Silicon Strip Detector (SSD)
In the two outermost layers the particle density is below one particle per cm^2 and so double-sided silicon micro-strips were used. The outermost layers are important for the matching of the tracks between ITS and TPC and provide a two dimensional measurement of the position of the track. The fifth and sixth layers are located at a radius of 38.0 and 43.0 cm, have lengths of 86.2 and 97.8 cm in z-direction and are covering areas of 2.2 and $2.8\,\mathrm{m}^2$, respectively. The analog readout of the fifth layer has more than 1.1 million channels, while the one of the sixth layer has more than 1.4 million channels.

Due to the analog readout of SDD and SSD the ITS can work as a particle spectrometer for low-p_{T} particles on its own.

(2) V0, T0 and Forward Multiplicity Detector (FMD)

V0, T0 and FMD are all located in forward direction on both sides of the interaction point. They determine event characteristics like multiplicity, centrality and interaction time and provide various triggers.

(d) V0 and T0

The V0 detector constists of two arrays of scintillator counters, one on each side of the interaction point. They are called V0A and V0C. V0A is located on the side opposite to the muon arm 340 cm away from the interaction point and covers a pseudorapidity range of $2.8 \leq \eta \leq 5.1$. V0C is located 90 cm away from the interaction point and is fixed on the front absorber, it covers a pseudorapidity range of $-3.7 \leq \eta \leq -1.7$. They are both segmented in 32 counters that are arranged in four rings. The light is guided via wave-length-shifting fibres to photomultipliers. The V0 provides triggers for the central barrel detectors in pp as well as heavy-ion collisions and also serves as an indicator of the collision centrality via the number of recorded particles per event and its relation to the total multiplicity. The number of fired counters and the total deposited charge can be measured. Four triggers are provided where a signal in both V0 detectors is required: The minimum bias (MB) trigger, the multiplicity trigger (MT), the semi-central trigger (CT1) and the central trigger (CT2). In addition the V0 can help to reject false triggers of the muon spectrometer trigger chambers, if there is no MB trigger in the V0C. It also plays a role in the measurement of the luminosity in pp collisions. The time resolution of the individual counters is better than 1 ns.

The T0 detector consists of two arrays of Cherenkov counters with twelve counters per array. One array is installed on each side of the collision point. T0A is located 375 cm away from the interaction point and covers a pseudorapidity range of $4.61 \leq \eta \leq 4.92$. T0C is installed 72.7 cm away from the interaction point and covers $-3.28 \leq \eta \leq -2.97$. In transverse direction it is installed close to the beam pipe, 6.5 cm away from the beam line. The T0 detector determines the time of the collision with a precision of about 50 ps, this is used as start time for the TOF detector. It also measures the vertex position with a precision of ± 1.5 cm and provides the first trigger, if the vertex position is within a set range, to discriminate from interactions of the beam with residual gas. Even before that trigger, the T0 generates a wake-up signal for the TRD. In addition, the T0 detector can provide minimum bias, central and semi-central triggers, like the V0. The dead time of

the T0 is less than 25 ps.

(e) FMD

The main purpose of the FMD is to determine the event multiplicity in forward direction. It covers a pseudorapidity range of $1.7 \leq \eta \leq 5.0$ on the A side, opposite to the muon arm, and of $-3.4 \leq \eta \leq -1.7$ on the C side. The overlapping coverage with the innermost ITS layer ($|\eta| < 1.98$), ensures a continuous measurement of the charged-particle multiplicity in the mid- and forward-rapidity region. The azimuthal coverage of the FMD is 360°. Due to the FMD's radial and azimuthal segmentation also multiplicity fluctuations and the orientation of the reaction plane can be estimated, respectively. The FMD consists of three ring systems. FMD2 and FMD3 are placed on each side of the ITS, on A and C side, respectively. They each have an inner and an outer ring. The z positions of the outer rings are both 75.2 cm away from the interaction point on both sides of it. The inner rings do not have the same distance from the interaction point due to the position of the T0 detector. On the A side the inner ring is placed 83.4 cm away from the interaction point, on the C side 62.8 cm away. FMD1 only consists of an inner ring and is located further away from the interaction point (320 cm) on the A side to extend the pseudorapidity coverage up to 5.0. This upper limit is given by the increasing number of secondary particles in the forward pseudorapidity region. The radius of the inner rings of the FMD is constrained by the beam pipe (3.9 cm), the outer radius of the outer rings is constrained by the inner radius of the TPC (84.8 cm). The inner rings are divided in 20 azimuthal sectors consisting of 512 silicon strips each with an inner radius of 4.2 cm and an outer radius of 17.2 cm. The outer rings are divided in 40 azimuthal sectors with 256 silicon strips each. The silicon strips of the outer rings have an inner radius of 15.4 cm and an outer radius of 28.4 cm. This results in a total number of 51,200 silicon strips to be read out. The readout time is with $>1.2\,\mu$s quite long and so the FMD cannot be used as a multiplicity trigger and only provides offline information.

(3) Time Projection Chamber (TPC)

The TPC is the main tracking detector of ALICE and the most important detector in the analyses presented in this work. A schematic view of the TPC is shown in figure 3.4. The TPC is located in the central barrel surrounding the ITS, also having an azimuthal acceptance of $2\,\pi$ and a pseudorapidity coverage of $|\eta| < 0.9$. It is designed to provide the best possible two-track separation, particle identification and vertexing with a good momentum resolution from low p_{T} of 0.1 GeV/c up to 100 GeV/c at extreme charged-particle multiplicities. With an inner radius of 84.8 cm, an outer radius of 246.6 cm and a

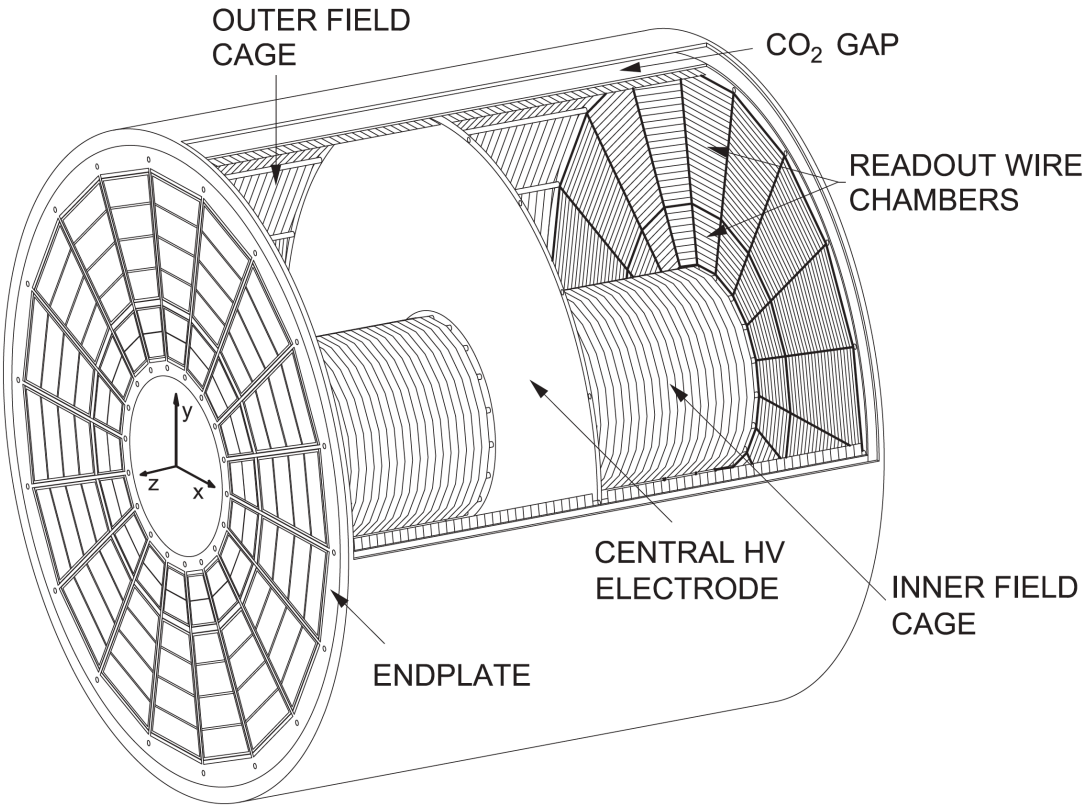

Figure 3.4: Schematic view of the ALICE TPC [48].

length of 5 m along the z axis, the TPC has an active gas volume of about 90 m^3. During Run 2 it was filled with two different gas mixtures, Ar-CO_2 (88-12) in the years 2015, 2016 and 2018 and Ne-CO_2-N_2 (90-10-5) in the year 2017. The drift volume of the TPC is divided into two parts of 2.5 m length by a central high-voltage electrode, together with the cylindrical field cage it provides a highly uniform electric field of 400 V/cm along the z axis parallel to the magnetic field in the central barrel. The drift velocity of the electrons is about 2.7 cm/μs, which leads to a maximal drift time to the readout of 92 μs. To keep the variation of the temperature inside the drift volume below 0.1 K the TPC is equipped with several heat screens and cooling circuits. The readout chambers are located at the end caps of the cylinder. The readout is divided into 18 trapezoidal sectors on each side of the TPC. Each sector is divided in an inner and an outer readout chamber (IROC and OROC). During Run 1 and Run 2 the TPC was equipped with multi-wire proportional chambers (MWPC) with cathode pad readout. To keep the occupancy small and to obtain the necessary resolution the pad planes consist in total

of about 560,000 pads of three different sizes, smaller ones in the IROCs and larger ones in the OROCs. Above the pad plane an anode wire plane, then a cathode wire plane and above this a gating grid is installed. The distance between anode and cathode wire planes is only 2 mm and 3 mm in IROCs and OROCs, respectively, what leads to an operating gain of up to 20,000. The gating grid prevents ions that are created in the amplification process from drifting back into the drift volume, where they would lead to space charges and so distortions of the electric field. This gating grid is usually closed so that neither electrons from the drift volume, nor ions from the amplification region can pass it. Only 6.5 μs after a collision the gating grid is opened and stays open for the duration of about 90 μs, one electron drift-time period, and is closed again before the much slower ions can enter the drift volume. The disadvantage of the gating grid is that it makes the TPC quite slow and limits the interaction rate to about 3 kHz.

(4) Transition Radiation Detector (TRD)

The TRD surrounds the TPC in the central barrel with a radial extension of 2.9 m $< r <$ 3.68 m. It has an azimuthal acceptance of 360° and covers a pseudorapidity range of $|\eta| < 0.84$. The main purpose of the TRD is to provide electron and pion separation for momenta above 1 GeV/c by exploiting specific energy loss in a gas and the fact that high-momentum electrons emit transition radiation when passing a radiator. In addition the TRD is used for tracking and triggering of high-p_{T} charged particles. The material budget has to be small to reduce Bremsstrahlung, it is 23.4 % of a radiation length X_0 in radial direction. The TRD is divided in 18 super modules. Each super module has a weight of 1650 kg and contains 30 readout chambers which are arranged in stacks of six chambers on top of each other and five of these stacks in a row in z direction. In total the TRD consists of 540 individual readout chamber modules. Each chamber consists of a 48 mm thick radiator made of two layers of Rohacell foam and irregular polypropylene fibre mats in between, then a 30 mm thick drift region containing Xe-CO_2 (85-15) and a 7 mm thick multi-wire proportional chamber with pad readout. In azimuthal direction one pad row consists of 144 pads. The chambers of the central stacks in z direction have twelve pad rows while all other chambers have 16 pad rows. Ionizing particles that pass the gas volume create electrons, while fast enough particles that exceed the threshold for transition radiation also create about one or two X-ray photons that are then with high probability converted to electrons in the xenon gas mixture, due to its high charge number. The produced electrons then drift with a velocity of 1.5 cm/μs to the anode wire plane of the Multi-Wire Proportional Chambers (MWPC). Due to their good position and angular resolution the six layers of the TRD can also contribute to the tracking

of high-p_{T} particles and can improve the overall momentum resolution in the central barrel. Three central readout-chamber stacks in front of the PHOS detector have not been installed in order to reduce the amount of material in front of the electromagnetic calorimeter.

(5) Time-Of-Flight detector (TOF)

The TOF detector surrounds the TRD in the central barrel with a radial extension of $3.7\,\mathrm{m} < r < 3.99\,\mathrm{m}$. It has an azimuthal acceptance of 360° and covers a pseudorapidity range of $|\eta| < 0.9$. Together with the momentum and track length information of TPC and ITS the TOF detector provides particle identification in the intermediate momentum range. The detector is made of Multi-gap Resistive-Plate Chambers (MRPC) as they have an intrinsic time resolution better than 40 ps and an efficiency close to 100 %. In the high electric field a traversing charged particle immediately starts a gas avalanche that can be measured on the pick-up electrodes without any delay created by drifting electrons. The TOF detector is segmented in 18 super modules in ϕ direction, each weighing about 1.4 t. Each super module consists of five individual modules arranged in z direction. The individual modules are made of several 122 cm long and 13 cm wide 10-gap double-stack MRPC strips. Each strip is divided into two rows of 48 pads with a size of $3.5\,\mathrm{x}\,2.5\,\mathrm{cm}^2$. The strips are arranged transversely to the beam axis and are placed inside the gas-tight modules. The central module of each super module contains 15 MRPC strips and has a length of 117 cm, while the two intermediate and the two external modules all contain 19 MRPC strips but differ in length with 137 and 177 cm, respectively. The strips are tilted with increasing angle starting with 0° in the middle of the central module and going to 45° at the outer ends of the external modules in order to minimize the path length of the passing particles through the strips and so reduce shared signals of adjacent pads that would increase fluctuations in the time signal. In addition the strips overlap a bit that the edges of the pads are aligned to avoid dead areas in z direction. The modules are filled with $C_2H_2F_4$-C_4H_{10}-SF_6 (90-5-5). The material budget in radial direction is 29.5 % of X_0. Three central modules in front of the PHOS detector have not been installed in order to reduce the amount of material in front of the electromagnetic calorimeter.

(6) High-Momentum Particle Identification Detector (HMPID)

The HMPID is built out of seven modules of Ring Imaging Cherenkov (RICH) counters. Each module has a size of about $1.5\,\mathrm{x}\,1.5\,\mathrm{m}^2$. The HMPID is located in the central barrel, after the TOF detector, 5 m away from the beam line in radial direction. It does

not cover the full azimuth and is installed at a two o'clock position, if one is looking in direction of the negative z axis. The coverage is 5 % of the central barrel acceptance, namely $|\eta| < 0.6$ in pseudorapidity and $1.2° < \phi < 58.8°$ in azimuthal direction. The HMPID was optimized to separate pions from kaons and kaons from protons in the high-momentum region above 1 GeV, where the identification cannot be done by ITS, TPC and TOF alone anymore. The momentum range that is covered by the HMPID is determined by the radiator which is a 15 mm thick layer of liquid C_6F_{14}, resulting in $\beta_{\text{min}} = 0.77$. The Cherenkov photons emitted by fast charged particles passing the radiator are detected by a photon counter. The photon counter consists of a MWPC, the pad cathode of which is covered with a 300 nm thin layer of CsI. After the radiator the Cherenkov light cone passes a quartz window and then enters an about 8 cm long, CH_4 filled gas volume where it expands before reaching the photon detector. A positive collection electrode close to the quartz window prevents electrons, produced by charged particles passing the gas volume, to enter the photon detector. The CsI photocathode of the MWPC is segmented in pads of $8 \text{ x } 8.4\,\text{mm}^2$. The electrons are collected by the anode wire plane that is made of 20 μm thick gold-plated tungsten-rhenium wires, spaced by 4.2 mm. The cathode wire plane of the MWPC as well as the collection electrode on the other side of the gas volume is made of 100 μm thick gold-plated copper-beryllium wires.

(7) ElectroMagnetic CALorimeter (EMCal)

The EMCal is a lead-scintillator sampling calorimeter, located directly beneath the magnetic coil of the L3 magnet and next to the HMPID, about 4.5 m away from the beam line, covering a range of $|\eta| < 0.7$ in pseudorapidity and $80° < \phi < 187°$ in azimuthal angle. The EMCal has a moderate resolution but with its large acceptance it increases the coverage of electromagnetic calorimeters of ALICE significantly. It enables a measurement of charged as well as neutral energy components of jets and also provides fast triggers for hard jets, photons and electrons. The EMCal is segmented in twelve super modules, of which two are smaller and have one third of the size of the full-size ones. The super modules can be slid into a dedicated support structure, that is attached to the L3 magnet yoke, and holds the full 100 t weight of the detector. Each full-size super module consists of 288 single modules. Always twelve single modules are combined in a strip module and 24 of these are installed in one super module. Each single module has a cross section of $12 \text{ x } 12\,\text{cm}^2$ and a height of 24.6 cm. It contains four stacks of 76 alternating layers of 1.44 mm lead 77 layers of 1.76 mm polystyrene base scintillator with an array of 36 longitudinal wavelength-shifting fibres in between. At the front face of the module each fibre ends in an aluminized mirror, at the back of the module the fibres

lead to an avalanche photodiode (APD) photo sensor. One stack that leads to one APD is referred to as tower and has an active volume of $6 \times 6 \times 24.6\,\mathrm{cm}^3$. In total the EMCal has 3,168 modules and 12,672 towers. The material budget is 20.1 radiation lengths X_0 and the Molière radius is 3.2 cm.

(8) Di-Jet CALorimeter (DCal)

The DCal is an extension of the EMCal on the opposite side in ϕ of the central barrel that was installed in the first long shutdown of the LHC before the RUN 2 data-taking period. It enables the measurement of back-to-back correlations of jets. The DCal has an azimuthal acceptance of $\Delta\phi = 60°$ and covers a pseudorapidity range of $|\eta| < 0.7$. The DCal consists of six super modules that are basically identical to the EMCal ones but with only two thirds of the length in η, so containing only 16 instead of 24 strip modules. The reason for that is the presence of the PHOS detector modules at midrapidity, three PHOS modules are on both sides adjoined by the DCal super modules [49].

(9) PHOton Spectromenter (PHOS) and Charged-Particle Veto detector (CPV)

PHOS is a high-granularity electromagnetic spectrometer. It has a limited acceptance and is installed at midrapidity with a radial distance from the beam line of 460 cm. It covers a pseudorapidity range of $|\eta| < 0.125$ and an azimuthal angle of $250° < \phi < 320°$. PHOS is designed to measure spectra, collective flow and correlations of thermal and prompt direct photons coming from the initial phase of the collision as well as neutral mesons via their decay into photon pairs. The detector consists of an electromagnetic calorimeter made of $PbWO_4$ crystals (PHOS) and a MWPC as charged-particle veto (CPV) in front of it. Because of the high particle multiplicities, the calorimeter must be far away from the collision point, very dense with a small Molière radius, and highly segmented. There are three full size and one half size PHOS+CPV modules [50], each full module covers 20° in azimuthal angle. The full modules consist of 3,584 lead-tungstate crystal, $22 \times 22 \times 180\,\mathrm{mm}^3$ in size, glued to an avalanche photo-diode with low-noise preamplifier. The length of the crystals corresponds to 20 radiation lengths X_0. The PHOS modules are operated at a temperature of -25 °C to increase the light yield of the crystals. The CPV is mounted with 5 mm distance in front of the electromagnetic calorimeter and has a charged-particle detection efficiency better than 99 %. It has a spatial resolution of about 1.54 mm in beam direction and 1.38 mm transverse to the beam. The MWPC has a cathode-pad readout, divided in 7,168 $22 \times 10.5\,\mathrm{mm}^2$ large pads per module. The active volume is 14 mm thick, covers an area of about $1.8\,\mathrm{m}^2$ per module and is filled with Ar-CO_2 (80-20). The material budget of the CPV detector is

less than 5 % of X_0.

(10) Solenoid magnet

The solenoid magnet was originally build for the L3 experiment at LEP and was reused for ALICE in order to save costs. It houses all central barrel detectors, has a diameter of 15.8 m and a length of 14.1 m. The total weight is 7800 tons. The magnet is operated at room temperature and delivers a maximal magnetic field of 0.5 T along the z axis created by an octagonal aluminium coil with 168 turns. The octagonal steel yoke, that surrounds the coil, is closed at the pole caps by 'doors' that can be opened if the detectors have to be accessed. The magnet is cooled by demineralized water flowing through an external circuit. The field variations in the active volume of the detectors is less than 2 %.

(11) Absorbers

The front absorber is part of the muon spectrometer, but it is located inside the solenoid magnet in the central barrel, pointing towards the muon arm. It starts 90 cm away from the interaction point and has a length of 4.13 m which corresponds to about 60 times the radiation length X_0 and its purpose is to absorb hadrons and photons coming from the interaction vertex. It is mostly made out of carbon and concrete to minimize small-angle scattering and energy loss of the crossing muons and is also designed for shielding the central barrel detectors from secondary particles created in the absorber material itself by traversing hadrons.

Another absorber, the beam shield, surrounds the beam pipe throughout the length of the muon spectrometer arm. It protects the muon spectrometer from background-particle interactions and is made out of tungsten, lead and stainless steel.

(12) Muon tracker

The muons are detected in forward direction in a pseudorapidity range of -4.0 $\leq \eta \leq$ -2.5. For the measurement of heavy-quark resonances in the $\mu^+\mu^-$ decay channel a good invariant-mass resolution is necessary. To resolve for example the Υ, Υ' and Υ'' resonances the invariant-mass resolution has to be at least 100 MeV/c^2 in the 10 GeV/c^2 dimuon invariant-mass region. This is achieved with a bending strength of the spectrometer magnet that is large enough and a good spatial resolution of the muon tracking system of about 100 μm.

The muon tracking system consists of 5 tracking stations with 2 chamber planes each. Two stations are placed after the front absorber before the dipole magnet, the first cham-

ber directly after the absorber to determine the exit points of the muons as accurately as possible. One station is located inside the dipole magnet and two stations are placed after the dipole magnet. All tracking chambers together cover an area of about $100\,\mathrm{m}^2$, where the chambers further away from the collision point are larger (up to more than $30\,\mathrm{m}^2$) than the chambers closer to the collision point (few m^2). The chambers are filled with an Ar-CO_2 (80-20) gas mixture. For reasons of multiplicity and therefore detector occupancy a fine-granularity segmentation of the readout pads was chosen. The pad size is smallest ($4.2 \times 6.3\,\mathrm{mm}^2$) at the first tracking station closest to the beam pipe and becomes larger going to larger radii as well as further away from the interaction point in z direction. The last three tracking stations have pad sizes of up to $5 \times 100\,\mathrm{mm}^2$ at the largest radii, where the hit density is smallest, to keep the total number of readout channels limited to about one million. To keep multiple scattering of the muons at a minimum composite materials like carbon fibre are used for the chambers that results in $0.03\,X_0$ per chamber. With this chamber design a spatial resolution of about $70\,\mu$m is reached.

In order to obtain a good invariant mass resolution it is important that the ten tracking chambers are properly aligned. Therefore there are dedicated runs without magnetic field at the beginning of each data-taking period to determine the position of the chambers with straight muon tracks. In addition an optical Geometry Monitoring System (GMS) checks whether there are any displacements or deformations during the data taking, coming for example from switching on the magnetic field. The position resolution of the GMS is better than $40\,\mu$m.

(13) Muon filter

The muon filter is a 1.2 m thick iron wall that is placed after the last tracking chamber to protect the trigger chambers, as for these the front absorber and the beam shield are not sufficient. The muon filter stops together with the front absorber muons with energies below $4\,\mathrm{GeV}/c$.

(14) Muon trigger

The aim of the muon trigger is to select events with high-p_T muons coming from the decay of heavy quarkonia or the semi-leptonic decays of open charm and beauty and to exclude events with only low-p_T muons coming from π and K decays. Therefor a p_T cut has to be applied on each individual muon created in one event. There are two p_T thresholds that can be set independently between about 0.5 and $2\,\mathrm{GeV}/c$ and that are applied in parallel for each muon. The trigger system can decide whether there is a single

muon above the thresholds, two like-sign muons or two unlike-sign muons. For two p_{T} thresholds that results in six trigger signals per event.

The muon trigger system has to be fast and provide a spatial resolution better than 1 cm, therefore resistive plate chambers (RPCs) operated in streamer mode were chosen. The trigger signal is delivered less than 800 ns after an interaction. The muon trigger system consists of four RPC planes that are arranged in two stations. The stations are one meter apart from each other and placed after the muon filter. Each plane consists of 18 RPC modules with a size of about $70\,\mathrm{x}\,300\,\mathrm{m}^2$, adding up to a total active area of about $140\,\mathrm{m}^2$. For the location in x, y direction the readout is segmented into strips, where anode and cathode strips are turned by 90° against each other. The length and pitch of the strips is increasing with increasing distance from the beam axis.

(15) Dipole magnet

The dipole magnet is part of the muon spectrometer arm and is located next to the solenoid magnet, 7 m away from the interaction point. It provides a horizontal magnetic field of 0.67 T which is perpendicular to the beam line. The free gap between the poles lies between 2.97 and 3.96 m, the steel yoke has a height of 9 m and a length of 5 m, leading to a total weight of the magnet of 900 tons. The magnet is made of two saddle type coils that are each assembled from three sub-coils with 56 turns per sub-coil. The size and the magnetic field of the dipole magnet was determined by the angular acceptance and mass resolution of the muon spectrometer arm as the tracking chambers are up to 14 m away from the interaction point. The magnet is operated at room temperature and cooled by demineralized water flowing trough an internal hole in the two saddle type coils.

(16) Photon Multiplicity Detector (PMD)

The PMD is located inside the solenoid magnet in forward direction at the side opposite of the muon arm, 364 cm away from the interaction point and covers a pseudorapidity range of $2.3 \leq \eta \leq 3.7$ and 360° in ϕ direction. It measures the multiplicity and spatial distribution of photons. Due to the large particle density in forward direction, building an electromagnetic calorimeter at that position is not possible and a preshower method is applied. The PMD consists of two planes of highly granular gas proportional counters with a 2 cm thick converter, made of lead and stainless steel in between, that creates the preshower. The first detector plane in front of the converter only measures charged-particles and is thus used as a charged-particle veto. The second detector plane after the converter measures the position and amount of photons in each event. Each plane of the PMD is made of 24 modules that each consist of 4608 honeycomb shaped cells of gas

proportional counters with a cross section of 0.22 cm^2 and a length of 0.5 cm. The cells are filled with Ar-CO_2 (70-30). The honeycomb shaped cathode is set to an operating voltage of -1400 V while a 20 μm thick gold plated tungsten wire at ground potential in the middle of each cell serves as anode. Each module is a high voltage isolated and gas tight enclosure. The PMD is constructed in two equal halfs that are installed and can be moved on a stainless steel girder. Each half is independently equipped with cooling, gas supply and electronics.

(17) ALICE Diffractive (AD) detector

The AD detector is located in forward direction outside of the solenoid magnet and consists of two stations (ADA and ADC), one on each side of the collision point, 16.95 m and 19.57 m away from it, respectively. It covers a pseudorapidity range of $4.7 \leq \eta \leq 6.3$ on the A side and $-6.9 \leq \eta \leq -4.9$ on the C side. The AD detector was installed during the first long shutdown of the LHC before the RUN 2 data-taking period in order to improve the trigger efficiency to select diffractive events in proton-proton collisions. Each station is made of two layers of four 18×21 cm^2 large plastic scintillator pads arranged around the beam pipe. Each scintillator pad is coupled to a photomultiplier via a wavelength shifting bar and an array of about 200 clear optic fibres. Charge and time of the signals are measured by the AD front-end electronics. The time resolution of ADA and ADC is about 440 ps and 300 ps, respectively. The AD detector significantly increases the coverage for forward physics to about twelve units in pseudorapidity. Because of its good time resolution the AD detector can also be used for technical tasks like beam-gas background rejection. In Pb–Pb and p–Pb collisions the AD detector provides an extended centrality trigger [51, 52].

(18) Zero Degree Calorimeter (ZDC)

The ZDC is located at 0° relative to the beam direction and its purpose is to determine the collision centrality in heavy-ion collisions. It consists of two sets of hadronic calorimeters, that are located 116 m away from the interaction point to both sides of it, and of one set of electromagnetic calorimeters, placed 7 m away from the interaction point on the side opposite to the muon arm. By measuring the energy of the spectator nucleons that is carried in forward direction in the hadronic calorimeters, the number of participant nucleons and with this the collision centrality can be estimated. If all spectator nucleons $N_{\text{spectators}}$ were detected, the number of participant nucleons $N_{\text{participants}}$ could be calculated by the following equations:

$$
\begin{aligned}
E_{ZDC} &= \sqrt{s_{\mathrm{NN}}} \cdot N_{\mathrm{spectators}} \\
N_{\mathrm{participants}} &= A - N_{\mathrm{spectators}}
\end{aligned}
$$

$\sqrt{s_{\mathrm{NN}}}$ is the center-of-mass energy per nucleon pair and A is the number of nucleons of the colliding nuclei, in case of Pb it is 208.

The two sets of hadronic calorimeters consist each of one neutron calorimeter (ZN), located between the beam pipes, and one proton calorimeter (ZP), located next to the outgoing beam pipe in the horizontal plane of the LHC on that side where the positive particles are deflected by the magnetic elements of the beam line. The hadronic calorimeters are made of quartz fibres as active material, where Cherenkov radiation is produced and a passive, dense absorber material where the shower is generated.

As between the beam pipes the space is very limited the ZN has to be very compact ($7.04 \times 7.04 \times 100\,\mathrm{cm}^3$). So a very dense passive material (tungsten alloy) is used for the ZN to contain the whole shower energy. For the ZP the space limitations are more relaxed ($12 \times 22.4 \times 150\,\mathrm{cm}^3$) and the absorber material is made of brass. The quartz fibres that are placed between the absorber material with a spacing smaller than one radiation length are read out by photomultiplier tubes.

As the radiation environment where the ZDC is located is very harsh the hadronic calorimeters are installed on lifting platforms such that they can be moved out of the horizontal LHC plane when they are not used. In very central Pb-Pb collisions a small energy deposition in the hadronic calorimeters is expected. However, in very peripheral collisions the nucleons of the Pb nuclei stay bound or the Pb nuclei break into fragments with similar charge-to-mass ratio like the original nucleus and thus do not leave the beam pipe, meaning they cannot be measured in the hadronic calorimeters. So, a small energy deposition can mean a very central or a very peripheral Pb-Pb collision. To solve this situation the electromagnetic calorimeters (ZEM) are used. They measure the energy deposited by particles emitted in forward direction, mostly photons, that increases the more central the collision was. The ZEM's dimension is $7 \times 7 \times 20.4\,\mathrm{cm}^3$ and the absorber is made of lead plates with quartz fibres as active material in between to detect the Cherenkov light. The light is transferred via a light guide to a photomultiplier tube. Central Pb-Pb collisions are hence characterized by a small energy deposition in ZNs and ZPs and a large energy deposition in the ZEMs.

(19) ALICE COsmic Ray DEtector (ACORDE)

ACORDE is located on top of the L3 magnet and its purpose is to detect cosmic rays. It consists of 60 modules of plastic scintillator counters. Each module is made of 2 plastic scintillators with $190 \times 20\,\mathrm{cm}^2$ active area on top of each other which are read out in coincidence. At the end of each scintillator two photomultipliers are mounted. The coverage of ACORDE is $|\eta| < 1.3$ in pseudorapidity and $|\phi| < 60^\circ$ in azimuthal angle. ACORDE provides a very fast trigger when it is hit by a cosmic muon for calibration and commissioning of several ALICE tracking detectors (TPC, TRD, TOF, HMPID, ITS). In addition ACORDE can study together with the TPC, TRD and TOF the atmospheric muon momentum spectrum in a wide range from about 0.1 to $2\,\mathrm{TeV}/c$.

3.3.3 Trigger system and data acquisition

To reduce the stored amount of data and to make sure the most interesting and as many as possible events are chosen a trigger system is mandatory. The Central Trigger Processor (CTP) of ALICE performs trigger selections that are optimized for various different running modes, i.e. collision systems that vary in collision rate by almost two orders of magnitude. It also has to take into account that the time period the various sub-detectors are busy after receiving a trigger signal differs by up to nearly a factor 100.

The fast detectors that contribute to the trigger system on the hardware side are T0, V0, ZDC, SPD, TOF, TRD, PHOS, EMCal, Muon, AD and ACORDE. The trigger system operates in several levels. The fastest trigger is a pre-trigger to activate the TRD electronics, it is generated by the T0 detector less than 900 ns after a collision. There are three more trigger levels L0 at $1.2\,\mu$s, L1 at $6.5\,\mu$s and L2 at $88\,\mu$s after the end of the drift time of the TPC, which is the slowest detector of ALICE, in order to prevent selecting pile-up events.

The software based High-Level Trigger (HLT) consists of up to 1000 multiprocessor PCs which analyze the complete event online and decide for example to select or reject an event, to store only the information of certain azimuthal sectors of interest, and compress the event information. The data acquisition (DAQ) system has a very large bandwidth of 1.25 GB/s to the permanent storage that is necessary to collect events with the desired data taking rate during the heavy-ion runs. This is realized with optical data links through the whole experiment, PCs and network switches in a highly parallel arrangement.

There are about 50 trigger classes. A trigger class is a combination of logical conditions of the trigger inputs (L0, L1 or L2) coming from the different detectors contributing to

the trigger system to select and characterize events. The trigger classes are grouped into two categories, those corresponding to rare processes and those corresponding to frequent processes. In order to prevent loosing any rare processes due to saturation of the temporary data storage in the DAQ, the trigger classes corresponding to the frequent processes can be disabled, if the occupation of this storage reaches a certain preset upper value. After a preset lower value is reached the trigger classes of the frequent processes are re-enabled.

3.3.4 Particle IDentification (PID)

The detectors that participate in the charged-particle identification in the central barrel are the ITS, the TPC, the TRD, the TOF and the HMPID. They perform best at different momentum ranges. The best PID is achieved by combining the information of several detectors. Four of the six layers of the ITS, the Silicon Drift and the Silicon Strip Detector can identify particles via their specific energy loss in the low-momentum range with a resolution of about 11 %. Figure 3.5 shows the specific energy loss in the ITS for different particle species. The black lines are the Bethe-Bloch parametrizations, which describe the energy loss as a function of momentum [53]. As one can see, this permits to distinguish pions from kaons up to about 450 MeV/c and protons from kaons up to about 1 GeV/c.

Also the TPC identifies charged particles exploiting the specific energy loss with an even better resolution of about 5.5 % in pp and 6.5 % in Pb–Pb collisions, depending slightly on the charged-particle density. The separation of the different particle species is very good at low momenta in the $1/\beta^2$ region of the Bethe-Bloch curves. With increasing momentum the separation gets worse until the Bethe-Bloch curves of the different particle species cross each other which is for example for pions and kaons at about 900 MeV/c, for pions and protons at about 1.6 GeV/c and for kaons and protons at about 2.2 GeV/c. After the crossing point the separation gets slightly better again due to the relativistic rise of the energy loss in the TPC gas until the Fermi plateau is reached at high momenta, where the energy loss is the same for all particles and a separation is no longer possible [53]. As the energy loss is proportional to z^2, nuclei with a charge of two have four times higher energy loss than particles with single charge. So, these nuclei can also at high momenta be separated from particles with a charge of one (see figure 3.6).

The TRD provides energy-loss information in the same momentum range as the TPC. Although the ionization in the TRD is larger than in the TPC due to the xenon-based counting gas, the resolution of the $\mathrm{d}E/\mathrm{d}x$ measurement is only about 18-20 % because of the limited track length. However, the main task of the TRD is to discriminate between

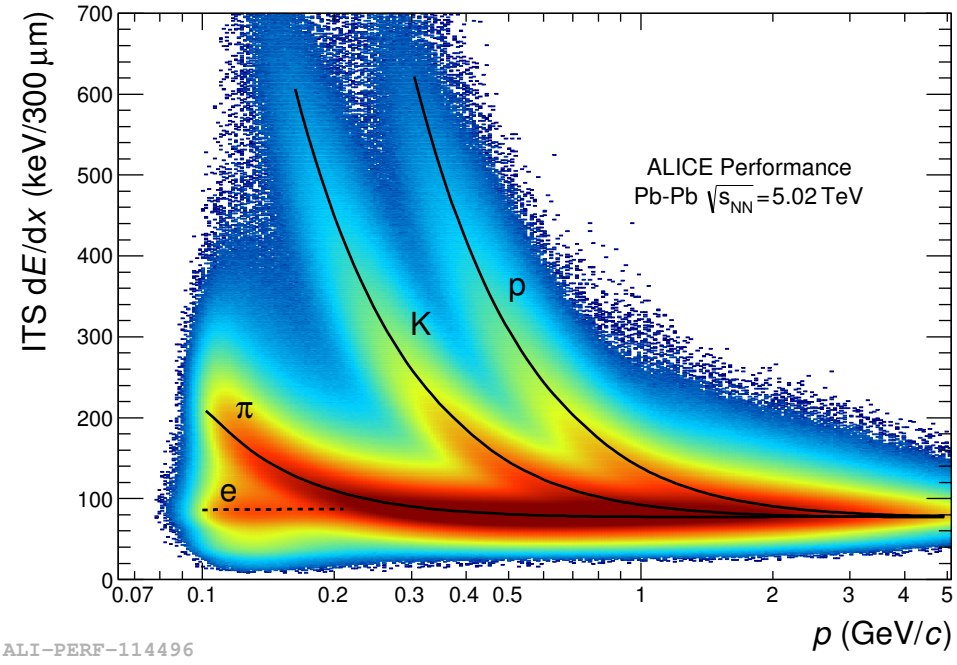

Figure 3.5: Specific energy loss ($\mathrm{d}E/\mathrm{d}x$) in the ITS versus momentum during the Pb–Pb data-taking period of 2015 [54].

electrons and pions via transition radiation. This is possible up to a few tens of GeV/c with an electron detection efficiency of about 90 %. The TRD can even operate on L1 trigger level.

At intermediate momenta, in the range between 0.9 and 3 GeV/c, where the PID using energy loss is not sufficient, the TOF detector is employed. It measures the particle's arrival time with a precision of 80 ps. Together with the information of track length, momentum and collision time, provided by ITS, TPC and T0, the velocity and the mass of the particle and so the identity can be determined. This extends the possible separation of pions and kaons up to 2.5-3 GeV/c and of kaons and protons up to 3.5-4 GeV/c (see figure 3.7). Some light nuclei can be seperated up to even higher momenta. In case of (anti)triton and (anti)^{4}He this will be discussed in more detail in chapter 4. The fact that in figure 3.7 are also entries of β above one is because flight times are matched to the wrong tracks and thus result in an incorrect β.

The HMPID further extends the PID of charged-particles to higher momenta, but only in a limited acceptance of about 10 % of the central barrel. It can identify protons up to 5 GeV/c.

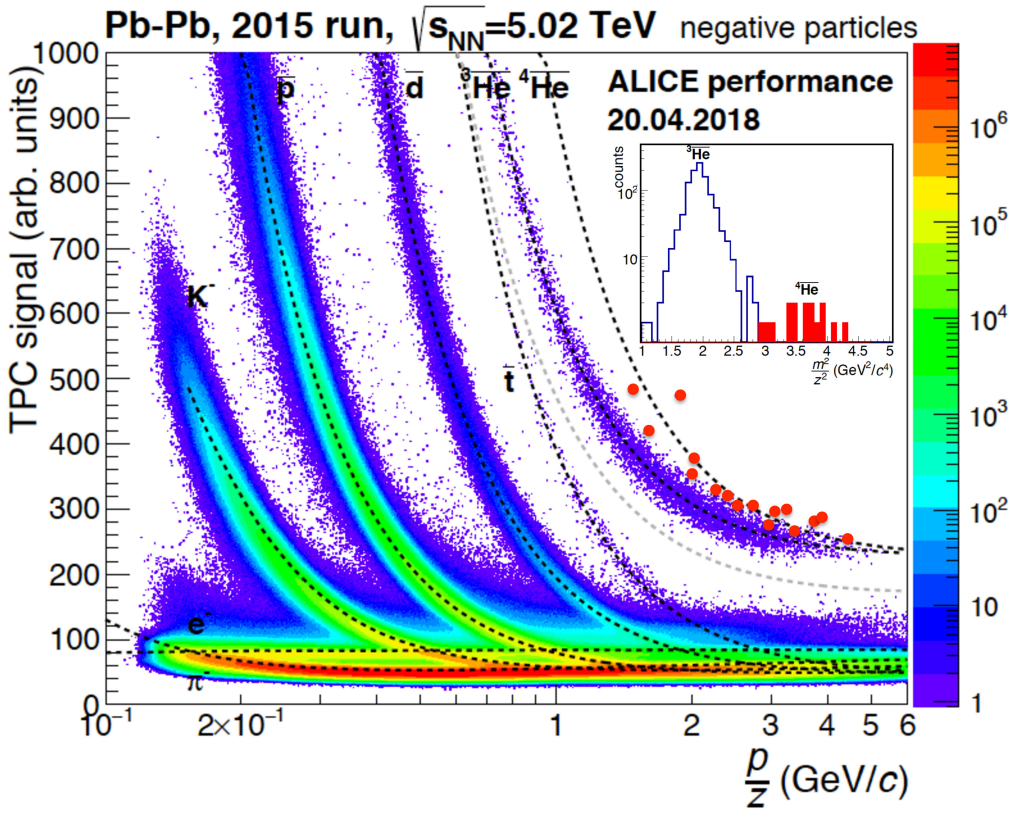

Figure 3.6: Specific energy loss ($\mathrm{d}E/\mathrm{d}x$) in the TPC versus rigidity for negative particles during the Pb–Pb data-taking period of 2015. Marked in red are the $^4\overline{\mathrm{He}}$ nuclei that were in addition identified with the TOF detector (see inlay) to discriminate them from the $^3\overline{\mathrm{He}}$ nuclei. The inlay shows the squared mass-to-charge ratio calculated from the velocity measured by the TOF detector and the momentum measured mainly by the TPC.

For the detection of π^0 and photons the PHOS is employed. It also only has a limited acceptance but measures photons with an excellent energy resolution of better than 5 %, improving with higher photon energies. With much larger acceptance but worse energy resolution by about a factor 2.5-3 the EMCal and DCal can measure neutral particles. In addition the PMD can count the number of photons that are produced in forward direction.

Muons are measured in the muon spectrometer with a tracking efficiency better than 95 % and a relative momentum resolution of about 1 %. The muon spectrometer also operates on trigger level.

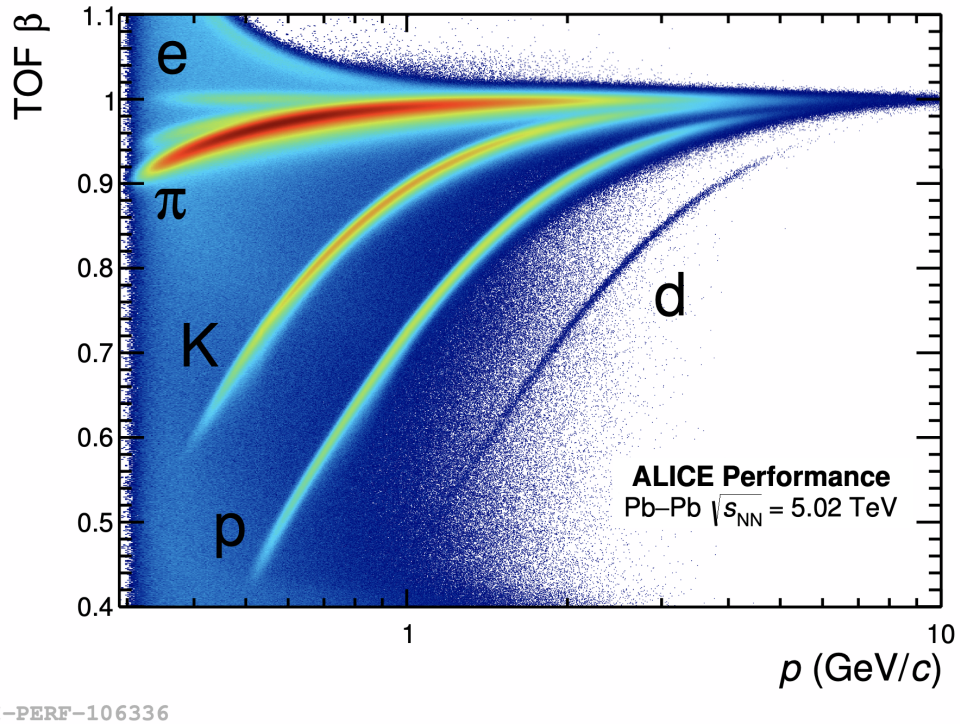

Figure 3.7: TOF β versus momentum measured during the Pb–Pb data-taking period of 2015 [55].

For the (anti)triton and (anti)^{4}He analyses presented in this work the dE/dx measurement of the TPC in combination with the time measurement of the TOF detector is applied. This is explained in more detail in section 4.4.

3.3.5 Upgrade

After the end of the LHC Long Shutdown 2 (LS2), anticipated in the beginning of 2022, the LHC will, after some month of pp data taking, increase its luminosity in Pb–Pb collisions progressively, reaching an interaction rate of 50 kHz which corresponds to $L = 6 \cdot 10^{27}\,\mathrm{cm}^{-2}\mathrm{s}^{-1}$. This made it irremissible to perform some major upgrades at the ALICE experiment, such that ALICE will be able to read out all interactions. It is planned that about 10^{11} Pb–Pb collisions will be accumulated during the Run 3 data-taking period. The upgrades include besides others a new beampipe with smaller diameter and an upgrade of the readout electronics of the TRD, the TOF detector and the muon spectrometer to enable high rate operation. In addition, two smaller detectors were newly installed during LS2, the Fast Interaction Trigger (FIT) detector and the Muon

Forward Tracker (MFT). The FIT is replacing the previous V0, T0 and AD detectors. Its purpose is to improve the centrality and event plane determination. The MFT is a vertex tracker at forward rapidity which is located in front of the front absorber. It will improve the momentum resolution for muons. The two main upgrades are, however, a renewal of the TPC readout chambers and the complete ITS.

The TPC is ALICE's slowest detector. Due to the gating grid in the TPC MWPCs the data taking rate was limited to about 3 kHz. The gating grid prevented the ions that were produced during gas amplification to drift back in the TPC drift volume. To cope with the much higher rate in the Run 3 data-taking period the readout chambers were replaced by stacks of four Gas Electron Multipliers (GEMs) [56], which have an intrinsic blocking of the back-drifting ions and so enable continuous data readout. How this is done is explained in more detail in chapter 6. With the exchange of the readout chambers also the front-end electronics had to be replaced [48].

The ITS was exchanged completely for a version with higher resolution and less material budget. From the reduced material thickness and the improved tracking precision and momentum resolution many physics analyses, primarily, heavy-flavour and low-mass dielectron measurements, will largely benefit. But in particular it will be possible to access lower momentum regions. The new ITS uses Monolithic Active Pixel Sensors (MAPS) which reduces the material budget per layer by a factor seven with respect to the previous ITS and also the pixel density could significantly be increased by about a factor of 50. In addition, the innermost layer is closer to the beamline which is possible due to the reduction of the beampipe diameter. The new ITS consists of seven concentric cylindrical layers of pixel detectors, the innermost layer has a radius of 22 mm and the outermost of 392 mm. The new ITS will not be able to measure the energy loss of the traversing particles and thus contribute to the PID anymore. It is assumed that the measurements that were using the ITS PID will be completed with the data sets of Run 2 [57].

4 (Anti)triton and (anti)^{4}He production

In this work the production of (anti)triton (t) and (anti)^{4}He in Pb–Pb collisions at a center-of-mass energy of $\sqrt{s_{\mathrm{NN}}} = 5.02\,\mathrm{TeV}$ measured by the ALICE experiment at the LHC was studied. Therefore transverse-momentum (p_{T}) spectra as well as p_{T}-integrated production yields and coalescence parameters B_3 and B_4 were extracted and compared to model calculations. In this chapter the different analysis steps are described in detail. The key aspect of these analyses is the particle identification. It is challenging for (anti)t and (anti)^{4}He because of slightly different reasons. Due to their large mass, in principle, both particles are rarely produced probes, so the size of the available data set is crucial. While (anti)^{4}He is even more rare than (anti)t it is, because of its charge of two, in the energy-loss measurement of the TPC well separated from the other particles with $z = 1$. However, the (anti)t has a charge of one and so it is at higher momenta in the TPC difficult to distinguish from the other particles. Even with the help of the TOF detector the signal is sitting on a huge background that is severely limiting the (anti)t analysis. While the (anti)t yield was extracted in four centrality intervals, the (anti)^{4}He yield was only extracted in the 0-10 % most central collisions. The detectors involved in both analyses are ITS, TPC, TRD and TOF.

4.1 Data sample

The data used for this analysis was taken in November 2018 by the ALICE experiment at the LHC. ^{208}Pb nuclei were collided with a center-of-mass energy ($\sqrt{s_{\mathrm{NN}}}$) of 5.02 TeV per nucleon pair. It was the second time in the LHC Run 2 period that Pb–Pb collisions at this energy were recorded, after the data sample LHC15o collected in the end of 2015. But this time more statistics was gathered. The data sample from 2018 consists of two periods, LHC18q and LHC18r, which have as sole difference an inversed magnetic field direction and were analyzed together. 126 runs were used from LHC18q, while 90 runs were used from LHC18r. A run is a time interval of uninterrupted data taking where beam and detector conditions are stable. These runs are selected based on the Run Condition Table (RCT) that is filled with quality assurance information provided by the different detector experts being part of the Data Preparation Group (DPG).

In the heavy-ion data gathered in 2015 (LHC15o) the selection of the recorded events was based on a minimum bias (MB) trigger, this means a coincident signal of both V0 detectors must be detected. In the LHC18q+r data sample the MB trigger was also running, but in addition it was triggered on central (CT2) and semi-central (CT1) events, also determined by the V0 detectors.

Event selection

For the event selection the standard ALICE event cuts for Pb–Pb collisions in Run 2 are used. To assure a uniform and symmetric acceptance of the detected events, only collisions with a position of their primary vertex within ±10 cm in beam direction from the center of the ALICE detector setup ($|V_z| < 10$ cm) are selected. This also rejects collisions with residual beam gas outside of this region. Furthermore, events with incomplete data acquisition (DAQ) are rejected.

Due to the high collision rates delivered by the LHC it can happen that more than one collision is detected during one readout phase of the TPC. This, so called pile-up, can happen with a very small probability in the same bunch crossing but mostly happens in different bunch crossings. Pile-up is unwanted, as then the created particles can eventually not be assigned to the correct collision. Therefore several pile-up rejection cuts are applied. If there is more than one primary collision vertex reconstructed with the SPD, the event is rejected. The vertices have to be reconstructed with more than a certain number of tracks to prevent that events are falsely rejected. If vertices are closer than 0.8 cm, it is considered as a single collision. In addition, pile-up is rejected based on the correlation of the two methods to estimate the centrality, the V0M and the SPD. Here the outlier region from the expected correlation between the two methods is cut away.

The event selection criteria are listed in table 4.1.

Table 4.1: Event selection criteria.

Criterion	Value	Reason
trigger	MB, CT1, CT2	desired centrality distribution
$\|V_z\|$	< 10 cm	uniform and symmetric acceptance
incomplete DAQ	rejected	complete information available
ΔV_z global and SPD	> 0.2 cm	quality of vertex
ΔV_z TPC and SPD	> 0.2 cm	quality of vertex
number of vertices in SPD	$= 1$	pile-up rejection

Centrality distribution

The overall number of events after event and physics selection in the LHC18q and LHC18r periods is 273.59 million. The physics selection selects only proper events, rejecting for example beam-gas events, pile-up and events without clear primary vertex determination. The centrality distribution of the data set is shown in figure 4.1. As can be seen the focus of the data taking was set to central collisions in the 0-10 % centrality interval, where particle production has its maximum, and a second focus to semi-central collisions in the 30-50 % centrality interval, where collective effects like elliptic flow can be studied best. Minimum bias data (0-90 %) has been taken with about the same number of events that was already taken in the Pb–Pb data set from 2015. The size of the LHC15o data set is about 90 million events evenly distributed from 0 to 90 %.

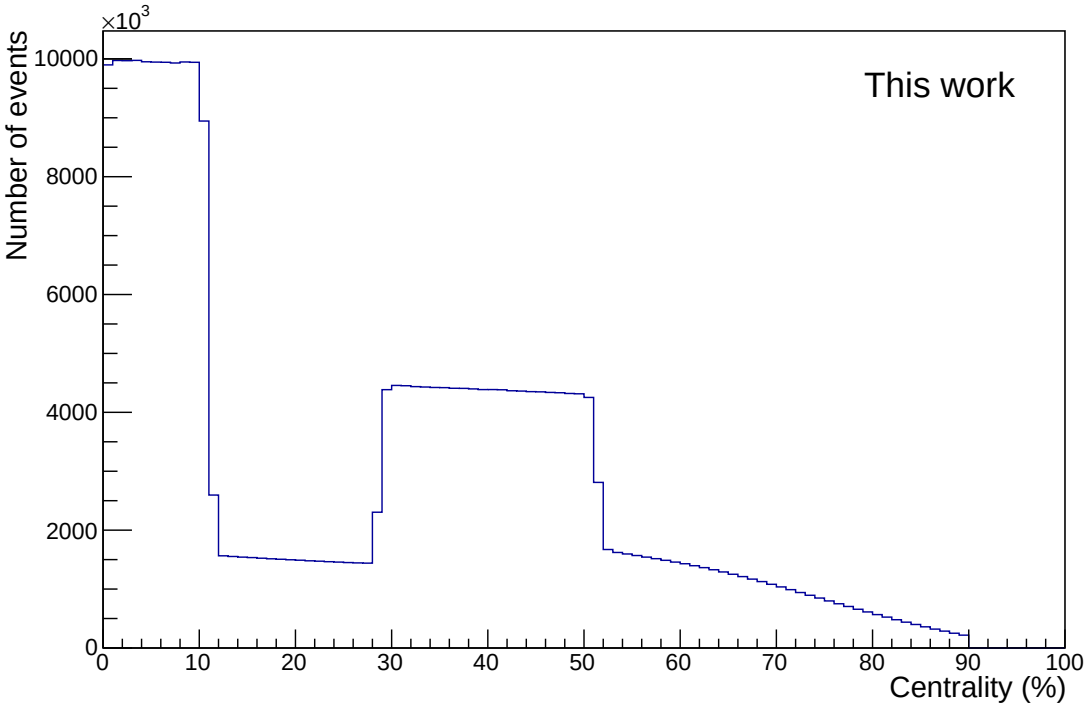

Figure 4.1: Centrality distribution in the 2018 data sample (LHC18q+r).

This centrality distribution suggests to perform the analysis in four centrality intervals, i.e. 0-10 %, 10-30 %, 30-50 % and 50-90 %. To perform an analysis in a certain centrality interval, the centrality distribution has to be flat in this interval to prevent any bias. As one can see in figure 4.1 this is not necessarily the case. While in the 0-10 % and 30-50 % centrality interval the structure is negligible as it is only a few percent, in the 10-30 %

centrality interval the distribution is higher at the edges and in the 50-90 % interval it is decreasing towards more peripheral collisions. So, the 10-30 % and 50-90 % centrality intervals were weighted with the average number of events in the centrality interval over the number of events in the respective centrality bin. As an example, if the average number of events in a centrality interval was 100 events per centrality bin and in one bin it was 200, this bin would be weighted with $\frac{1}{2}$. The number of events in the different centrality intervals of the LHC18q+r data set is listed in Table 4.2.

Table 4.2: Number of events in the different centrality intervals after event and physics selection in the LHC18q+r data sample.

Centrality interval	Number of events
0-90 %	273.59 million
0-10 %	99.47 million
10-30 %	42.16 million
30-50 %	87.72 million
50-90 %	44.24 million

4.2 Monte Carlo sample

To study the acceptance and efficiency of the detector setup, as well as the impact of the track cuts, a dedicated Monte Carlo (MC) simulation was produced for the LHC18q and LHC18r periods. The production is anchored to the runs of the data sample to reproduce the detector performance in each run. As MC simulations of heavy-ion collisions are very computing time consuming, and therefore expensive, the number of events in the MC sample is much less than in the data. In addition to optimize the computing time the MC sample was divided in three sub-samples (LHC20g7[a,b,c]) with different intervals of the impact parameter b, which is connected to the collision centrality. The ranges of the intervals were chosen from the centrality distribution of the real data.

The MC sample was produced with the HIJING event generator [58]. The detector simulation is based on the GEANT 4 transport code [59, 60, 61]. As in HIJING there are no nuclei produced, heavier nuclei and hyper-nuclei are on top injected in each event randomly with a flat distribution in p_{T} between 0 and 10 GeV/c and in rapidity between -1 and 1 ($\mid y \mid < 1$). In azimuthal angle ϕ the nuclei are also injected randomly with a flat distribution between 0 and $2\,\pi$.

The centrality distribution in the MC sample is shown in figure 4.2. Like in the real data the distribution is not flat. Therefore it was weighted in all four centrality intervals to obtain a flat centrality distribution.

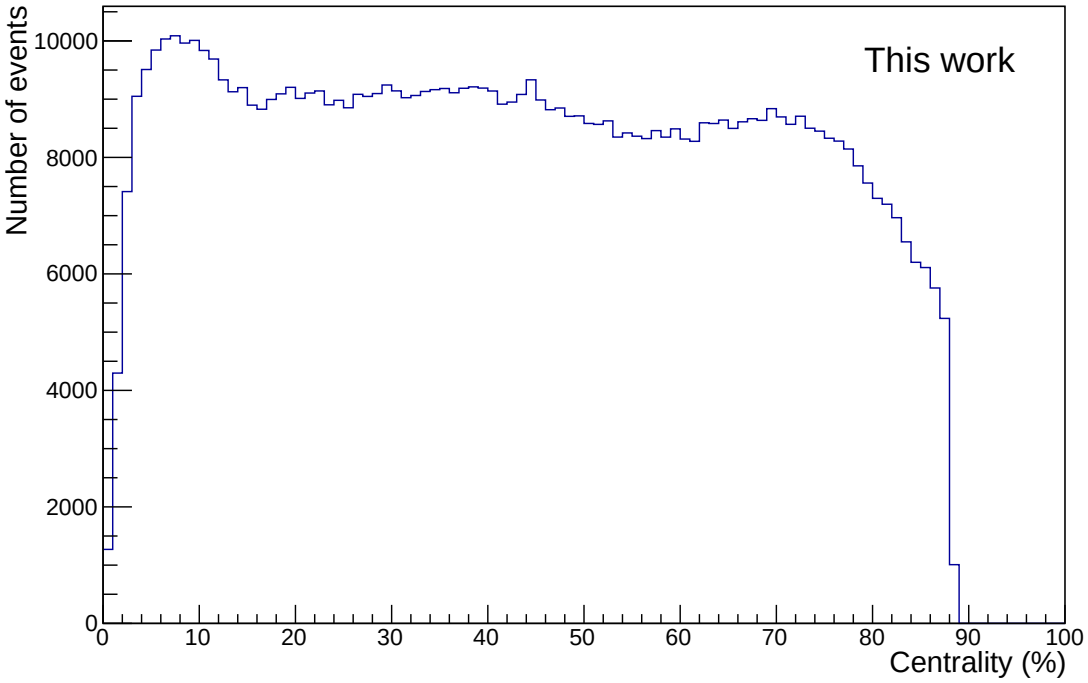

Figure 4.2: Centrality distribution in the used MC samples (LHC20g7a, b and c).

The efficiency correction also depends on the material budget of the detector setup as well as on the hadronic inelastic cross section. Both have an effect on how many particles are absorbed by the detector material or by the material of the support structure.

As the actual material budget of the detector setup is not completely known, a systematic uncertainty has to be assigned for this. There are two MCs (LHC17d5a and LHC17d5b), where the material budget has been varied up and down by 4.5 %. These MCs are anchored to the peripheral LHC15o data set. As it depends on the difference between the MCs, it is assumed that the centrality as well as the exact runs it is anchored to is not crucial. They were compared to the MC sample with nominal material budget anchored to the same data sample (LHC16h7c). All three MC samples were produced with the GEANT 3 transport code.

There is also an uncertainty on the hadronic inelastic cross section. In the MC productions LHC20i3[a,b,c][1,2,3] the hadronic inelastic cross section was increased and decreased by 50 %. a, b, c refers to the different cross sections (- 50 %, + 50 % and nominal), while 1, 2, 3 refers to the different centrality intervals (0-10 %, 10-50 % and 50-90 %). The MC productions are anchored to the LHC18q+r data set and use the GEANT 4 transport code. Only $^{3}\overline{\mathrm{He}}$ are injected in these MC productions, but it is assumed that

the uncertainty on the hadronic inelastic cross section is the same, due to the similar mass and size of $^3\overline{\mathrm{He}}$ and antitriton.

An overview of the different MC samples used is given in tables 4.3 and 4.4.

Table 4.3: Anchor period, impact parameter b, centrality, number of events N_{ev}, transport code and hadronic cross section of the different Monte Carlo productions.

MC period	Anchor period	b (nm)	Centr. (%)	N_{ev}	Tr. code	Hadr. CS
LHC20g7a	LHC18q+r	0-5	0-10	129538	GEANT4	nominal
LHC20g7b	LHC18q+r	5-11	10-50	431004	GEANT4	nominal
LHC20g7c	LHC18q+r	11-15	50-90	427956	GEANT4	nominal
LHC17d5a	LHC15o	11-15	50-90	444300	GEANT3	nominal
LHC17d5b	LHC15o	11-15	50-90	444240	GEANT3	nominal
LHC16h7c	LHC15o	11-15	50-90	355740	GEANT3	nominal
LHC20i3a1	LHC18q+r	0-5	0-10	12500	GEANT4	- 50 %
LHC20i3b1	LHC18q+r	0-5	0-10	12500	GEANT4	+ 50 %
LHC20i3c1	LHC18q+r	0-5	0-10	12500	GEANT4	nominal
LHC20i3a2	LHC18q+r	5-11	10-50	25000	GEANT4	- 50 %
LHC20i3b2	LHC18q+r	5-11	10-50	25000	GEANT4	+ 50 %
LHC20i3c2	LHC18q+r	5-11	10-50	25000	GEANT4	nominal
LHC20i3a3	LHC18q+r	11-15	50-90	25000	GEANT4	- 50 %
LHC20i3b3	LHC18q+r	11-15	50-90	25000	GEANT4	+ 50 %
LHC20i3c3	LHC18q+r	11-15	50-90	25000	GEANT4	nominal

Table 4.4: Number and species of injected nuclei per event and material budget of the different Monte Carlo productions.

MC period	Injected nuclei per event (+ charge conjugates)	Mat. budg.
LHC20g7a	$10 \times$ (d, t, ^{3}He, ^{4}He), $40 \times {}^3_\Lambda$H, $20 \times ({}^4_\Lambda$H, ${}^3_\Lambda$He)	nominal
LHC20g7b		nominal
LHC20g7c		nominal
LHC17d5a	$10 \times$ (d, t, ^{3}He, ^{4}He), $40 \times {}^3_\Lambda$H, $20 \times ({}^4_\Lambda$H, ${}^3_\Lambda$He)	+ 4.5 %
LHC17d5b		- 4.5 %
LHC16h7c		nominal
LHC20i3a1	$160 \times {}^3\overline{\mathrm{He}}$ (no ^{3}He)	nominal
LHC20i3b1		nominal
LHC20i3c1		nominal
LHC20i3a2		nominal
LHC20i3b2		nominal
LHC20i3c2		nominal
LHC20i3a3		nominal
LHC20i3b3		nominal
LHC20i3c3		nominal

4.3 Track selection

In each event it is checked for every track whether it satisfies the track selection criteria, also called track cuts. These criteria are listed in Table 4.5. They are a measure on how well the track reconstruction can be constrained.

Table 4.5: Track selection criteria. The cut on the TPC clusters used for PID is only applied for the (anti)triton analysis and not for (anti)^{4}He.

Selection	Value
Number of TPC clusters	> 70
TPC clusters used for PID (only (anti)triton)	>120
$\chi^2_{\mathrm{TPC}}/n_{\mathrm{TPCcluster}}$	< 4
TPC refit	On
ITS refit	On
TRD refit	On
Kink topologies	Reject
At least one hit on ITS layer	0 or 1
Track $\mid \eta \mid$	< 0.8
Track $\mid y \mid$	< 0.5

The first cut means that there have to be at least 71 track points measured in the TPC. The cut on the TPC clusters used for PID is only applied for (anti)t and not for (anti)^{4}He. It is the number of clusters that are used for the $\mathrm{d}E/\mathrm{d}x$ measurement in the TPC. This number has to be at least 121, which is a quite strong cut in order to reduce the (anti)t background. For (anti)^{4}He, where there is much less background, this cut would have negative effects on the anyways already small number of candidates. If this cut is used, the first one is redundant, as it is included in the latter one. The next cut describes the quality of the fit to these track points that determines the trajectory of the particle. The next three cuts, the requirement of TPC, ITS and TRD refit, are also a quality feature of the fit to the track points. It requires that the tracks can be fitted several times in inward and outward direction which also shows how well the track points of the different detectors can be connected. A further cut rejects tracks that have a kink topology, these tracks come from weak decays, where the mother particle decays in a charged and a neutral daughter particle. As a neutral particle can not be detected in the TPC, the topology looks like one track having a kink. The selection criterion on at least one hit in the inner most or second inner most ITS layer is a measure on how well the particle can be tracked back to the collision vertex, as the ITS is the inner most detector of ALICE. The cut on the pseudorapidity ($\mid \eta \mid < 0.8$) is a purely geometrical one that constrains the track to the active volume of the TPC and favours the midrapidity region.

The rapidity y is defined as:

$$y = \frac{1}{2} \cdot \ln\left(\frac{E + p_z}{E - p_z}\right) \tag{4.1}$$

To determine the rapidity the energy of the particle is needed and therefore the mass or identity of the particle must be known. For very light particles, where the mass can be neglected with respect to their momentum, rapidity and pseudorapidity are nearly identical. For nuclei this is of course not the case. The rapidity has the substantial property that it is additive under Lorentz transformation. The constraint to one unit of rapidity ($\mid y \mid < 0.5$) favours the midrapidity region and has the advantage that the yield is in the end automatically normalized to one unit of rapidity.

4.4 Raw spectra extraction

For the particle identification of the (anti)tritons and (anti)^{4}He a combination of the TPC and the TOF detector is used. In the TPC the specific energy loss of the particles versus rigidity (p/z) is measured. In figure 4.3 it is shown for deuterons, tritons, ^{3}He and ^{4}He for the full statistics of the LHC18q+r data set, particles and antiparticles together. A loose cut was applied to suppress the lighter particles. The red lines represent the parameterization of the Bethe-Bloch curves fitted to the particle bands, they are defined as the expected signal for the TPC PID. For the fit the ALEPH parametrization of the Bethe-Bloch formula is used [53]:

$$f(\beta\gamma) = \frac{P_1}{\beta^{P_4}} \left[P_2 - \beta^{P_4} - \ln\left(P_3 + \frac{1}{(\beta\gamma)^{P_5}} \right) \right] \tag{4.2}$$

This expression only depends on $\beta\gamma$ and the five parameters P_1 to P_5 which depend on the crossed material and are determined by the fit. They are different for nuclei with $z = 1$, like (anti)t, and nuclei with a $z = 2$, like (anti)^{4}He and are shown in Table 4.6. It was also checked for LHC18q and LHC18r that the parameters are the same for both periods.

The energy loss for $z = 2$ particles is four times higher than for $z = 1$ particles. Therefore they are nicely separated in the TPC, as can also be seen in figure 4.3.

In figure 4.4 the energy loss in the TPC is shown for particles and antiparticles separately. One can clearly see that there are much more particles than antiparticles at low momenta. This excess is not coming out of the collision as particles and antiparticles are created equally at LHC energies. These nuclei are coming from the beryllium beampipe and the detector material and are knocked-out by (anti)particles coming out of the

Table 4.6: Bethe-Bloch parameters of the ALEPH parametrization for nuclei with $z = 1$ and $z = 2$ in the LHC18q+r data set.

Parameters	Nuclei with $z = 1$ ((anti)t)	Nuclei with $z = 2$ ((anti)^{4}He)
P_1	0.648689	1.70184
P_2	56.6706	28.4426
P_3	-1.63243 10^{-10}	3.21871 10^{-12}
P_4	2.46921	2.06952
P_5	16.8531	2.77971

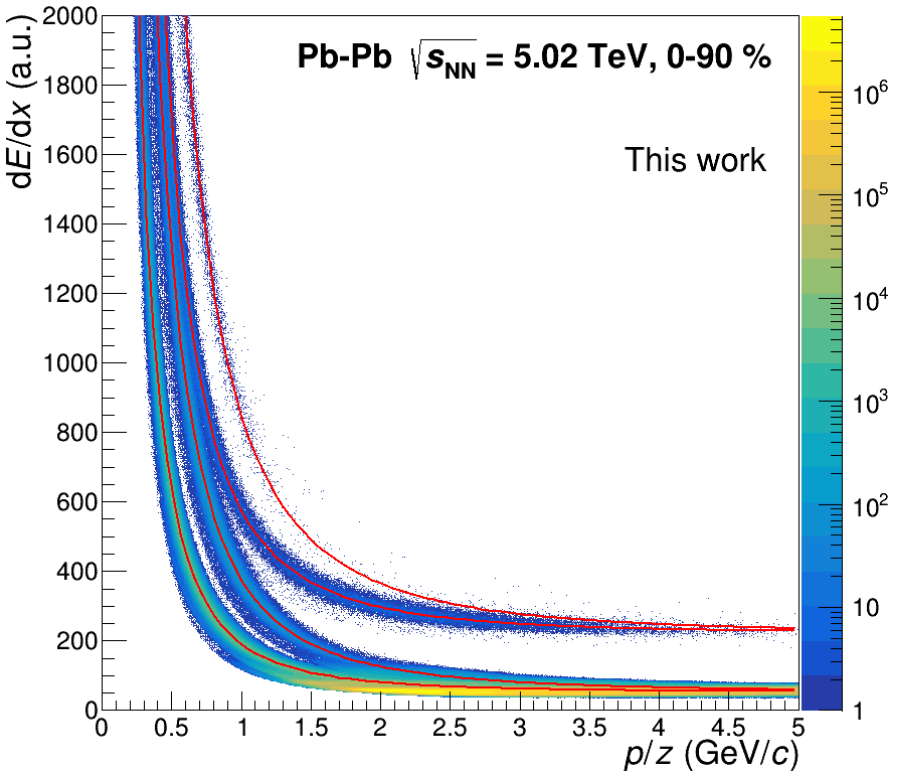

Figure 4.3: Specific energy loss in the TPC versus rigidity (from left to right) for deuterons, tritons, ^{3}He and ^{4}He in Pb–Pb collisions at $\sqrt{s_{\mathrm{NN}}} = 5.02\,\mathrm{TeV}$ for particles and antiparticles together (LHC18q+r, 0-90 %). The red lines represent the fitted Bethe-Bloch curves.

collision. This process is often called spallation or knock-out. In figure 4.4(b) only few $^4\overline{\mathrm{He}}$ are visible around the red ^{4}He Bethe-Bloch curve.

As from about 2 GeV/c the triton band becomes indistinguishable from the deuteron band and the ^{4}He band becomes indistinguishable from the ^{3}He band, in addition, the TOF information has to be used for the PID. The TOF detector provides the time-of-

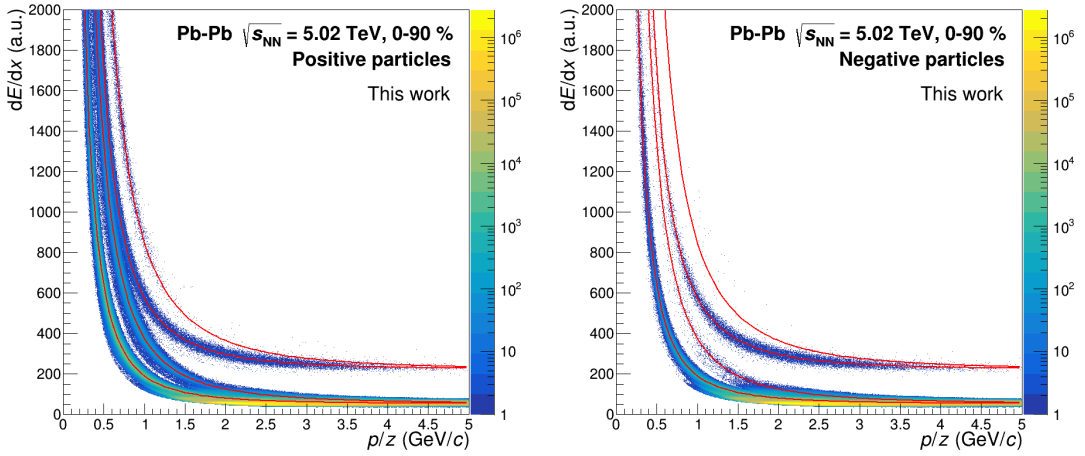

(a) Particles, 0-90 % centrality interval.

(b) Antiparticles, 0-90 % centrality interval.

Figure 4.4: Specific energy loss in the TPC versus rigidity (from left to right) for deuterons, tritons, ^{3}He and ^{4}He in Pb–Pb collisions at $\sqrt{s_{\mathrm{NN}}} = 5.02\,\mathrm{TeV}$ (LHC18q+r) for particles on the left and antiparticles on the right in the 0-90 % centrality interval. The red lines represent the fitted Bethe-Bloch curves.

flight t_{TOF} of a particle. With the additional information of the track length L and the momentum p, determined from the track curvature, the velocity β and the particle mass m are calculated:

$$\beta = \frac{L}{t_{\mathrm{TOF}} \cdot c} \tag{4.3}$$

$$m = \frac{\sqrt{1-\beta^2}}{\beta} p \tag{4.4}$$

4.4.1 (Anti)triton candidates selection and PID

In order to select the (anti)triton candidates, a $2\,\sigma$ cut around the (anti)triton line is done in the TPC, then the m^2/z^2 is calculated with the TOF information. The $2\,\sigma$ instead of a $3\,\sigma$ cut in the TPC is done in order to improve the signal-over-background ratio. The m^2/z^2 distribution versus transverse momentum for antitritons is shown in figure 4.5 for the four centrality intervals. The m^2 of the (anti)triton is $7.89\,\mathrm{GeV}^2/c^4$. Nevertheless, there is a huge background visible over the whole m^2 range starting at about 2 GeV/c, exactly where the (anti)triton band in the TPC is running in the other particle bands. This background is coming from mismatches in the TOF detector. This means, that

a hit in the TOF detector is matched to the wrong track with a different momentum, which then results in a wrong (not existing) particle mass. One can see that for central collisions the plot is more crowded, signal, as well as background, is higher than for the more peripheral collisions. However, it cannot exactly be compared on these plots, as the number of events is different in the different centrality intervals, as was already shown in table 4.2.

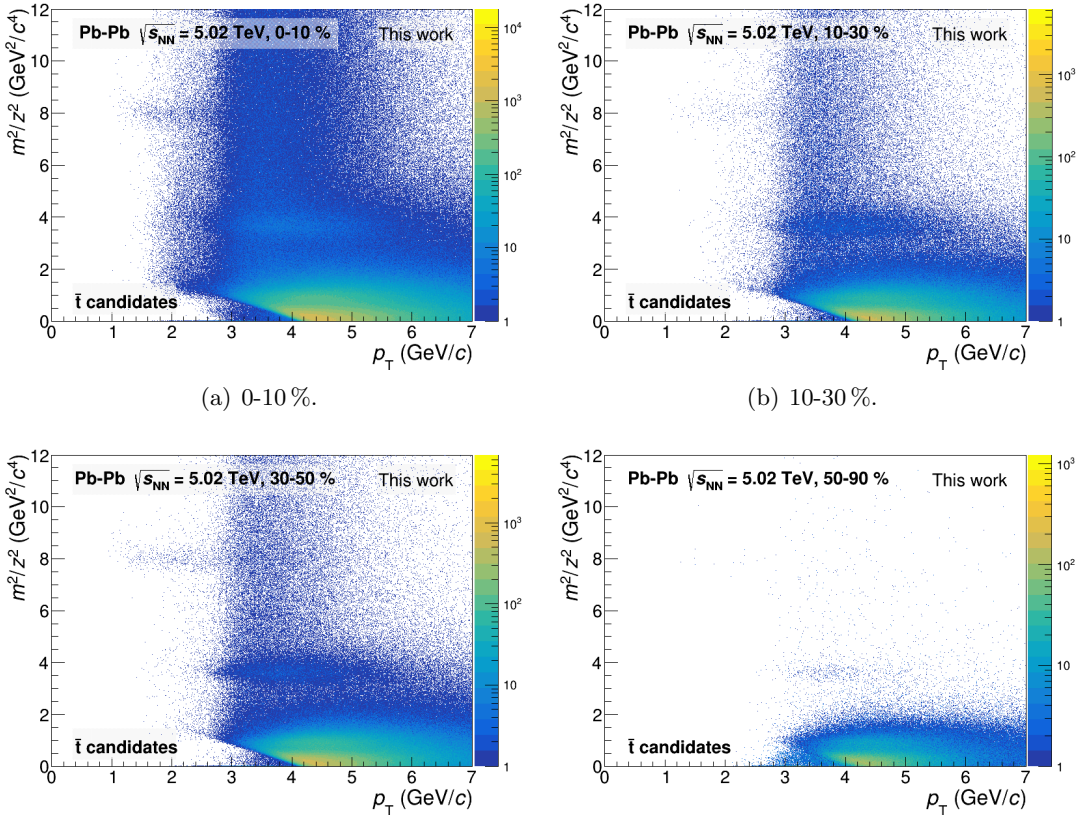

(a) 0-10 %. (b) 10-30 %.

(c) 30-50 %. (d) 50-90 %.

Figure 4.5: m^2/z^2 distribution of the TOF detector versus p_T for antitritons in the four centrality intervals ($m_t^2 = 7.89\,\mathrm{GeV}^2/c^4$). A $\mid n\sigma_{\mathrm{TPC}}(\mathrm{t}) \mid < 2$ selection around the (anti)triton band in the TPC has been done before. The background is clearly visible over the whole m^2 range starting from about 2 GeV/c.

Looking at the corresponding plot for the tritons (see figure 4.6) there is in addition at low p_T a significant contribution visible from knocked-out tritons coming from the beam pipe or the detector material, as already mentioned before and can also be seen in figure 4.4. This contribution is several times as much as the actual signal. For this reason the triton yield is only extracted for p_T larger than 2 GeV/c.

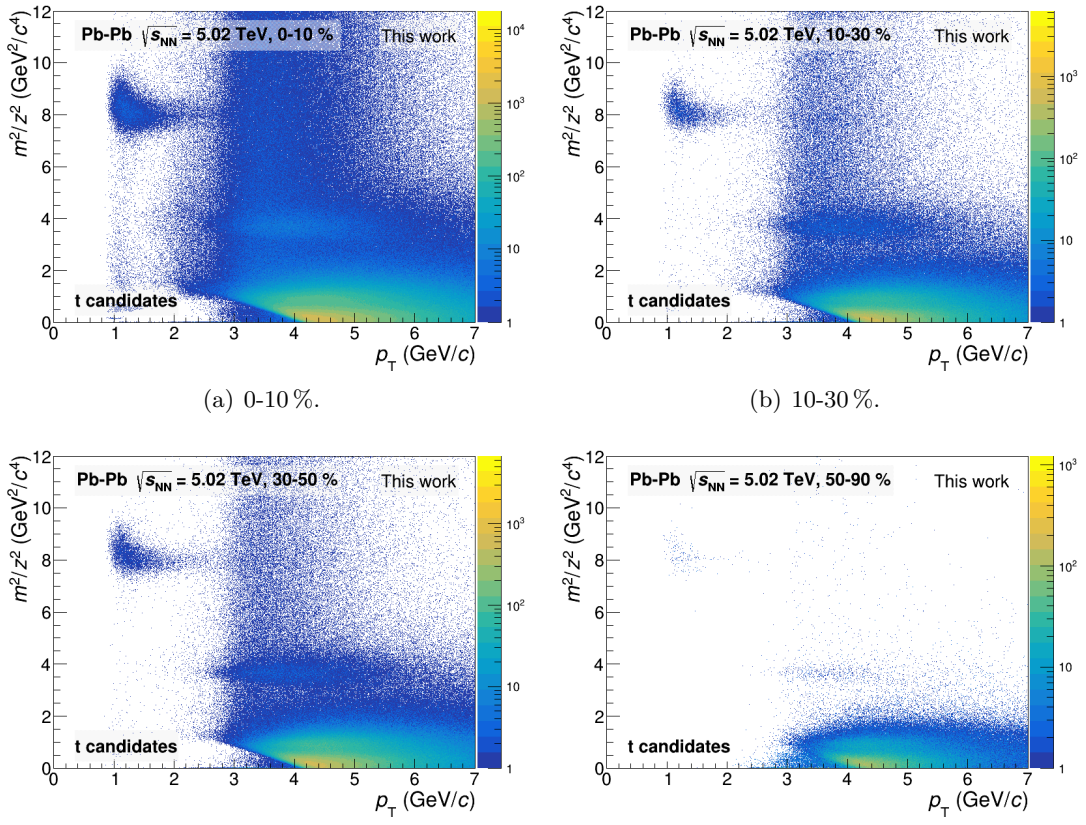

(a) 0-10 %. (b) 10-30 %.

(c) 30-50 %. (d) 50-90 %.

Figure 4.6: m^2/z^2 distribution of the TOF detector versus p_T for tritons in the four centrality intervals ($m_t^2 = 7.89\,\mathrm{GeV}^2/c^4$). A $|\, n\sigma_{\mathrm{TPC}}(\mathrm{t}) \,| < 2$ selection around the (anti)triton band in the TPC has been done before. The background is clearly visible over the whole m^2 range starting from about 2 GeV/c. In comparison to the antitritons there is a significant contribution visible at low p_T from knocked-out tritons coming from the beam pipe or the detector material.

The contribution from the material knock-out can also be seen in figure 4.7 where the Distance-of-Closest-Approach from the vertex in the x-y plane (DCA_{xy}) versus p_{T} is shown for tritons in the four centrality intervals. For tritons coming from material a broad distribution in DCA_{xy} is expected and also observed as these tritons do not come from the primary vertex. This broad distribution is seen up to about 2 GeV/c.

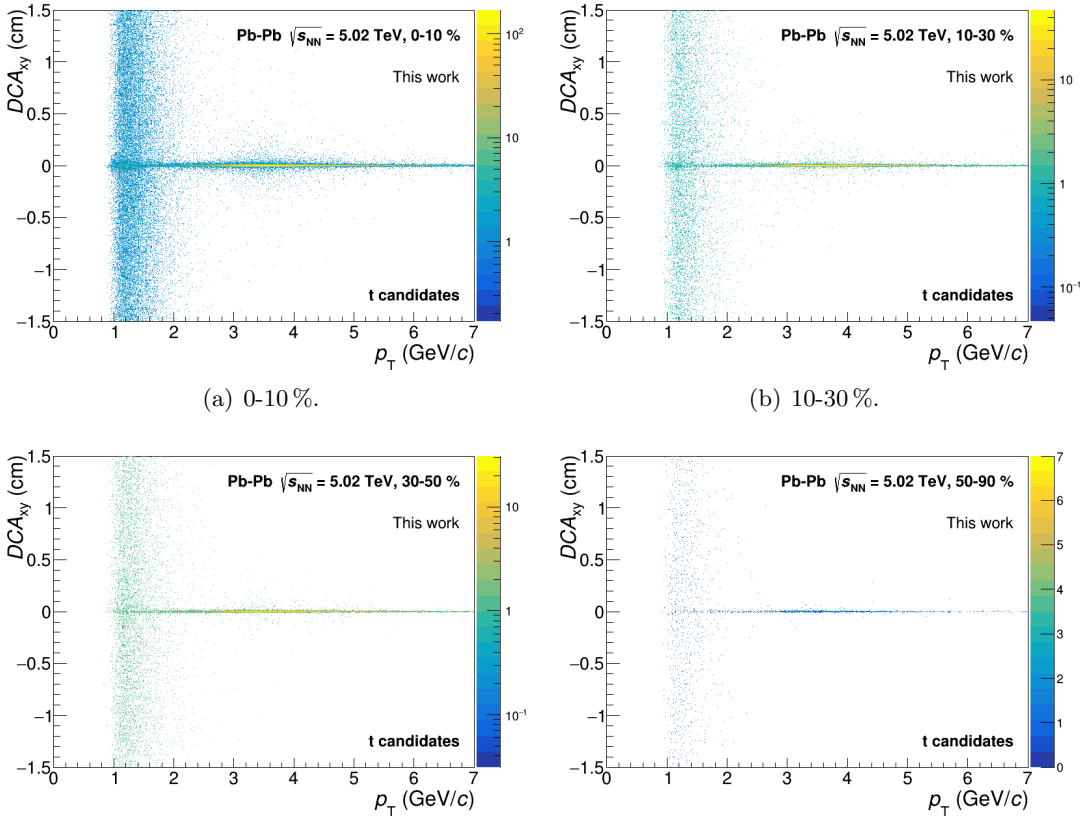

(a) 0-10 %. (b) 10-30 %.

(c) 30-50 %. (d) 50-90 %.

Figure 4.7: DCA_{xy} versus p_{T} for tritons in the four centrality intervals. The broad distribution at low p_{T} indicates the large contribution from material knock-out (spallation) up to about 2 GeV/c.

The analysis is done in p_{T} bins of 0.4 GeV/c from 0.8 to 3.2 GeV/c for the antitritons and from 2.4 to 3.2 GeV/c for the tritons. In the most peripheral centrality interval (50-90 %) the triton yield is extracted from 2.0 to 3.2 GeV/c as there is less contribution from material knock-out. Below 0.8 GeV/c the tritons do not reach the TOF detector and above 3.2 GeV/c the background is too dominant to extract a signal.

From the plots in figure 4.5 and 4.6 slices in p_{T} are projected on the m^2/z^2 axis (see figures 4.9 to 4.12). Figure 4.8 shows the m^2/z^2 distribution for antitritons exemplarily

in two p_{T} bins of the 0-10 % centrality interval. In blue an exponential + gauss · exponential fit to the m^2/z^2 distribution is shown. The exponential is supposed to describe the background, the gauss · exponential describes the signal as the TOF signal has an exponential tail. As a fit does not seem to describe the background very well an alternative method was tried. The magenta background is determined by selecting all tracks in the TPC outside the $2\,\sigma$ (anti)triton band. Like this a background template is created. Then this template is scaled to the height of the (anti)triton histogram (green). Using a template to estimate the background is an independent, data driven method with only one free parameter, the scaling factor. The scaling factor f is determined by dividing the (anti)triton histogram by the background histogram and then fitting a constant to a sideband (5 to 6.5 GeV/c) between the (anti)deuteron and the (anti)triton m^2. This constant is then used as scaling factor. One can see that the shape fits very well and with this method the background is constrained over a broader range than it is possible with a fit to the (anti)triton histogram.

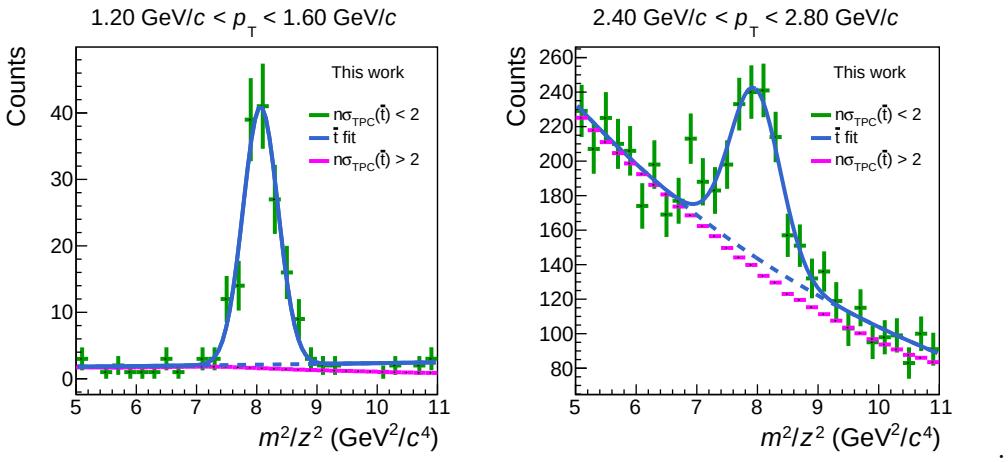

Figure 4.8: m^2/z^2 distribution of antitritons ($|\,\mathrm{n}\sigma_{\mathrm{TPC}}(\mathrm{t})\,| < 2$, green) with fit (exponential + gauss · exponential, blue) and scaled background ($|\,\mathrm{n}\sigma_{\mathrm{TPC}}(\mathrm{t})\,| > 2$, magenta) exemplary for two p_{T} bins of the 0-10 % centrality interval.

However, a close inspection reveals that in the last p_{T} bins between 2.8 and 3.2 GeV/c, especially in the 0-10 % centrality interval (figures 4.9(a) and 4.11(a)), there is a discrepancy from the template on the right side of the peak, whereas on the left side the template describes the background very well. The reason for that is not yet finally understood.

The template method to determine the background is used for all four centrality intervals (see figures 4.9 to 4.12), whereas in the 0-10 % centrality interval no background is subtracted in the first p_{T} bin, in the 10-30 % and 30-50 % centrality intervals no back-

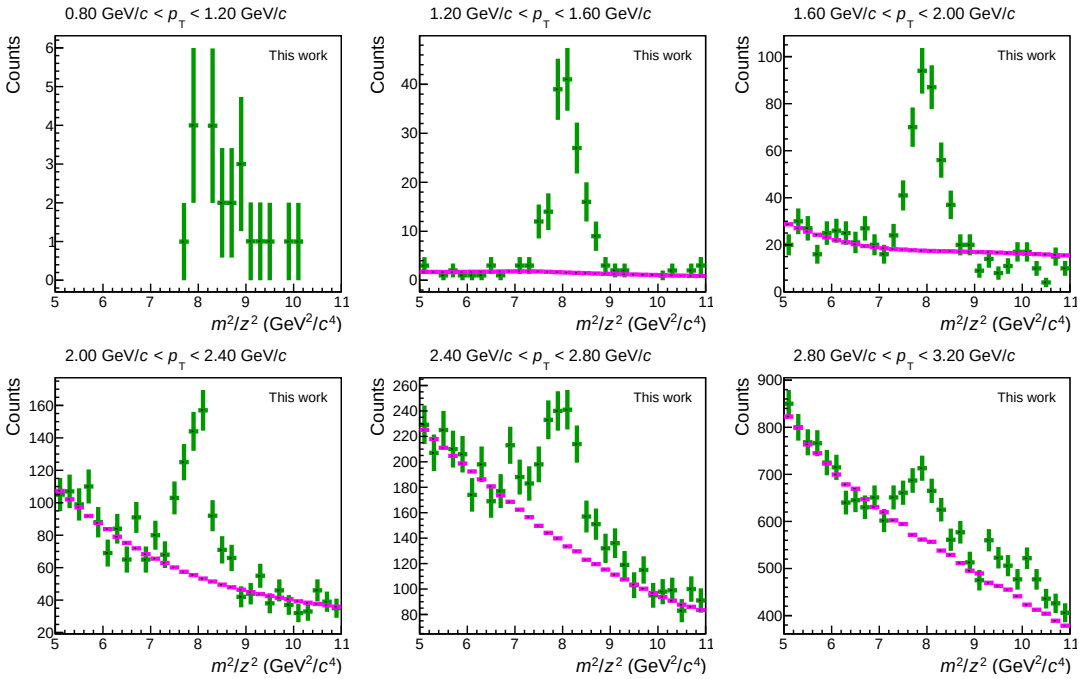

(a) 0-10 %.

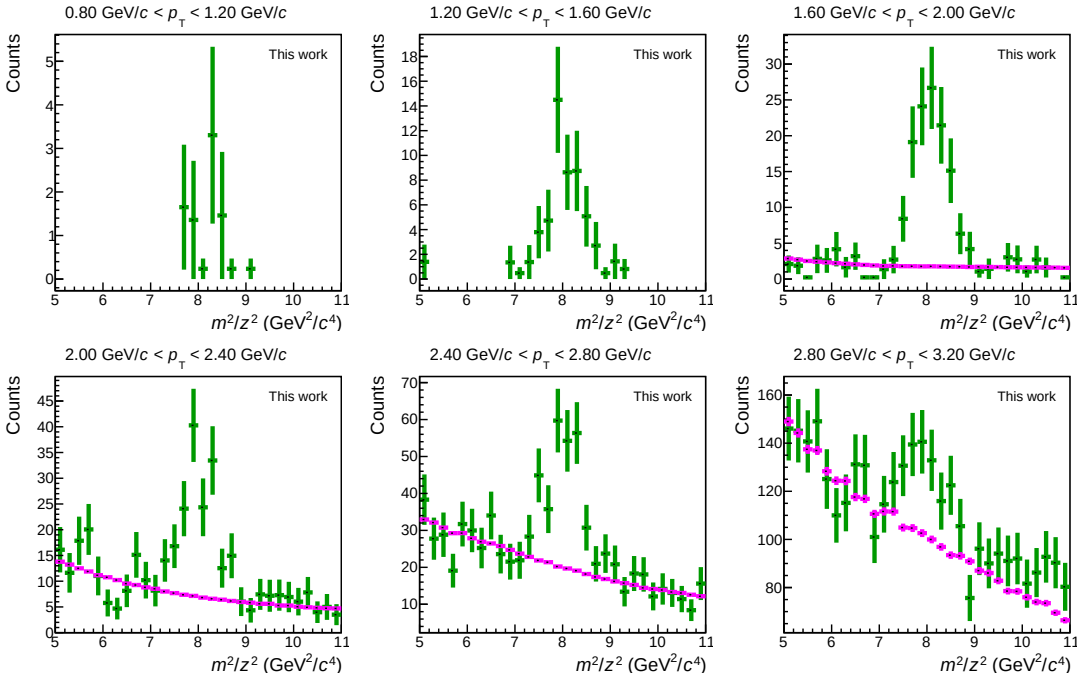

(b) 10-30 %.

Figure 4.9: m^2 distribution of antitritons ($|\ n\sigma_{\mathrm{TPC}}(t)\ | < 2$, green) and scaled background ($|\ n\sigma_{\mathrm{TPC}}(t)\ | > 2$, magenta) for the different p_{T} bins in the 0-10 % (top) and 10-30 % (bottom) centrality interval.

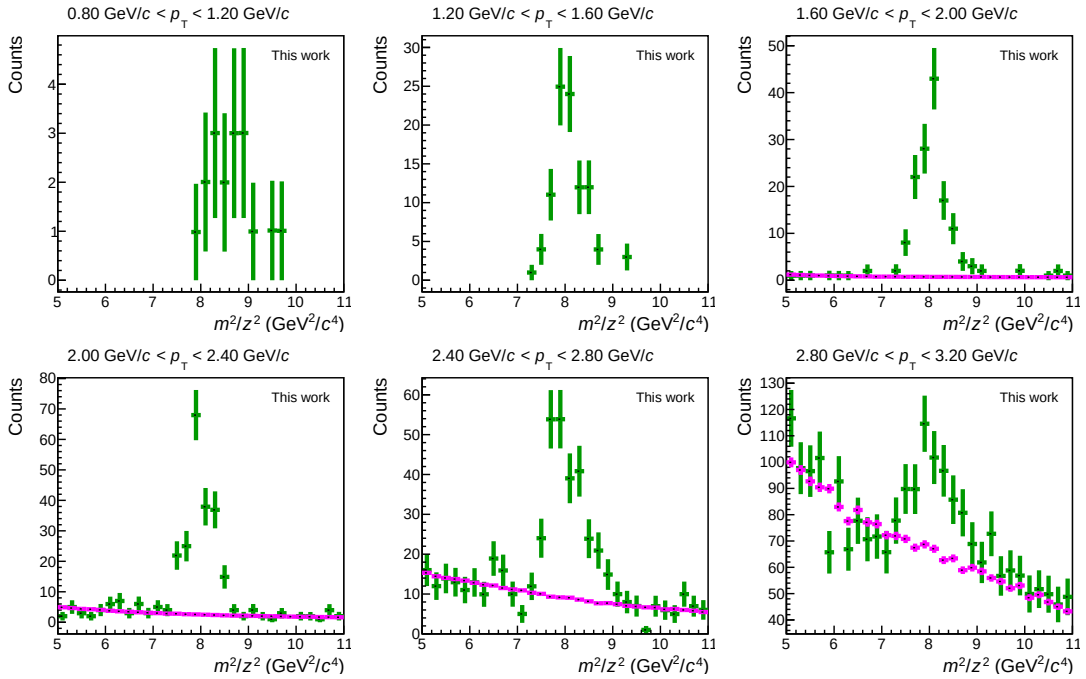

(a) 30-50 %.

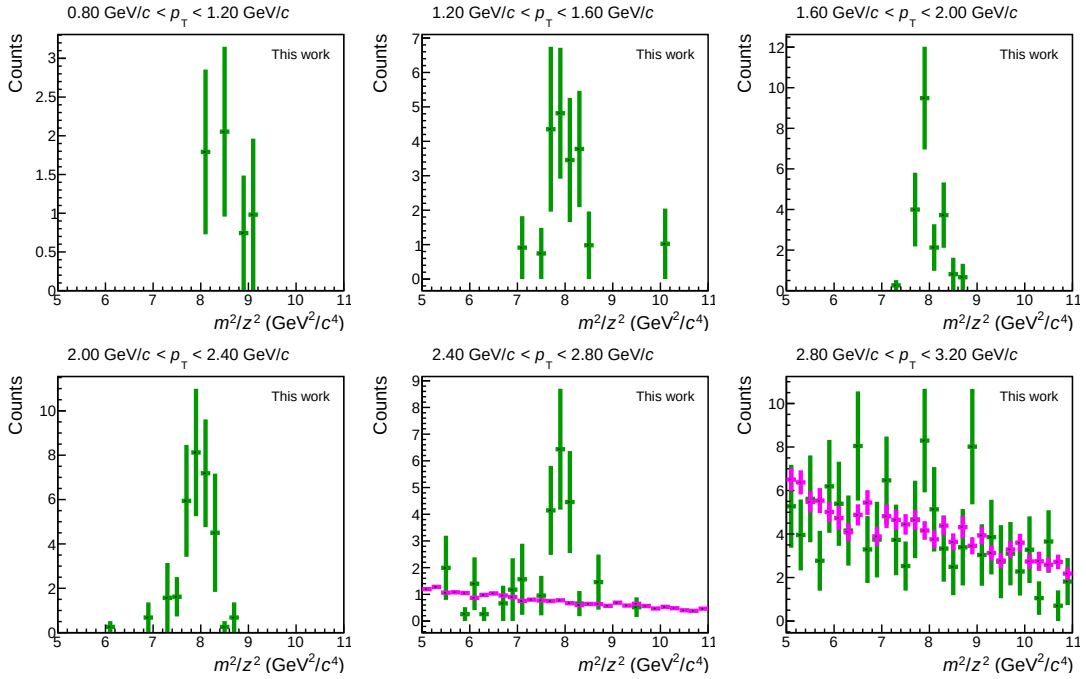

(b) 50-90 %.

Figure 4.10: m^2 distribution of antitritons (| nσ_{TPC}(t) |< 2, green) and scaled background (| nσ_{TPC}(t) |> 2, magenta) for the different p_{T} bins in the 30-50 % (top) and 50-90 % (bottom) centrality interval.

ground is subtracted in the first two p_{T} bins, and for the 50-90 % centrality interval for the first four p_{T} bins no background is subtracted.

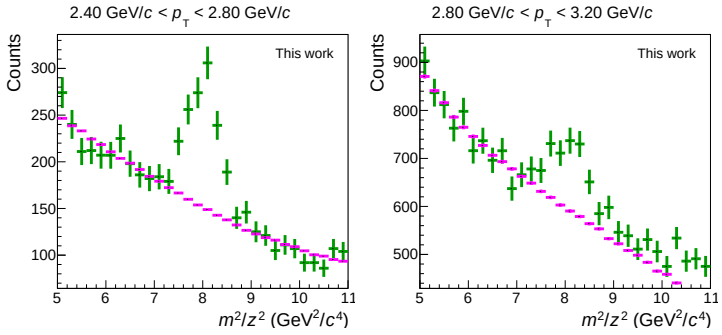

(a) 0-10 %.

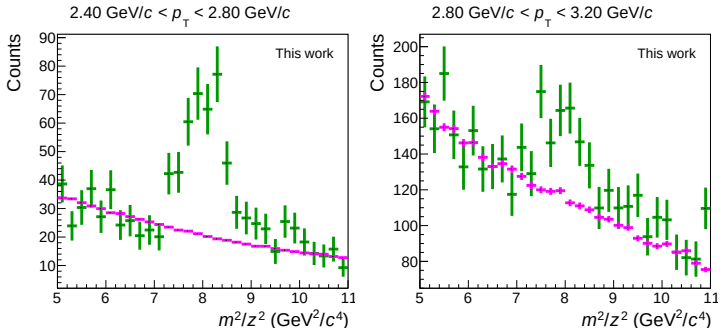

(b) 10-30 %.

Figure 4.11: m^2 distribution of tritons (| nσ_{TPC}(t) |< 2, green) and scaled background (| nσ_{TPC}(t) |> 2, magenta) for the different p_{T} bins in the 0-10 % (top) and 10-30 % (bottom) centrality interval.

The raw yield is extracted by counting the entries in the (anti)triton histogram between 6.99 and 8.79 GeV$^2/c^4$ and then subtracting the scaled background in this region. Here it is assumed that the σ of a potential Gaussian fit would be 0.3. The resolution of the TOF detector becomes worse with higher p_{T}, so the m^2 distribution should become broader, the σ of a Gaussian fit larger. Due to the dominant background, this is not the case for the m^2 distribution of (anti)tritons. No reasonable values could be obtained with a fit, however the σ were lying around 0.3 and this also seemed reasonable looking at the distributions. Thus an interval of $\pm 3 \cdot 0.3\,\mathrm{GeV}^2/c^4$ around the (anti)triton m^2 was chosen to extract the (anti)triton signal.

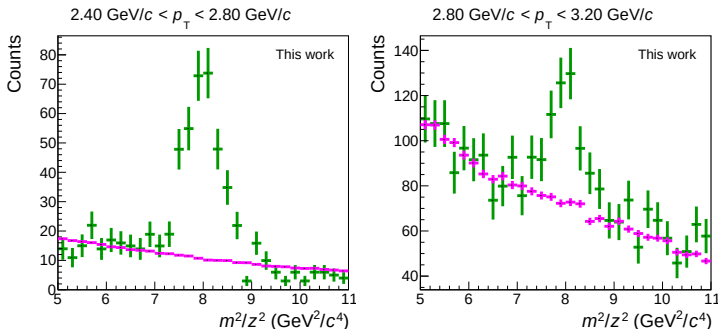

(a) 30-50 %.

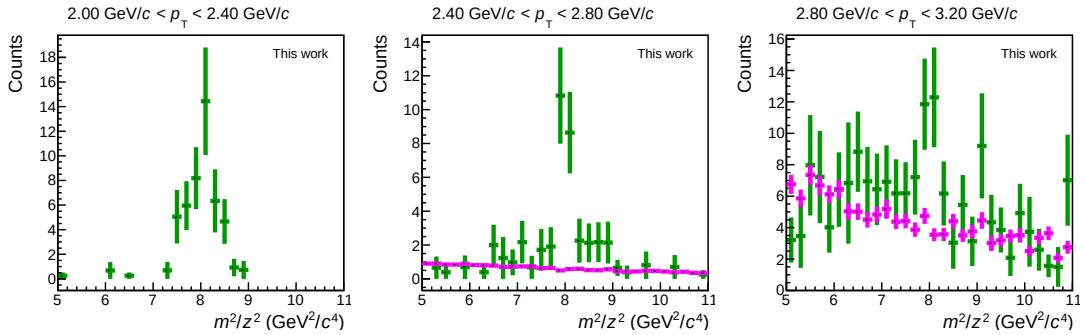

(b) 50-90 %.

Figure 4.12: m^2 distribution of tritons ($|\ \mathrm{n}\sigma_{\mathrm{TPC}}(\mathrm{t})\ | < 2$, green) and scaled background ($|\ \mathrm{n}\sigma_{\mathrm{TPC}}(\mathrm{t})\ | > 2$, magenta) for the different p_{T} bins in the 30-50 % (top) and 50-90 % (bottom) centrality interval.

As already mentioned earlier, the $2\,\sigma$ instead of a $3\,\sigma$ cut in the TPC $\mathrm{d}E/\mathrm{d}x$ is done in order to improve the signal-over-background ratio (S/B). This is shown in table 4.7. It is taken into account later in the acceptance and efficiency correction (see section 4.5) to determine the corrected yield by applying the same cut in Monte Carlo.

Table 4.7: Signal-over-background ratio for a $2\,\sigma$ and $3\,\sigma$ selection around the (anti)triton band in the TPC for the 0-10 % centrality interval and different p_{T} bins.

Antitritons			
Centrality (%)	p_{T} (GeV/c)	S/B ($2\,\sigma$)	S/B ($3\,\sigma$)
0-10	1.20-1.60	8.94	4.33
	1.60-2.00	1.61	0.61
	2.00-2.40	0.70	0.30
	2.40-2.80	0.41	0.15
	2.80-3.20	0.12	0.05

The statistical uncertainty of the signal is calculated by $\sqrt{S+B+f*B'}$ where $S+B$ is the triton histogram, B' is the scaled background and f is the scaling factor. The difference of taking the scaled background for the statistical uncertainty into account or not, as well as the raw signal (S) itself, the signal-over-background ratio (S/B) and the significance ($S/\sqrt{S+B+f*B'}$) of the signal, is shown in table 4.8 for the different centrality intervals and p_{T} bins. The scaled background introduces practically no additional statistical uncertainty.

The raw spectra of tritons and antitritons with statistical uncertainties are shown in figure 4.13 for all four centrality intervals.

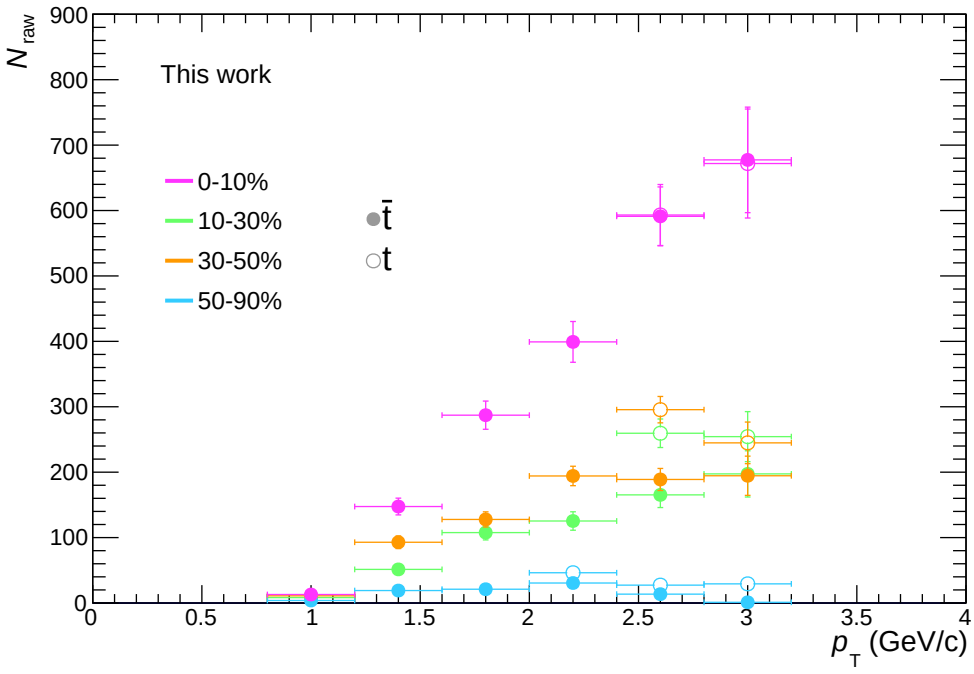

Figure 4.13: Raw spectra of tritons and antitritons with statistical uncertainties shown as vertical error bars. The horizontal error bars represent the bin width.

Table 4.8: Signal and statistical uncertainties for the different centrality intervals and p_{T} bins, using once only signal (S) + background (B) and once signal, background and the scaled background B' (scaled by f). Also the signal-over-background ratio and the significance are stated.

Cent. (%)	p_{T} (GeV/c)	S	$\sqrt{S+B+f*B'}$	$\sqrt{S+B}$	S/B	Signif.
			Antitritons			
0-10	0.80-1.20	12.98	–	–	–	3.60
	1.20-1.60	147.49	12.81	12.81	8.94	11.52
	1.60-2.00	287.13	21.56	21.56	1.61	13.32
	2.00-2.40	399.18	31.17	31.16	0.701	12.81
	2.40-2.80	591.14	44.96	44.92	0.41	13.15
	2.80-3.20	677.41	80.66	79.96	0.12	8.40
10-30	0.80-1.20	8.24	–	–	–	2.87
	1.20-1.60	51.37	–	–	–	7.17
	1.60-2.00	107.64	11.20	11.20	6.01	9.61
	2.00-2.40	125.36	14.10	14.10	1.71	8.89
	2.40-2.80	165.30	19.36	19.35	0.79	8.54
	2.80-3.20	197.38	35.34	35.03	0.19	5.59
30-50	0.80-1.20	10.99	–	–	–	3.32
	1.20-1.60	92.88	–	–	–	9.64
	1.60-2.00	127.74	11.62	11.62	17.45	10.99
	2.00-2.40	194.21	14.85	14.85	7.40	13.08
	2.40-2.80	188.87	16.84	16.83	2.00	11.22
	2.80-3.20	194.53	29.97	29.57	0.29	6.49
50-90	0.80-1.20	3.84	–	–	–	1.96
	1.20-1.60	19.04	–	–	–	4.36
	1.60-2.00	21.07	–	–	–	4.59
	2.00-2.40	30.56	–	–	–	5.53
	2.40-2.80	13.54	4.57	4.57	1.86	2.96
	2.80-3.20	1.08	6.81	6.62	0.03	0.16
			Tritons			
0-10	2.40-2.80	593.14	46.64	46.59	0.38	12.72
	2.80-3.20	671.86	83.30	82.47	0.11	8.07
10-30	2.40-2.80	259.51	21.81	21.80	1.20	11.90
	2.80-3.20	254.34	38.24	37.84	0.22	6.65
30-50	2.40-2.80	295.57	20.18	20.17	2.66	14.65
	2.80-3.20	244.81	31.80	31.31	0.33	7.70
50-90	2.00-2.40	46.25	–	–	–	6.80
	2.40-2.80	27.31	5.79	5.79	4.42	4.72
	2.80-3.20	29.27	8.64	8.47	0.69	3.39

4.4.2 (Anti)^{4}He candidates selection and PID

In order to select the (anti)^{4}He candidates, a $3\,\sigma$ cut around the (anti)^{4}He line is done in the TPC, then the m^2/z^2 is calculated with the TOF information. The m^2/z^2 distribution versus transverse momentum for the 0-10 % centrality interval is shown in figure 4.14 on the left for $^4\overline{\text{He}}$ and on the right for ^{4}He. The m^2/z^2 of the (anti)^{4}He is $3.475\,\text{GeV}^2/c^4$. ^{4}He and ^{3}He ($m(^3\text{He})^2/z^2 = 2.0\,\text{GeV}^2/c^4$) are clearly separated in the TOF mass. There is some background coming from TOF mismatches visible over the m^2 range. But it is much less than for the (anti)tritons. Comparing figures 4.14(a) and 4.14(b) on the right plot a significant contribution from knocked-out ^{4}He at low p_T is visible, coming from the beam pipe or the detector material, similar as it was for the tritons. For this reason the ^{4}He yield is only extracted for p_T/z larger than $1.5\,\text{GeV}/c$. In these plots one can actually hardly see any (anti)^{4}He, except for those ones coming from the material.

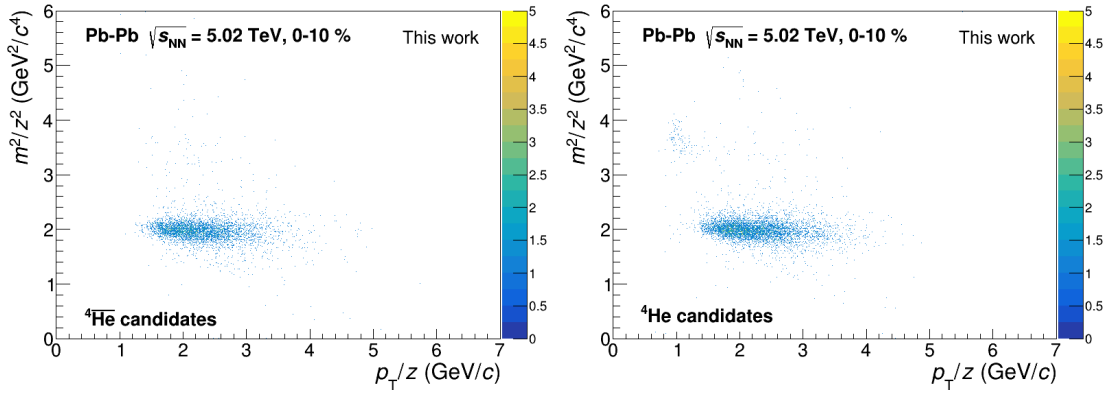

(a) $^4\overline{\text{He}}$. (b) ^{4}He.

Figure 4.14: m^2/z^2 distribution of the TOF detector versus the transverse momentum in the 0-10 % centrality interval for $^4\overline{\text{He}}$ on the left and ^{4}He on the right ($m^2_{^4\text{He}}/z^2 = 3.475\,\text{GeV}^2/c^4$). A $\mid n\sigma_{\text{TPC}}(^4\text{He}) \mid < 3$ selection around the (anti)^{4}He band in the TPC has been done before. Some background is visible over the m^2 range. In comparison to the $^4\overline{\text{He}}$ on the left side, on the right side there is a significant contribution visible at low p_T/z from knocked-out ^{4}He coming from the beam pipe or the detector material. However, the main contribution visible is the (anti)^{3}He at $2\,\text{GeV}^2/c^4$, well separated from the (anti)^{4}He in the TOF mass.

In figure 4.15 the DCA_xy distribution versus p_T/z is shown for ^{4}He. The broad distribution at low p_T/z is clearly visible and indicates once more the contribution from spallation processes.

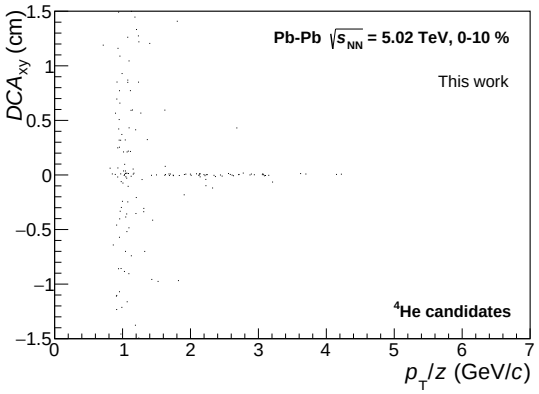

Figure 4.15: DCA_{xy} distribution versus p_{T}/z for ^{4}He in the 0-10 % centrality interval. The broad distribution at low p_{T}/z indicates the large contribution from material knock-out (spallation).

The (anti)^{4}He analysis is done in p_{T} bins of 1.0 GeV/c from 2.0 to 6.0 GeV/c for $^4\overline{\mathrm{He}}$ and from 3.0 to 6.0 GeV/c for ^{4}He. This corresponds to 0.5 GeV/c bins in p_{T}/z from 1.0 to 3.0 GeV/c and 1.5 to 3.0 GeV/c for $^4\overline{\mathrm{He}}$ and ^{4}He, respectively.

From the plots in figure 4.14 slices in p_{T}/z are projected on the m^2/z^2 axis.

To constrain the shape of the signal and to determine the range in which the signal is counted, it is first looked at the m^2/z^2 distribution of ^{4}He and $^4\overline{\mathrm{He}}$ together over the whole p_{T} range (2-6 GeV/c) including the ^{4}He coming from the material knock-out (see figure 4.16). The background (magenta) is determined by selecting all tracks in the TPC outside the $3\,\sigma$ ^{4}He band and in addition outside the $3\,\sigma$ deuteron band, as ^{4}He and deuteron have the same m^2/z^2. Then this background is scaled to the height of the ^{4}He histogram (green). The scaling factor is determined by dividing the integral of the ^{4}He histogram in a sideband (4.4-6.0 GeV$^2/c^4$) by the integral of the background histogram in this sideband. One can see the asymmetric shape of the ^{4}He signal around 3.475 GeV$^2/c^4$ with the TOF tail. Therefore the signal is counted between 3 and 4.2 GeV$^2/c^4$.

In figure 4.17 the four p_{T} bins for $^4\overline{\mathrm{He}}$ in the 0-10 % centrality interval are shown. In the first p_{T} bin no background is subtracted. In the other p_{T} bins the scaled background is subtracted.

In figure 4.18 the four p_{T} bins for ^{4}He in the 0-10 % centrality interval are shown. In the first p_{T} bin the material knock-out is visible. Therefore the yield is only extracted from the second bin onwards. From the second to the forth p_{T} bin the scaled background is subtracted.

In figure 4.17 as well as in figure 4.18 there still seems to be a contribution from ^{3}He in

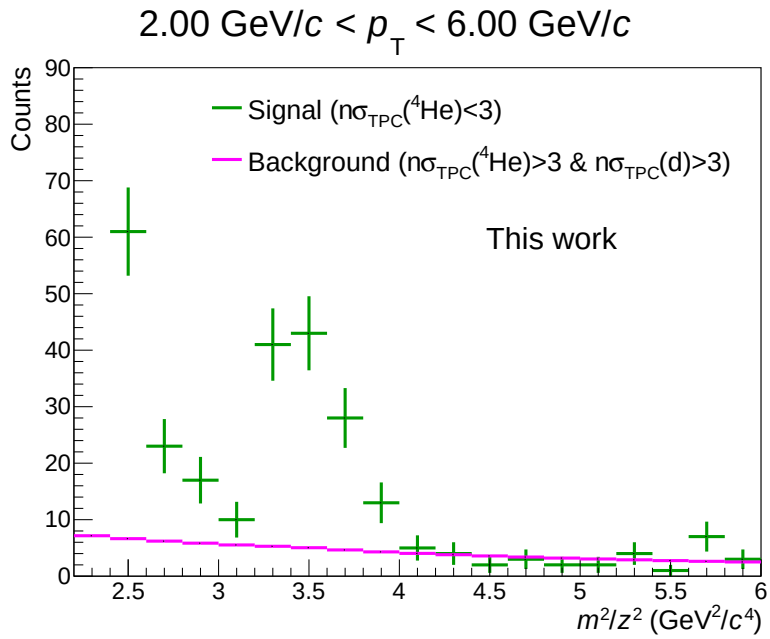

Figure 4.16: m^2/z^2 distribution of ^{4}He and $^4\overline{\text{He}}$ together ($|\ \text{n}\sigma_{\text{TPC}}(^4\text{He})\ | < 3$, green) and scaled background ($|\ \text{n}\sigma_{\text{TPC}}(^4\text{He})\ | > 3$ and $|\ \text{n}\sigma_{\text{TPC}}(\text{d})\ | > 3$, magenta) over the whole p_{T} range (2-6 GeV/c) in the 0-10 % centrality interval.

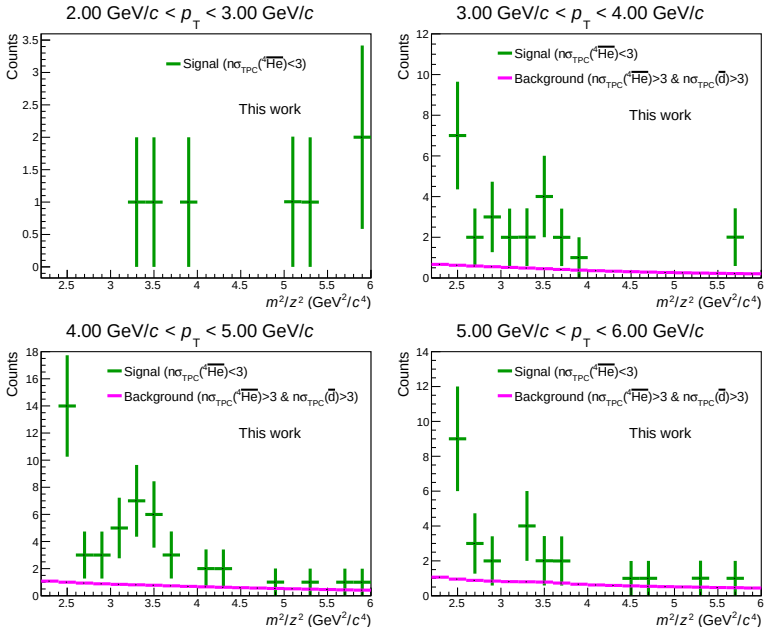

Figure 4.17: m^2/z^2 distribution of $^4\overline{\text{He}}$ ($|\ \text{n}\sigma_{\text{TPC}}(^4\overline{\text{He}})\ | < 3$, green) and scaled background ($|\ \text{n}\sigma_{\text{TPC}}(^4\overline{\text{He}})\ | > 3$ and $|\ \text{n}\sigma_{\text{TPC}}(\overline{\text{d}})\ | > 3$, magenta) for the different p_{T} bins in the 0-10 % centrality interval.

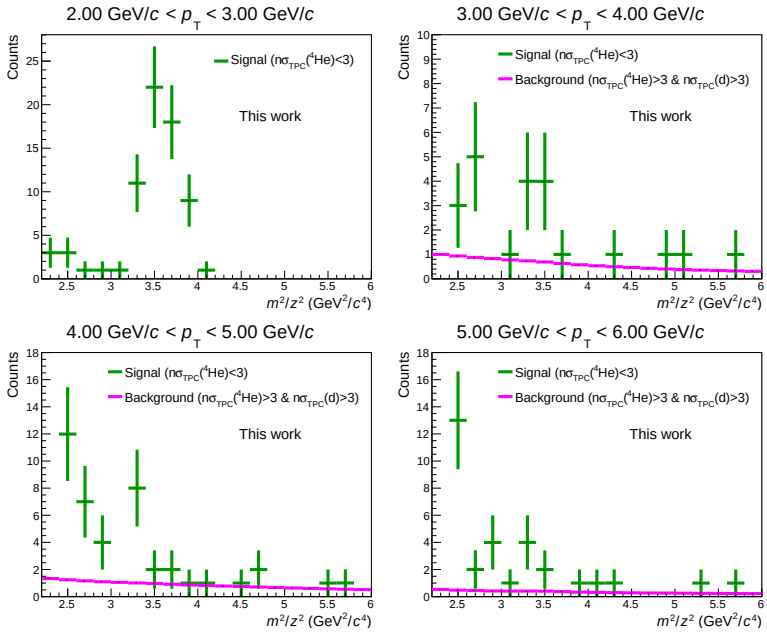

Figure 4.18: m^2/z^2 distribution of ^{4}He ($|\ \mathrm{n}\sigma_{\mathrm{TPC}}(^4\mathrm{He})\ | < 3$, green) and scaled background ($|\ \mathrm{n}\sigma_{\mathrm{TPC}}(^4\mathrm{He})\ | > 3$ and $|\ \mathrm{n}\sigma_{\mathrm{TPC}}(\mathrm{d})\ | > 3$, magenta) for the different p_{T} bins in the 0-10 % centrality interval. In the first p_{T} bin the contribution from material knock-out is visible.

the p_{T} bins from 3 to 6 GeV/c. As it was not possible to fit this contribution reasonably in the single p_{T} bins it was fitted in one p_{T} bin from 3 to 6 GeV/c for $^4\overline{\mathrm{He}}$ as well as for ^{4}He after subtracting the scaled background. As the m^2/z^2 signal of the TOF detector is usually well described by a Gaussian function with exponential tail at higher m^2/z^2, an exponential is chosen to describe the ^{3}He contribution. The fit is performed in two different fit ranges between 2.2 and 3.2 GeV$^2/c^4$ and between 2.4 and 3.2 GeV$^2/c^4$ (see figure 4.19). The inlay shows the same distribution with a logarithmic y-scale for a better visibility of the fits.

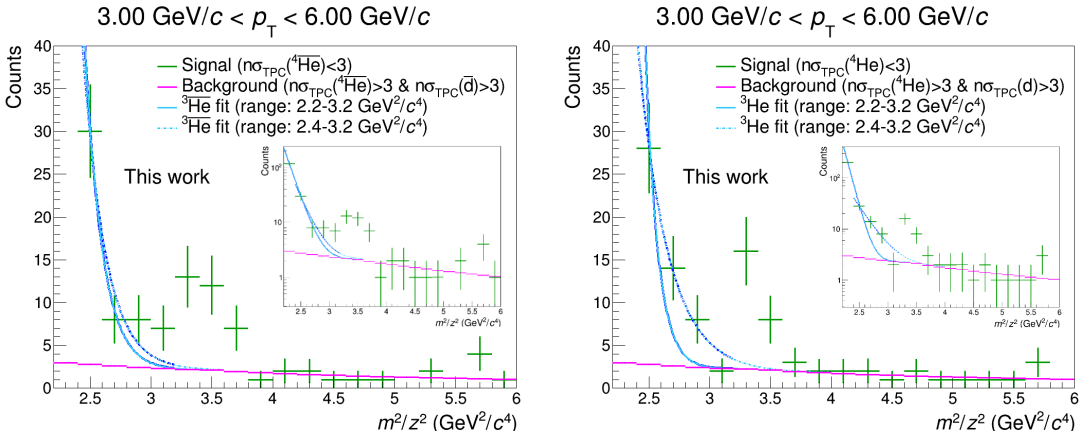

(a) Anti^{4}He. (b) ^{4}He.

Figure 4.19: m^2/z^2 distribution of (anti)^{4}He (green) and scaled background (magenta) between 3 and 6 GeV/c. In blue two exponential fit are shown to determine the (anti)^{3}He contribution. The inlay shows the same distribution with a logarithmic y-scale for a better visibility of the fits.

The fraction of entries under these fits to the entries in the (anti)^{4}He histogram between 3 and 4.2 GeV$^2/c^4$ is determined. The average between these two values is used as (anti)^{3}He contribution c. In the case of $^3\overline{\mathrm{He}}$ the difference between the two fits is quite small, while in the case of ^{3}He it is larger. The values are stated in table 4.9. As systematic uncertainty for the (anti)^{3}He contribution 25 % of the difference between the two fits is taken.

For both, ^{4}He and $^4\overline{\mathrm{He}}$, the entries are counted in a m^2/z^2 region between 3 and 4.2 GeV$^2/c^4$ in each p_{T} bin. From the p_{T} bins between 3 and 6 GeV/c the scaled background and then the constant fraction of the (anti)^{3}He contribution are subtracted. Because of the very small statistics of counts below ten of the (anti)^{4}He, the statistical uncertainties have been enlarged taking the Poisson distribution into account, following the suggestion by the Statistics Group of the CDF experiment [13, 62]. In-

Table 4.9: (Anti)^{3}He contribution to the (anti)^{4}He signal for the two fits as well as the average value with its systematic uncertainty.

Fit range (GeV$^2/c^4$)	$^3\overline{\text{He}}$ contribution	^{3}He contribution
2.2-3.2	1.86 %	0.48 %
2.4-3.2	4.24 %	17.15 %
Average	3.05 %	8.82 %
Systematic uncertainty	0.6 %	4.2 %

stead of $\sqrt{(S+B+f*B')(1-c)}$ the statistical uncertainty was determined as $\pm 0.5 + \sqrt{((S+B+f*B')(1-c))+0.25}$ for the upper (+) and lower (-) uncertainty, respectively. $S+B$ is the (anti)^{4}He histogram, B' is the scaled background, f is the scaling factor and c is the constant fraction of the (anti)^{3}He contribution (3.05 % for $^4\overline{\text{He}}$ and 8.82 % for ^{4}He). The raw signal, upper statistical uncertainty, signal-over-background ratio and significance for the different p_{T} bins for (anti)^{4}He in the 0-10 % centrality interval are stated in table 4.10.

Table 4.10: Signal, upper statistical uncertainty, signal-over-background ratio and significance for the different p_{T} bins for (anti)^{4}He in the 0-10 % centrality interval.

p_{T} (GeV/c)	S	$0.5+\sqrt{((S+B+f*B')(1-c))+0.25}$	S/B	Signif.
		$^4\overline{\textbf{He}}$		
2.00-3.00	3	2.3	–	1.30
3.00-4.00	8.13	3.80	2.83	2.14
4.00-5.00	17.94	5.25	3.55	3.42
5.00-6.00	3.50	3.33	0.78	1.05
		^{4}**He**		
3.00-4.00	5.52	3.56	1.23	1.55
4.00-5.00	7.63	4.11	1.20	1.86
5.00-6.00	6.17	3.41	2.18	1.81

The raw spectra of ^{4}He and $^4\overline{\text{He}}$ with statistical uncertainties are shown in figure 4.20.

4.5 Acceptance and Efficiency correction

Not all particles produced are measured in the detectors. On the one hand the active area of the detector does not cover the whole phase space. The acceptance is optimized to cover the midrapidity region, but also there support structure or edges between the chambers lead to not sensitive regions. On the other hand the detector is not completely efficient in measuring particle tracks, a particle could just not produce a signal in some detector layers or the signal could be distorted by noise, so that the information is not

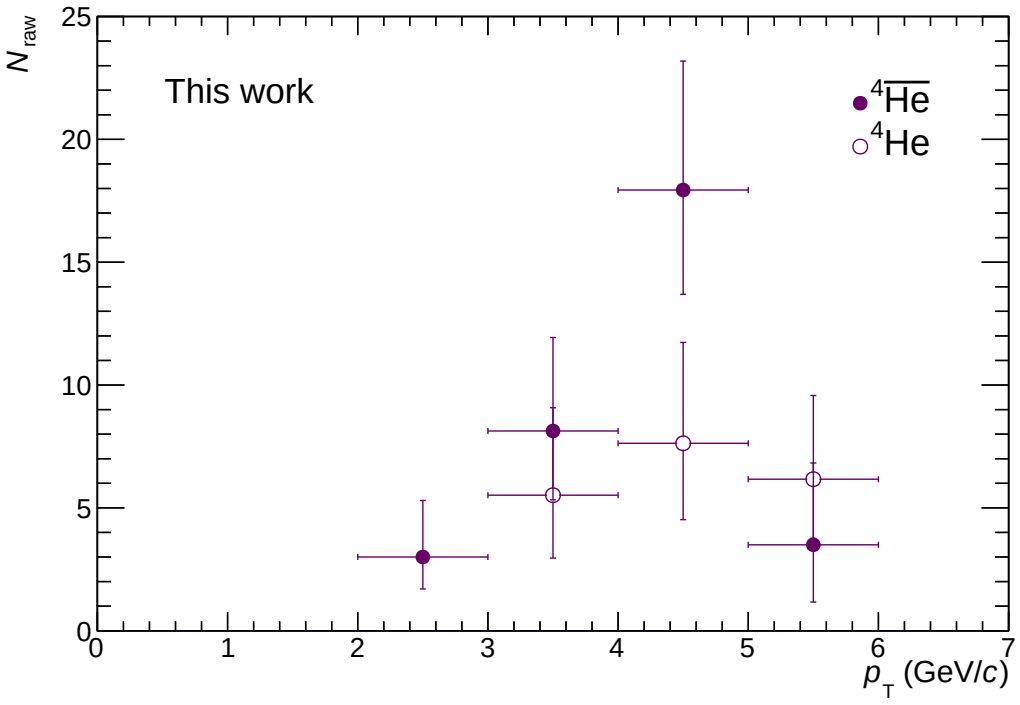

Figure 4.20: Raw spectra of ^{4}He and $^4\overline{\text{He}}$ with statistical uncertainties shown as vertical error bars. The horizontal error bars represent the bin width.

exact. In addition some parts of the detector could be switched off because of problems (e.g. stability, etc.) in some runs. So a combined acceptance and efficiency correction (Acceptance x Efficiency, Acc x Eff) has to be taken into account. This correction is determined with the Monte Carlo samples LHC20g7[a,b,c] that were introduced in section 4.2 and are anchored to the data runs that are analyzed. In the MC simulation the geometry of the detector and the data taking conditions are reproduced. The Acceptance x Efficiency is calculated as follows:

$$Acc \text{ x } Eff = \frac{N_{\text{rec}}}{N_{\text{gen}}} \tag{4.5}$$

N_{gen} is the number of generated particles of a certain species with flat p_{T} distribution between 0 and 10 GeV/c in an azimuthal region of $2\,\pi$ and in a rapidity window of $\mid y \mid < 0.5$. N_{rec} is the number of reconstructed particles of the certain species after passing the detector simulation satisfying the same track cuts also applied to the real data presented in table 4.5. Also the cut around the dE/dx band in the TPC has to be the same in MC and data ($2\,\sigma$ for (anti)triton and $3\,\sigma$ for (anti)^{4}He). Therefore the

Bethe-Bloch parametrization was checked for the MC data sample. As can be seen in figure 4.21(a) the Bethe-Bloch parametrization, that was determined for the data sample, does not match the MC sample very well. Thus, a new parametrization especially for the MC sample was determined, the Bethe-Bloch lines can be seen in figure 4.21(b).

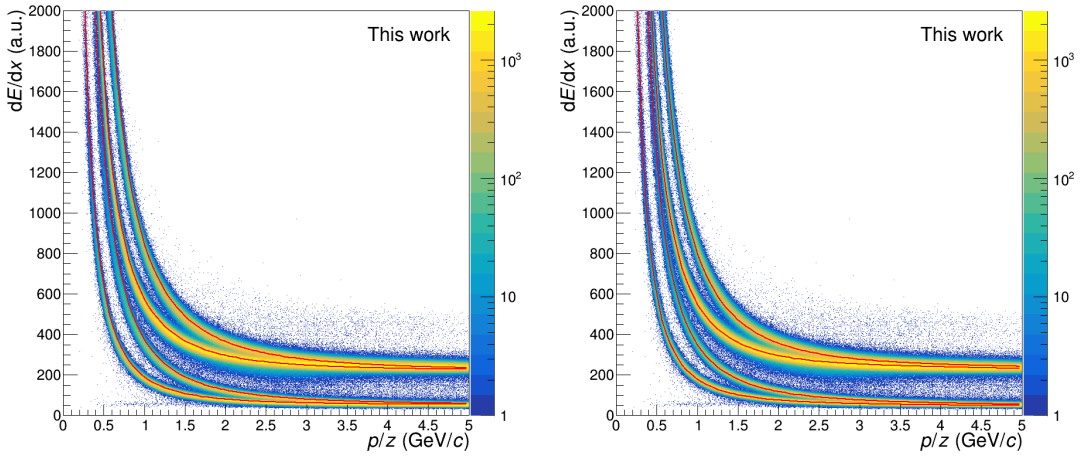

(a) 0-90 % centrality interval, Bethe-Bloch lines of data sample.

(b) 0-90 % centrality interval, parametrization determined for MC sample.

Figure 4.21: Specific energy loss in the TPC versus rigidity (from left to right) for deuterons, tritons, ^{3}He and ^{4}He in the MC sample anchored to the LHC18q+r data sample. The red lines represent the Bethe-Bloch curves. On the left plot the same curves as used for the data sample are drawn, on the right plot the parameters were determined to match the MC sample.

The parameters of the ALEPH parametrization (see equation 4.2) for the MC sample are listed in table 4.11.

Table 4.11: Bethe-Bloch parameters of the ALEPH parametrization for nuclei with $z=1$ and $z=2$ in the LHC20g7[a,b,c] MC samples.

Parameters	Nuclei with $z=1$ ((anti)t)	Nuclei with $z=2$ ((anti)^{4}He)
P_1	0.995866	0.900232
P_2	37.409	50.3113
P_3	0.00245485	$4.42379\ 10^{-5}$
P_4	2.28623	2.163
P_5	8.09021	9.78186

In figure 4.22 the Acceptance x Efficiency is shown for tritons and antitritons in the four centrality intervals, in figure 4.23 for ^{4}He and $^4\overline{\text{He}}$ in the 0-10 % centrality interval.

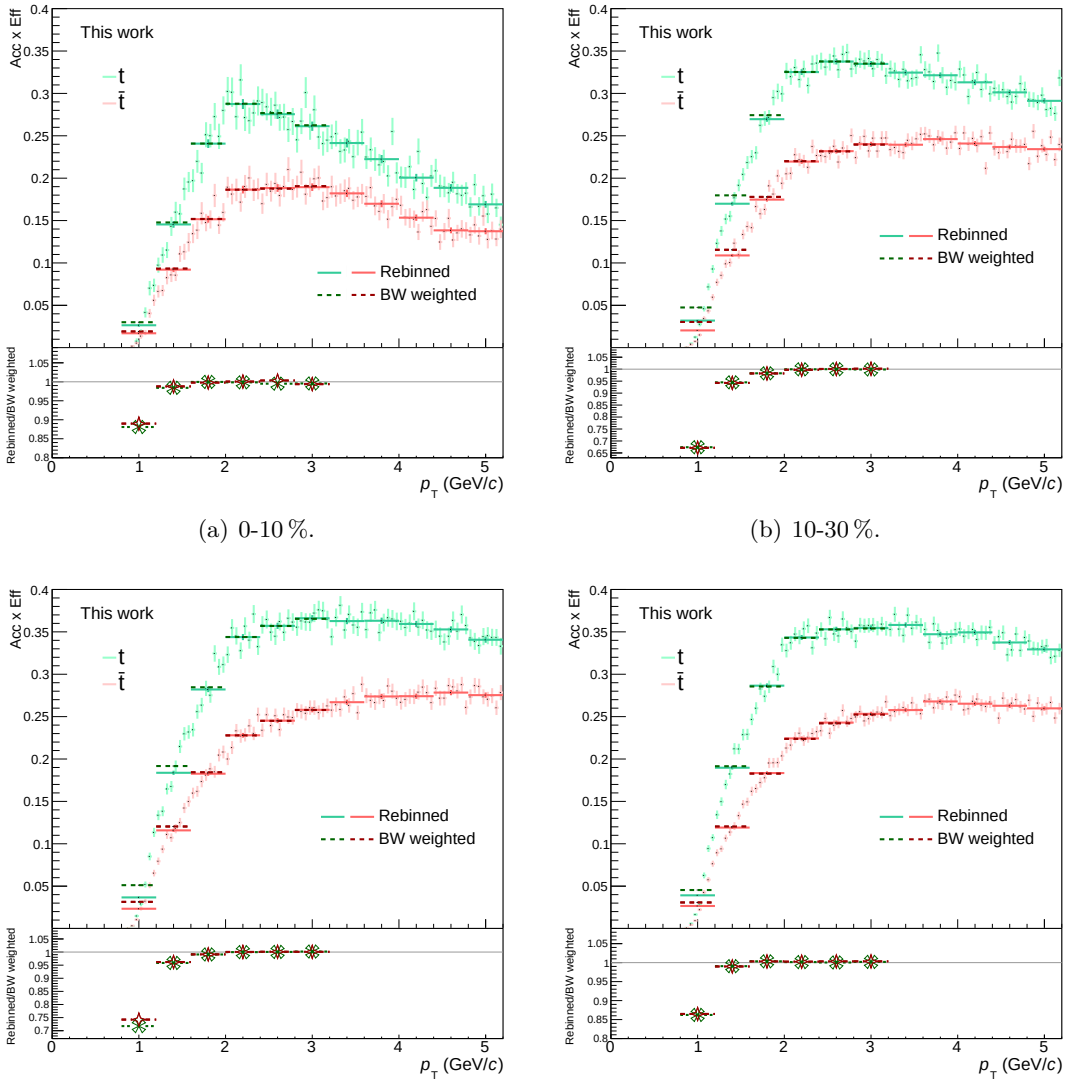

(a) 0-10 %. (b) 10-30 %.

(c) 30-50 %. (d) 50-90 %.

Figure 4.22: Acceptance x Efficiency versus p_T for tritons (green markers) and antitritons (red markers) in the four centrality intervals. The Acc x Eff is rebinned in the bins of the analysis (solid lines) and weighted with a Blast-Wave shape (dashed lines). In the lower panel the ratio between the rebinned and the weighted Acc x Eff is shown.

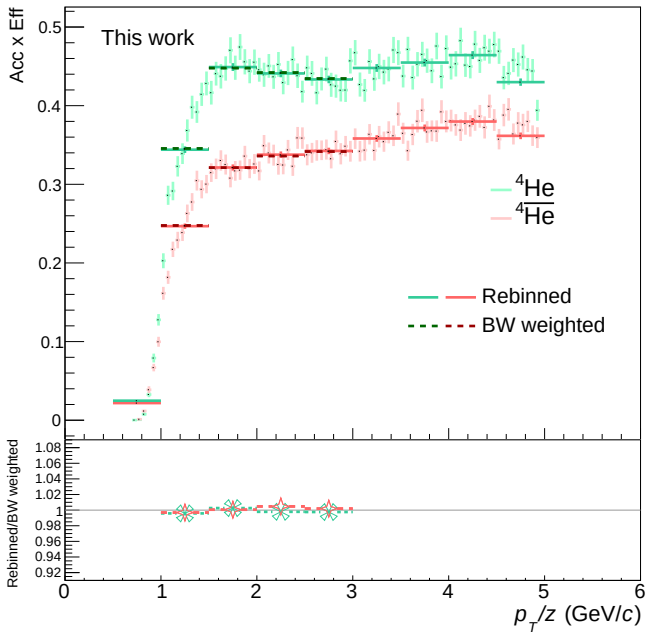

Figure 4.23: Acceptance x Efficiency versus p_{T}/z for ^{4}He (green markers) and anti^{4}He (red markers) in the 0-10 % centrality interval. The Acc x Eff is rebinned in the bins of the analysis (solid lines) and weighted with a Blast-Wave shape (dashed lines). In the lower panel the ratio between the rebinned and the weighted Acc x Eff is shown.

For the antiparticles (red markers) the Acceptance x Efficiency is lower than for the particles (green markers) because some of them are absorbed in the detector material.

The shape of the p_{T} spectra of light (anti)nuclei is not very well known, so in the MC samples they are injected with a flat p_{T} distribution, which means N_{gen} is flat. This is not physically correct. As at low p_{T} the Acceptance x Efficiency is rising very strongly (see figures 4.22 and 4.23), it was weighted with a Blast-Wave function, which is usually the shape of p_{T} spectra in Pb–Pb collisions. The dashed lines represent the Blast-Wave weighted Acc x Eff. For the solid lines the Acc x Eff was just rebinned to the bin size of the analysis. The lower panels show the ratio between the just rebinned and the weighted Acc x Eff.

One can see that at high p_{T} where the Acceptance x Efficiency is relatively flat no difference is observed with and without weighting. At low p_{T} of the (anti)triton Acc x Eff, however, especially in the first p_{T} bin from 0.8 to 1.2 GeV/c, the Acc x Eff is significantly higher if the Blast-Wave weighting of the Acceptance x Efficiency is performed. So the weighting is taken into account. For (anti)^{4}He nearly no difference is visible between

weighted and not-weighted Acc x Eff as the analysis starts at higher p_{T}.

4.6 Systematic uncertainties

A time consuming but important part of the analysis is the estimation of the systematic uncertainties. Systematic uncertainties are independent from the size of the available data set, they concern the analysis method. While the statistical uncertainties are indicated as error bars on the data points, the systematic uncertainties will be shown as boxes. There are several contributions of systematic uncertainties from the different analysis steps. They are listed below. The total systematic uncertainty is determined as the quadratic sum of the single contributions.

1. Uncertainty of the track selection.
2. Uncertainty of the signal extraction.
3. Uncertainty of the hadronic interaction with the detector material (difference of Acc x Eff in MC samples with increased and decreased hadronic inelastic cross section).
4. Uncertainty of the material budget of the detector (difference of Acc x Eff in MC samples with increased and decreased material budget).
5. Uncertainty of the exact shape of the input spectrum of the generated (anti)nuclei in the MC samples (difference between the Acc x Eff weighted with a Blast-Wave function and without weighting).

As the statistical uncertainties of the (anti)t and (anti)^{4}He analyses are very large it is not always clear whether variations in the yield mirror a systematic change or are purely due to statistical fluctuations. Therefore for the systematic variations of the track selection and signal extraction (only for (anti)tritons) a criterion proposed by Roger Barlow [63] was applied. For every value of the yield resulting from a variation of a track cut or the signal extraction a value C was calculated. This was done for all p_{T} bins. The value C is defined as follows:

$$C(J,K) = \frac{J-K}{\sqrt{\mid \sigma_J^2 - \sigma_K^2 \mid}} \tag{4.6}$$

Here J is the nominal value with its statistical uncertainty σ_J and K is the variation with its statistical uncertainty σ_K. As for the most variations and p_{T} bins C was below

two, what means that the significance that this variation was a systematic one and not purely statistical is below $2\,\sigma$, the obtained systematic uncertainties for the cut variations and signal extraction were dropped and reasonable systematic uncertainties were assigned. The total systematic uncertainties and the single contributions for (anti)t and (anti)^{4}He are shown in table 4.12. In the following it will be explained in detail how these uncertainties were obtained. This will be done separately for (anti)t and (anti)^{4}He, as they were partly determined differently.

Table 4.12: Summary table of systematic uncertainties for (anti)tritons and (anti)^{4}He.

	ITS-TPC mat.	Signal extr.	Hadr. int.	Mat. bud.	BW weigh.	Total
$\bar{\mathrm{t}}$	5 %	6 %	6.8 %	2 %	(0-16.4) %	(10.5-19.5) %
t	5 %	6 %	2.3 %	2 %	0 %	8.4 %
$^4\overline{\mathrm{He}}$	5 %	(6-21.9) %	7 %	2 %	-	(10.7-23.6) %
^{4}He	5 %	(9.3-13.7) %	2.3 %	2 %	-	(11.0-14.9) %

4.6.1 Systematic uncertainty estimation for (anti)tritons

Track selection

To estimate the systematic uncertainties of the track selection, a variation of the track selection criteria was performed. These variations are shown in table 4.13. The analysis was done for every variation, while the other values were fixed at the default value.

Table 4.13: Variation of the track selection criteria for (anti)tritons.

Selection	Default	Variation
TPC clusters used for PID	>120	110, 130
$\chi^2_{\mathrm{TPC}}/n_{\mathrm{TPC\ clusters}}$	< 4	3, 5
TRD refit	On	Off
At least one hit on ITS layer	0 or 1	0 and 1
DCA_{xy}	Off	$< (0.0105 + (0.0350\ {p_{\mathrm{T}}}^{-1.1}))$ cm

In figure 4.24(a) the corrected yield is shown for the default track selection (dark blue markers) and for the different variations (colorful lines) versus p_{T} exemplarily for antitritons in the 30-50 % centrality interval. It can be observed that most of the variations are inside the statistical uncertainties of the default setting. In figure 4.24(b) the corresponding C value of the Barlow criterion for the different variations is shown. The C values hardly exceed $2\,\sigma$, this happens only for a few p_{T} bins. So, these variations seem to be due to statistical fluctuations. For this reason it was refrained from using the

cut variations to determine systematic uncertainties. The same can be observed for the other centrality intervals and for the tritons.

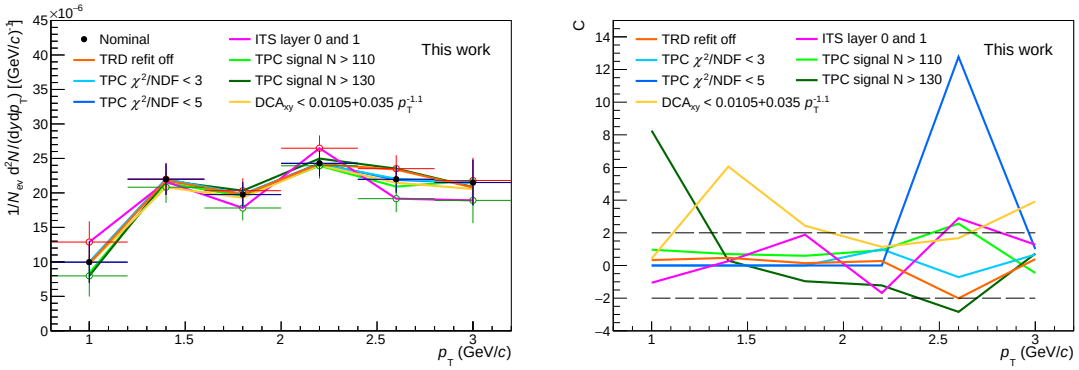

(a) Systematic variations of the track cuts. The red and green open circles indicate the uppermost and the lowermost variation with statistical uncertainties, respectively.

(b) C value of the Barlow criterion for the track cut variations.

Figure 4.24: Systematic variations of the track cuts (left) and C value of the Barlow criterion (right) versus p_{T} for antitritons in the 30-50 % centrality interval.

Instead the systematic uncertainty of the ITS-TPC matching was employed. The recommendation of the ALICE Data Preparation Group (DPG) therefor is 5 % [64].

Signal extraction

To estimate the systematic uncertainty of the signal extraction the binning of the m^2/z^2 histogram was increased and decreased. Furthermore, the region in which the entries are counted was decreased to $2\,\sigma$ and $1\,\sigma$ and then corrected by the corresponding factor of 0.9545 and 0.6827, respectively. In addition, the background was scaled up and down by 10 %. Also for the systematic variations of the signal extraction the Barlow criterion was applied. In figure 4.25(a) the corrected yield is shown for the default signal extraction (dark blue markers) and for the different variations (colorful lines) versus p_{T} exemplarily for antitritons in the 30-50 % centrality interval. Figure 4.25(b) shows the corresponding C value of the Barlow criterion for the different variations. As can be seen also for the signal extraction the value only exceeds $2\,\sigma$ in a few p_{T} bins. So, these variations seem to be dominated by statistical fluctuations and are not used to determine systematic uncertainties. Instead the systematic uncertainty of the signal extraction was p_{T}-independently set to 6 % for antitritons and tritons which is a value for this quantity that is extracted in similar analyses with significantly larger statistics and smaller

background and therefore smaller fluctuations [65].

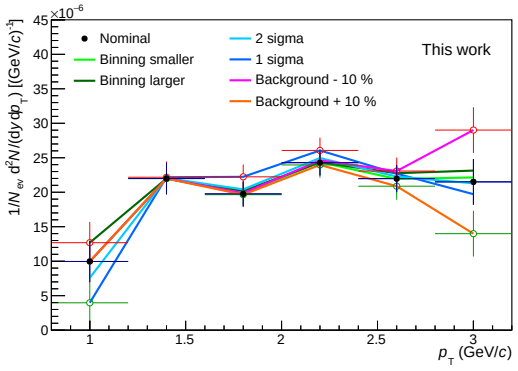

(a) Systematic variations of the signal extraction. The red and green open circles indicate the uppermost and the lowermost variation with statistical uncertainties, respectively.

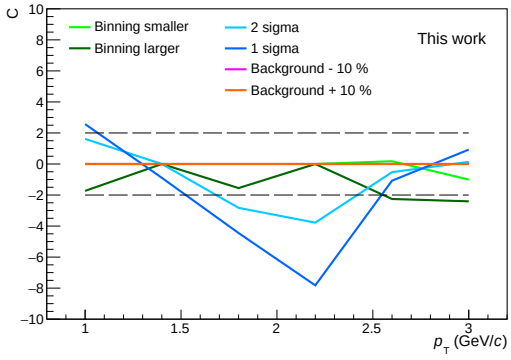

(b) C Value of the Barlow criterion for the variation of the signal extraction.

Figure 4.25: Systematic variations of the signal extraction (left) and C value of the Barlow criterion (right) versus p_T for antitritons in the 30-50 % centrality interval.

Hadronic interaction

The hadronic inelastic cross section of nuclei with the ALICE detector material is only known to a limited precision. However, there has been a preliminary ALICE measurement of the hadronic inelastic cross section of $^3\overline{\text{He}}$ nuclei [65]. As $^3\overline{\text{He}}$ and $\bar{\text{t}}$ have similar mass and size, it is assumed that the uncertainty of the hadronic inelastic cross section is the same. The measurement of the $^3\overline{\text{He}}$ inelastic cross section was compared to the default cross section used in the MC samples LHC20g7[a,b,c] from which the Acc x Eff to correct the nuclei spectra are obtained. A deviation of 17 % between the measured $^3\overline{\text{He}}$ cross section and the default cross section in the MC samples was determined [66]. To translate the uncertainty on the cross section to an uncertainty on the p_T spectra a special MC production LHC20i3[a,b,c][1,2,3] (see section 4.2) with increased and decreased hadronic inelastic cross section and injected $^3\overline{\text{He}}$ nuclei was used. In these MC samples the Acc x Eff for $^3\overline{\text{He}}$ was calculated applying the track cuts of the (anti)triton analysis (see table 4.5). Figure 4.26 shows the Acc x Eff versus p_T/z for $^3\overline{\text{He}}$ in the 0-10 % centrality interval in the MC samples with increased (yellow), decreased (red) and default (orange) hadronic inelastic cross section. As the hadronic inelastic cross section is independent from the collision centrality, this plot is only shown for one centrality

interval. As it should be, the Acc x Eff is lower for the increased cross section, as more nuclei react with the material and cannot be measured anymore, and higher for the decreased cross section. In the lower panel twice the variation of the Acc x Eff with varied (i.e. increased or decreased) from the Acc x Eff with default cross section is shown. The factor two meets the fact that the cross section in the MC samples is varied by 50 %.

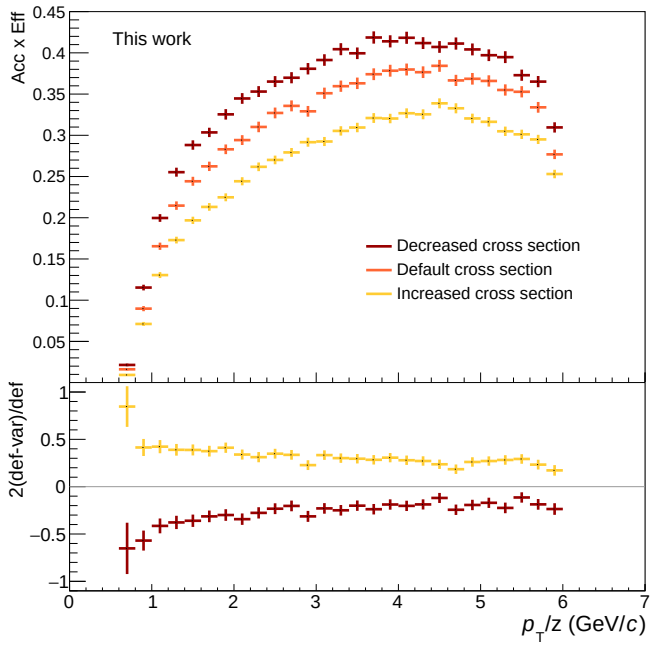

Figure 4.26: Acceptance x Efficiency versus p_T/z for $^3\overline{He}$ in the 0-10 % centrality interval determined from the MC samples with increased, decreased and default hadronic inelastic cross section. The lower panel shows two times the relative deviation of the Acc x Eff with varied cross section from the Acc x Eff with default cross section.

This variation is quite independent of the momentum and only varies a bit between 0.2 at higher p_T and 0.4 at lower p_T. The systematic uncertainty on the $^3\overline{He}$ and thus antitriton p_T spectra coming from the hadronic interaction is determined by multiplying the variation in the Acc x Eff with the 17 % deviation of the measured hadronic inelastic cross section mentioned above. As the antitriton spectra are measured at lower p_T, 0.4 is used for the variation on the Acc x Eff and thus the systematic uncertainty on the antitriton spectra is obtained to be $0.4 \cdot 0.17 = 6.8$ %.

Other analyses obtained a factor 3 smaller uncertainty on the hadronic interaction for particles with respect to antiparticles [66]. Therefore for tritons, one third of the determined 6.8 % for the antitritons, i.e. 2.3 %, is employed.

Material budget

The material budget of the ALICE detector setup is not exactly known and has an uncertainty of about 5 %. To consider the uncertainty of the material budget on the p_{T} spectra, two MCs with increased and decreased material budget (LHC17d5a and LHC17d5b) by respectively 4.5 %, were compared to a MC with the default material budget (LHC16h7c). These MCs are anchored to peripheral Pb–Pb collisions from the 2015 data set and produced with the GEANT 3 transport code (see section 4.2). The Acceptance x Efficiency was determined for tritons and antitritons in all three MC samples (see figure 4.27(a)). Here is clearly something wrong with the MC samples, as the Acc x Eff with increased and decreased material budget should lie below and above the default one, respectively. So, obviously something else and not only the material budget must have changed between the MC samples. However, at the time of the analysis no other and more recent MC sample with varied material budget and injected nuclei anchored to a Pb–Pb data set was available.

The ratio of the MC samples with the increased and decreased material budget over the MC sample with the default material budget was determined (see figure 4.27(b)). A constant was fitted to the ratio with the largest deviation from one (magenta markers) between a p_{T} of 2 and 9 GeV/c, which gave a 4 % deviation. Half of this value, so 2 %, was taken as systematic uncertainty of the material budget for both, antitritons and tritons. This value was also confirmed in other analyses [67].

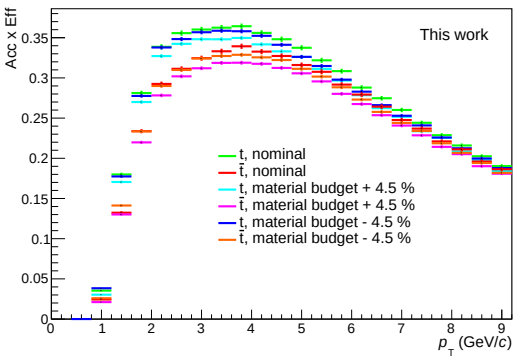

(a) Acceptance x Efficiency of antitritons and tritons for MCs with different material budget.

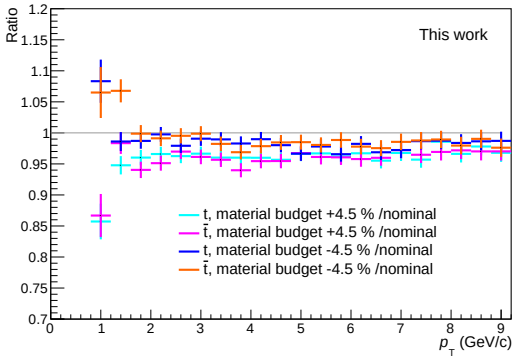

(b) Ratio of Acceptance x Efficiency for (anti)t for the MCs with different material budget over the MC with nominal material budget.

Figure 4.27: Comparison of MC samples with increased, decreased and nominal material budget for antitritons and tritons.

Weighting of Acceptance x Efficiency

The systematic uncertainty of the Acc x Eff weighting is estimated by taking half of the deviation from one in the ratio in figure 4.22 p_{T} bin by p_{T} bin for all four centrality intervals. As the difference only appears at low p_{T} and the triton spectra start from higher p_{T} the systematic uncertainty only applies for antitritons, it is stated in table 4.14.

Table 4.14: Systematic uncertainties from the Blast-Wave weighting for the different centralities and p_{T} bins.

Antitritons		
Centrality (%)	p_{T} (GeV/c)	Syst. uncertainty of BW weighting
0-10	0.8-1.2	5.5 %
	1.2-1.6	0.6%
10-30	0.8-1.2	16.4%
	1.2-1.6	2.9%
	1.6-2.0	0.9%
30-50	0.8-1.2	12.9%
	1.2-1.6	1.9%
	1.6-2.0	0.4%
50-90	0.8-1.2	6.8%
	1.2-1.6	0.5%

4.6.2 Systematic uncertainty estimation for (anti)^{4}He

Track selection

The variation of the track selection criteria is in principle the same as for the (anti)tritons (see table 4.13), with the only exception that the cut on the TPC cluster used for PID was not applied in the (anti)^{4}He analysis and thus also not varied. Instead the minimum number of TPC clusters for the tracking was varied.

Table 4.15: Variation of the track selection criteria fot (anti)^{4}He.

Selection	Default	Variation
Number of TPC clusters	> 70	60, 80
$\chi^2_{\mathrm{TPC}}/n_{\mathrm{TPC\ clusters}}$	< 4	3, 5
TRD refit	On	Off
At least one hit on ITS layer	0 or 1	0 and 1
DCA_{xy}	Off	$< (0.0105 + (0.0350\ {p_{\mathrm{T}}}^{-1.1}))$ cm

Due to the very low statistics of the (anti)^{4}He, the variation of the track selection

criteria was performed in a single p_{T} bin from 2 to 6 GeV/c and 3 to 6 GeVc for $^4\overline{\mathrm{He}}$ and ^{4}He, respectively (see figures 4.28(a) and 4.28(c)). The dark blue marker is the value with the default cuts with its statistical uncertainty. The colorful lines are the variations. The C value of the Barlow criterion is calculated and shown in figures 4.28(b) and 4.28(d). For nearly all variations it is below two. So, also for (anti)^{4}He, it was refrained from determining a systematic uncertainty from the track cut variation and the systematic uncertainty of the ITS-TPC matching of 5 % recommended by the ALICE DPG [64] was applied instead.

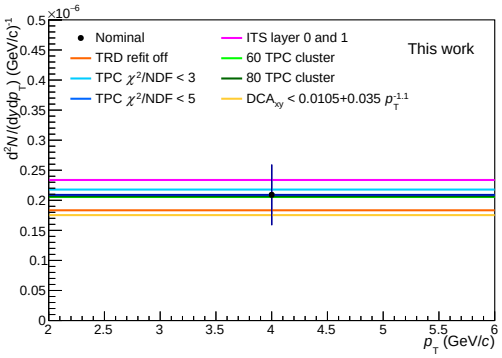

(a) Cut variations $^4\overline{\mathrm{He}}$, 2-6 GeV/c.

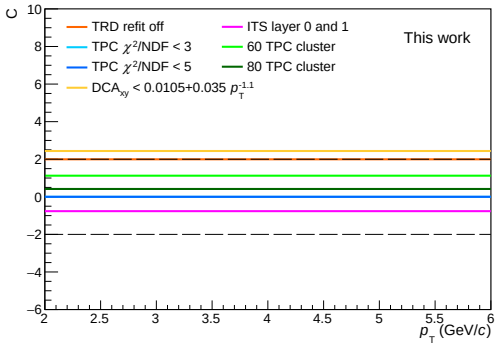

(b) C value $^4\overline{\mathrm{He}}$, 2-6 GeV/c.

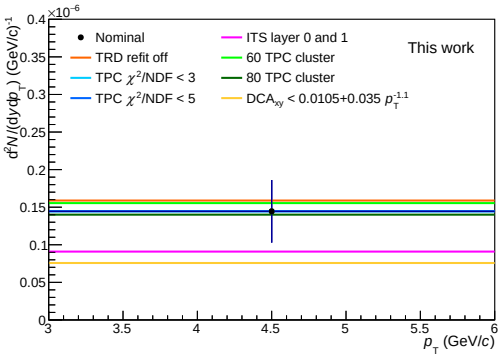

(c) Cut variations ^{4}He, 3-6 GeV/c.

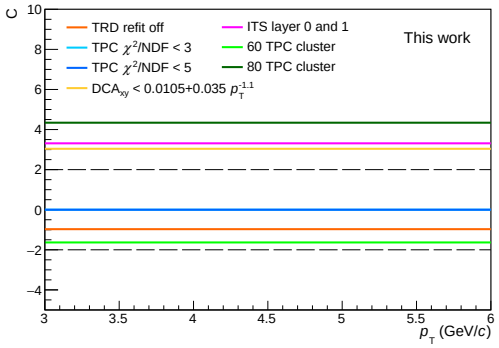

(d) C value ^{4}He, 3-6 GeV/c.

Figure 4.28: Variation of the track cuts for (anti)^{4}He in one p_{T} bin (left) and C value of the Barlow criterion (right).

Signal extraction

As systematic uncertainty of the signal extraction 6 % was taken for ^{4}He as well as $^4\overline{\mathrm{He}}$, as was done for the (anti)tritons.

In addition as estimation of the systematic uncertainty of the (anti)^{3}He contribution to

the (anti)^{4}He yield half of the difference between the two fits to the (anti)^{3}He contribution was taken, as was already stated in table 4.9. This results in a systematic uncertainty of 0.6 % for $^4\overline{\text{He}}$ and 4.2 % for ^{4}He in the p_{T} bins between 3 and 6 GeV/c.

Furthermore, the scaling factor of the scaled background was varied up and down by 30 % (see figure 4.29). In the first p_{T} bin of the $^4\overline{\text{He}}$ between 2 and 3 GeV/c no background is subtracted, so in this bin there is no systematic uncertainty coming from this contribution. The resulting systematic uncertainties for the other p_{T} bins are stated in table 4.16 for $^4\overline{\text{He}}$ and ^{4}He.

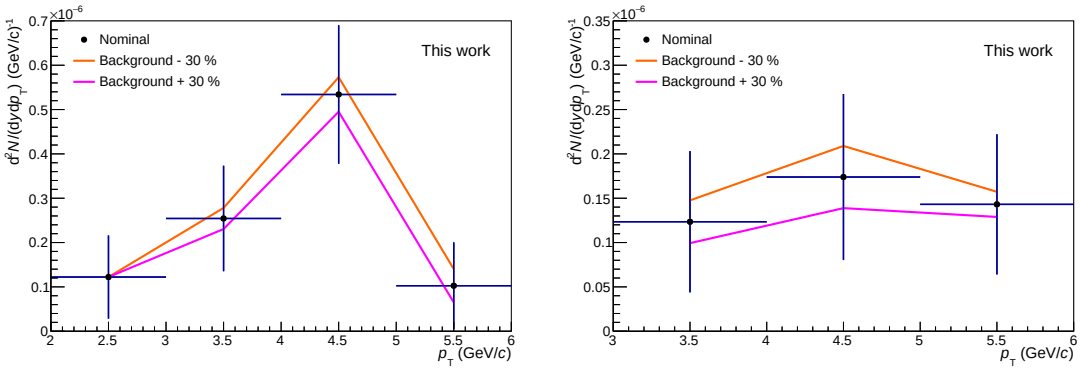

(a) $^4\overline{\text{He}}$. (b) ^{4}He.

Figure 4.29: Variation of the signal extraction (scaling factor of scaled background) for (anti)^{4}He.

Table 4.16: Systematic uncertainties from the variation of the scaling factor of the scaled background for (anti)^{4}He.

p_{T} (GeV/c)	3-4	4-5	5-6
$^4\overline{\text{He}}$	5.4%	4.2%	21.1%
^{4}He	11.3%	11.6%	5.7%

The three different contributions to the systematic uncertainty coming from the signal extraction are added quadratically.

Hadronic interaction

As there is no ALICE measurement of the hadronic inelastic cross section for $^4\overline{\text{He}}$ yet, the uncertainty on the $^4\overline{\text{He}}$ p_{T} spectrum due to the hadronic interaction is inherited from the (anti)^{4}He measurement at $\sqrt{s_{\text{NN}}} = 2.76$ TeV [19] to be 7 %. For ^{4}He one third of this value, i.e. 2.3 %, is taken, as it was done for the tritons.

Material budget

Like for the (anti)tritons the MC samples with the increased and decreased material budget (LHC17d5a and LHC17d5b) were compared with the one with default material budget (LHC16h7c). In figure 4.30(a) the Acceptance x Efficiency is shown for ^{4}He and $^4\overline{\text{He}}$ in these three MC samples. In figure 4.30(b) the ratio to the MC with nominal material budget is shown. To estimate a systematic uncertainty a constant was fitted to the histogram with the largest deviation from one (magenta markers) between a p_{T}/z of 1 and 5 GeV/c. This results in 4 % deviation and 2 % systematic uncertainty for ^{4}He and $^4\overline{\text{He}}$, taking half of the determined value. This is the same uncertainty that was determined for the (anti)tritons.

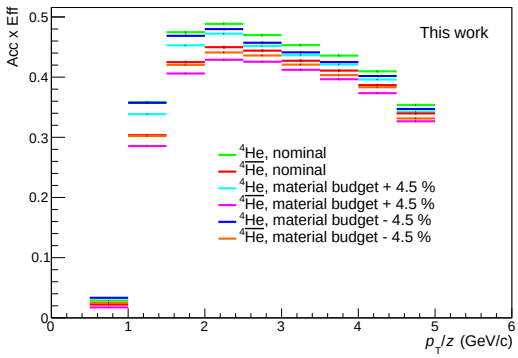

(a) Acceptance x Efficiency of $^4\overline{\text{He}}$ and ^{4}He for MCs with different material budget.

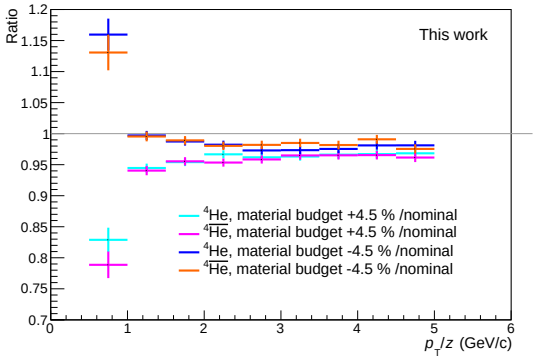

(b) Ratio of Acceptance x Efficiency of (anti)^{4}He for the MCs with different material budget over the MC with nominal material budget.

Figure 4.30: Comparison of MC samples with increased, decreased and default material budget for $^4\overline{\text{He}}$ and ^{4}He.

Weighting of Acceptance x Efficiency

For (anti)^{4}He there was no difference observed in the Acceptance x Efficiency with and without weighting (see figure 4.23). So, there is no contribution to the systematic uncertainties for (anti)^{4}He coming from the Blast-Wave weighting.

4.7 Coalescence parameters

From the p_{T} spectra of (anti)tritons (see figure 5.1(a)) and (anti)^{4}He (see figure 5.1(b)) and the proton spectra at the same center-of-mass energy the coalescence parameters B_3

and B_4 can be calculated. The coalescence parameter B_A is the main parameter of the coalescence model and is related to the probability to form a nucleus via coalescence. A is the mass number of the nucleus. The coalescence parameter is calculated from the p_{T} spectra as follows:

$$B_A = \frac{\frac{1}{2\pi p_{\mathrm{T}}^A} \frac{\mathrm{d}^2 N_A}{\mathrm{d}y \mathrm{d}p_{\mathrm{T}}^A}}{\left(\frac{1}{2\pi p_{\mathrm{T}}^{\mathrm{p}}} \frac{\mathrm{d}^2 N_{\mathrm{p}}}{\mathrm{d}y \mathrm{d}p_{\mathrm{T}}^{\mathrm{p}}}\right)^A} \qquad \text{with } p_{\mathrm{p}} = \frac{p_A}{A} \tag{4.7}$$

The invariant yield of a nucleus with mass number A is divided by the invariant proton yield to the power of A. The proton yield is measured at a momentum of $1/A$ of the momentum of the nucleus. In case of $A = 3$ the $\frac{\mathrm{d}^2 N_A}{\mathrm{d}y \mathrm{d}p_{\mathrm{T}}^A}$ in the numerator is the (anti)triton yield, in case of $A = 4$ it is the (anti)^{4}He yield. The proton yield, used in the denominator, is published [68]. As the proton yield is measured in finer centrality intervals the centrality intervals were averaged to match the (anti)triton and (anti)^{4}He spectra. Therefor the statistical uncertainties are quadratically, the systematic uncertainties linearly added. In addition, the proton yield was divided by two as it is measured as the combined proton and antiproton spectrum. The proton yield for the B_3 is measured at $\frac{1}{3}$ of the (anti)triton momentum, whereas for the B_4 it is measured at $\frac{1}{4}$ of the (anti)^{4}He momentum. This suggests that a nucleus with mass number A and a momentum p_A is build of A nucleons (protons or neutrons) with a momentum of p_A/A each. As ALICE cannot measure neutrons, only the proton spectra are used to calculate the B_A and it is assumed that proton and neutron spectra are the same. The binning in p_{T} is much finer for the proton spectra than for (anti)triton and (anti)^{4}He. Because of that the proton spectra were rebinned to match the (anti)triton or (anti)^{4}He spectra, respectively. As the bin boundaries don't match, a fit was needed to weight the single proton bins. For this purpose a Blast-Wave function was used.

For the B_3, the proton spectra were fitted from 0.3 to 1.2 GeV/c. In figure 4.31(a) the averaged spectra with the fits with $3\,\sigma$ confidence interval are shown. The proton spectra start at 0.3 GeV/c, however, for the B_3 the spectrum is needed from 0.267 GeV/c. Therefore the first point of each centrality interval was added at the fit value, the statistical uncertainty was set to zero and the systematic uncertainty to the one of the neighbouring point and the $3\,\sigma$ confidence interval of the fit quadratically added.

The spectra were rebinned using the fit as weight, adding the statistical uncertainties of the single bins quadratically, the systematic ones linearly. This was done for all four centrality intervals.

For the B_4, the proton spectrum in the 0-10 % centrality interval was fitted from 0.5

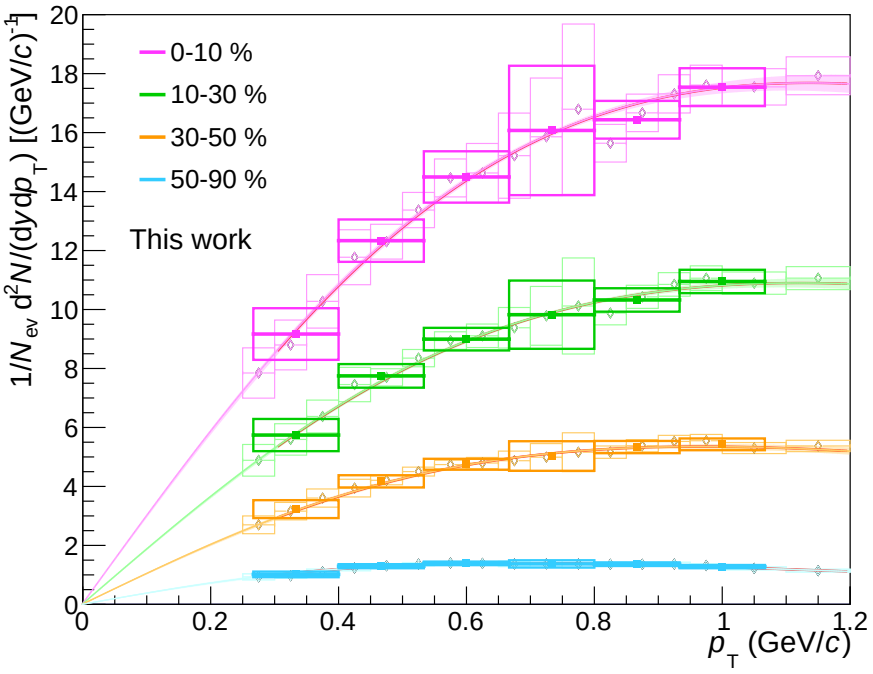

(a) Rebinned proton spectra to match the (anti)triton p_T bins. The first point of each averaged centrality interval was set to the fit value as the measurement only starts from 0.3 GeV/c.

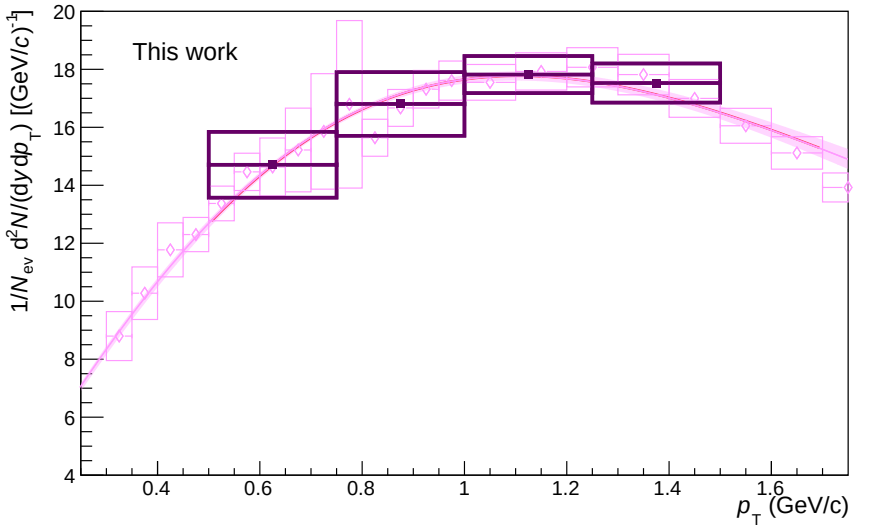

(b) Rebinned proton spectrum to match the (anti)^{4}He p_T bins.

Figure 4.31: Averaged (anti)proton spectra [68] of the 0-5 and 5-10 % (magenta), 10-20 and 20-30 % (green), 30-40 and 40-50 % (orange), and 50-60, 60-70, 70-80 and 80-90 % (blue) centrality intervals with Blast-Wave fits with 3 σ confidence intervals.

to 1.7 GeV/c and then rebinned to match the (anti)^{4}He bins. This is shown in figure 4.31(b).

The statistical and systematic uncertainties are calculated from the ones of the (anti)triton, (anti)^{4}He and (anti)proton spectra with error propagation. The uncertainty of the B_3 was calculated according to the following formula:

$$[\Delta B_3]^2 = \left[\frac{a\Delta Y_{\mathrm{t}}}{(bY_{\mathrm{p}})^3}\right]^2 + \left[3b\frac{aY_{\mathrm{t}}\Delta Y_{\mathrm{p}}}{(bY_{\mathrm{p}})^4}\right]^2 \tag{4.8}$$

where $a = \frac{1}{2\pi p_{\mathrm{T}}^{\mathrm{t}}}$, $b = \frac{1}{2\pi p_{\mathrm{T}}^{\mathrm{p}}}$, Y_{t} is the (anti)triton and Y_{p} the (anti)proton yield.

Accordingly, the uncertainty of the B_4 was calculated with the following equation:

$$[\Delta B_4]^2 = \left[\frac{a\Delta Y_{\alpha}}{(bY_{\mathrm{p}})^4}\right]^2 + \left[4b\frac{aY_{\alpha}\Delta Y_{\mathrm{p}}}{(bY_{\mathrm{p}})^5}\right]^2 \tag{4.9}$$

where $a = \frac{1}{2\pi p_{\mathrm{T}}^{\alpha}}$, Y_{α} is the (anti)^{4}He yield and b and Y_{p} are the same as for equation 4.8.

The B_3 and B_4 will be shown and further discussed in chapter 5 (figures 5.10(a) and 5.10(b), respectively).

5 Final results and discussion

In this chapter the final results will be shown and discussed. From the p_{T} spectra further quantities will be extracted and the results will be brought into a physics context, i.e. compared to different models that were introduced earlier in this thesis as well as to other ALICE measurements.

5.1 Corrected (anti)triton and (anti)^{4}He spectra

Figure 5.1(a) shows the corrected (anti)triton spectra with statistical and systematic uncertainties in four centrality intervals. The statistical uncertainties are shown as error bars, the systematic uncertainties are shown as boxes. The antitritons (full markers) are measured from 0.8 to 3.2 GeV/c, whereas the last data point in the 50-90 % centrality interval should be dropped for reasons of significance (see table 4.8). The tritons (open markers) are only measured from 2.4 GeV/c (or 2.0 GeV/c in the most peripheral centrality interval) to 3.2 GeV/c. It can be seen that the (anti)triton yield is higher for central than more peripheral collisions, as would be expected. It is rising with p_{T}, while this rise is stronger the more central the collisions. In the most peripheral centrality interval the yield is even slightly dropping from about 1.5 GeV/c, while in the 30-50 % centrality interval it slightly drops from about 2.5 GeV/c.

In the last two p_{T} bins of the 0-10 % centrality interval there is a deviation between triton and antitriton. Taking statistical and systematic uncertainties of both data points into account (added quadratically), this deviation is 2.11 σ in the p_{T} bin from 2.4 to 2.8 GeV/c and 1.46 σ in the p_{T} bin between 2.8 and 3.2 GeV/c. For the other data points triton and antitriton are in good agreement. This can also be seen in figure 5.2(a), where the antiparticle-to-particle ratio is shown for the p_{T} bins where a particle and antiparticle measurement is available. It is about unity for most points, as expected at the LHC.

In figure 5.1(b) the corrected (anti)^{4}He spectra in the 0-10 % centrality interval are shown with statistical and systematic uncertainties. The $^4\overline{\mathrm{He}}$ (full markers) is measured from 2 to 6 GeV/c, the ^{4}He (open markers) is measured from 3 to 6 GeV/c. Also here a deviation can be seen between particle and antiparticle, namely in the p_{T} bin between 4 and 5 GeV/c. This deviation is 2.1 σ, taking statistical and systematic uncertainties of

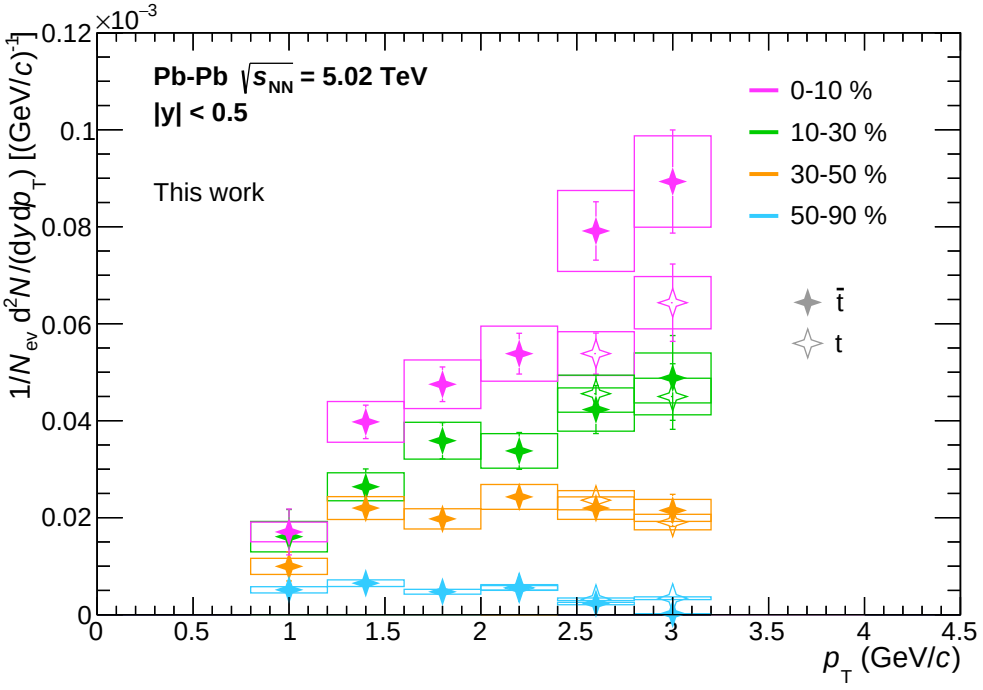

(a) (Anti)tritons.

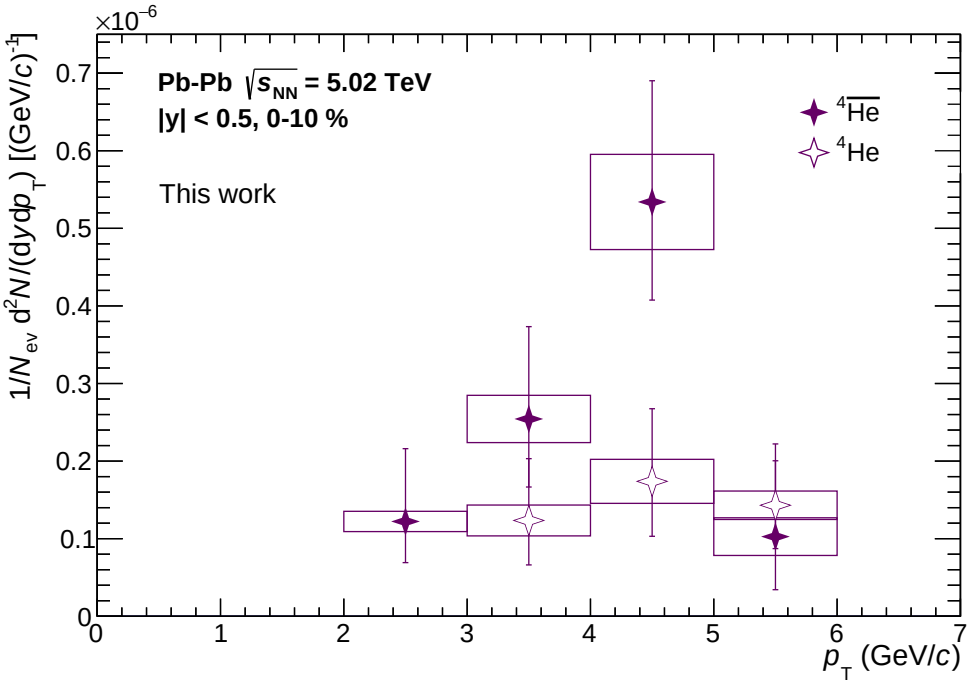

(b) (Anti)^{4}He.

Figure 5.1: Corrected yield versus transverse momentum of (anti)tritons and (anti)^{4}He with statistical (error bars) and systematic (boxes) uncertainties.

both data points into account. In the other p_{T} bins ^{4}He and $^4\overline{\mathrm{He}}$ are in agreement. In the case of the $^4\overline{\mathrm{He}}$ it can be seen nicely that the p_{T} spectrum is rising with p_{T} up to about 4 to 5 GeV/c and then it is dropping again. For ^{4}He this rise is less distinct.

The antiparticle-to-particle ratio for (anti)^{4}He is shown in figure 5.2(b) for the three p_{T} bins where a particle and antiparticle measurement is available. In all p_{T} bins the ratio is compatible with one.

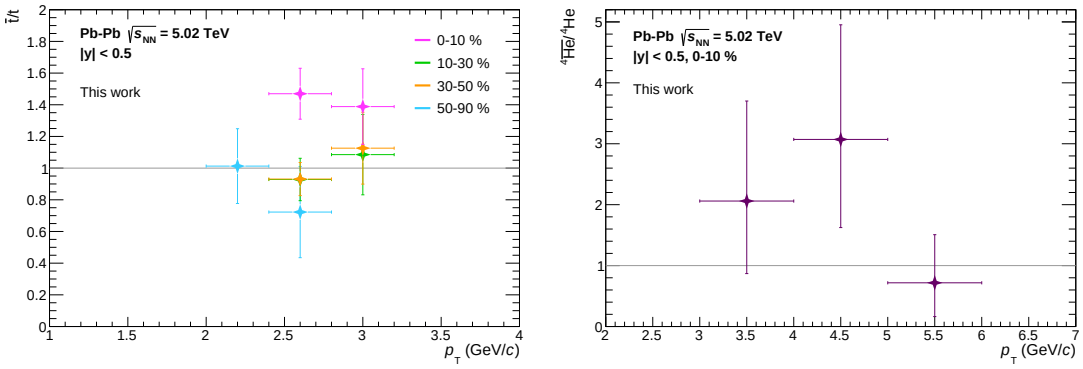

(a) (Anti)tritons.

(b) (Anti)^{4}He.

Figure 5.2: Antiparticle-to-particle ratio versus transverse momentum for (anti)tritons and (anti)^{4}He.

5.2 Blast-Wave fits

The p_{T} spectra can be fitted with Blast-Wave functions (see subsection 1.2.3). This is done for all centrality intervals of the antitritons as well as for (anti)^{4}He (see figures 5.3(a) and 5.3(b)). For the 0-10 % and 10-30 % centrality interval of the (anti)tritons in the last two p_{T} bins the triton points are fitted instead of the antitritons. Otherwise the fit did not converge to reasonable values. This might be an indication that the last two p_{T} bins are subject to statistical fluctuations and systematic effects due to the large background. For the ^{4}He fit the shape of the $^4\overline{\mathrm{He}}$ was adopted, as only three data points are measured for ^{4}He.

The fit parameters of the Blast-Wave fits are stated in table 5.1. β_{max} is in the Blast-Wave model the surface velocity of the isotropically expanding fireball. For the antitritons it is increasing with collision centrality, as would be expected, as a larger fireball results in a higher energy density and pressure gradient. The kinetic freeze-out temperature T_{kin} should decrease the more central the collision is as the fireball freezes out later. This is, with the exception of the 50-90 % centrality interval, also the case.

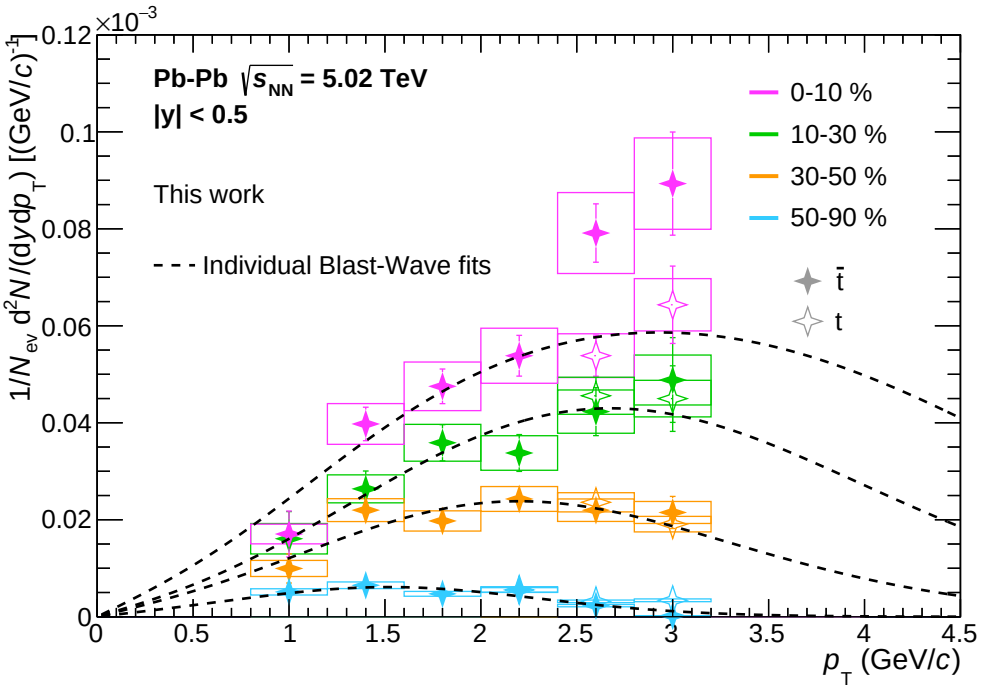

(a) (Anti)tritons.

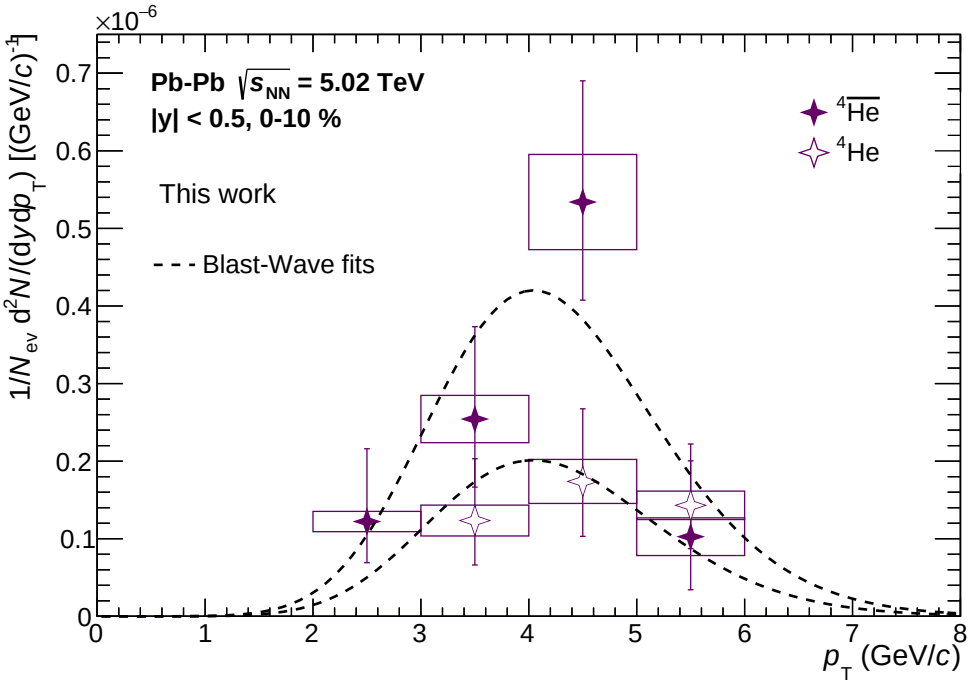

(b) (Anti)^{4}He.

Figure 5.3: p_{T} spectra with statistical and systematic uncertainties and Blast-Wave fits.

The parameter n of the velocity profile is below one and lies between 0.58 and 0.78 for the antitritons. The last parameter *norm* is a normalization. For ^{4}He the parameters $\beta_{\max}$ and T_{kin} were taken from the $^4\overline{\mathrm{He}}$ fit to constrain the shape of the fit.

Table 5.1: Fit parameters of the Blast-Wave fits of antitritons and (anti)^{4}He.

Centrality (%)	$\beta_{\max}$	T_{kin} (MeV)	n	norm
		$\overline{\mathbf{t}}$		
0-10	0.87 ± 0.07	125 ± 6	0.68 ± 0.05	$(7.3 \pm 8.5) \cdot 10^6$
10-30	0.80 ± 0.04	157 ± 11	0.58 ± 0.08	$(3.1 \pm 4.5) \cdot 10^4$
30-50	0.72 ± 0.08	165 ± 9	0.62 ± 0.09	$(5.8 \pm 6.2) \cdot 10^3$
50-90	0.59 ± 0.08	98 ± 4	0.80 ± 0.79	$(3.0 \pm 3.7) \cdot 10^8$
		$^4\overline{\mathbf{He}}$		
0-10	0.72 ± 0.07	132 ± 65	0.01 ± 3.01	$(6.7 \pm 100.1) \cdot 10^6$
		$^4\mathbf{He}$		
0-10	0.72	132	0.01 ± 0.05	$(3.2 \pm 0.97) \cdot 10^6$

5.3 dN/dy and $\langle p_{\mathrm{T}} \rangle$

From the Blast-Wave functions presented in section 5.2 the p_{T}-integrated yield $\mathrm{d}N/\mathrm{d}y$ and the mean p_{T} ($\langle p_{\mathrm{T}} \rangle$) is extracted and stated in table 5.2. The statistical uncertainty of the $\mathrm{d}N/\mathrm{d}y$ is the error of the integral of the fit. The systematic uncertainty is determined by shifting the spectra up and down by their systematic uncertainty and extracting the $\mathrm{d}N/\mathrm{d}y$ correspondingly. The larger difference to the nominal value is taken as systematic uncertainty. For the uncertainty of the $\langle p_{\mathrm{T}} \rangle$ the relative statistical uncertainty of the $\mathrm{d}N/\mathrm{d}y$ is used. Both, $\mathrm{d}N/\mathrm{d}y$ and $\langle p_{\mathrm{T}} \rangle$ are increasing with increasing centrality as one would assume and as can also be seen in figure 5.3(a). For the ^{4}He fit the Blast-Wave function of the $^4\overline{\mathrm{He}}$ is scaled down, this results in a $\mathrm{d}N/\mathrm{d}y$ that is about half that of $^4\overline{\mathrm{He}}$, the deviation between the two values is $1.82\,\sigma$. The weighted average of the $\mathrm{d}N/\mathrm{d}y$ of $^4\overline{\mathrm{He}}$ and ^{4}He is also stated in table 5.2. As weights the quadratic sum of statistical and systematic uncertainties was used. With the averaged $\mathrm{d}N/\mathrm{d}y$ one obtains a penalty factor of $\frac{1}{334}$ between (anti)triton and (anti)^{4}He. This is quite close to the penalty factor of $\frac{1}{330}$ [10], that is obtained in Pb–Pb collisions taking also the lighter nuclei into account.

The $\mathrm{d}N/\mathrm{d}y$ and $\langle p_{\mathrm{T}} \rangle$ can also be plotted versus charged-particle multiplicity. This is done for the four centrality intervals of the antitritons and compared to the ALICE preliminary ^{3}He results [70, 71] (see also section 5.4). For the antitritons the mean charged-particle multiplicities in the four centrality intervals are stated in table 5.2.

Table 5.2: Extracted $\mathrm{d}N/\mathrm{d}y$ and $\langle p_{\mathrm{T}} \rangle$ from the Blast-Wave fits of antitritons and (anti)^{4}He. Also stated is the mean charged-particle multiplicity $\langle \mathrm{d}N_{\mathrm{ch}}/\mathrm{d}\eta_{\mathrm{lab}} \rangle$ in the different centrality intervals [69].

Centrality (%)	$\mathrm{d}N/\mathrm{d}y$	$\langle p_{\mathrm{T}} \rangle$ (GeV/c)	$\langle \mathrm{d}N_{\mathrm{ch}}/\mathrm{d}\eta_{\mathrm{lab}} \rangle$
	$\overline{\mathbf{t}}$		
0-10	$(2.37 \pm 0.13 \pm 0.21) \cdot 10^{-4}$	3.34 ± 0.18	1765 ± 52
10-30	$(1.40 \pm 0.07 \pm 0.13) \cdot 10^{-4}$	2.95 ± 0.15	983 ± 39.5
30-50	$(6.55 \pm 0.31 \pm 0.70) \cdot 10^{-5}$	2.45 ± 0.12	415 ± 13.5
50-90	$(1.16 \pm 0.29 \pm 0.13) \cdot 10^{-5}$	1.63 ± 0.41	85.43 ± 4.77
	$^4\overline{\mathbf{He}}$		
0-10	$(1.10 \pm 0.22 \pm 0.14) \cdot 10^{-6}$	4.25 ± 0.87	1765 ± 52
	^{4}He		
0-10	$(0.53 \pm 0.16 \pm 0.08) \cdot 10^{-6}$	4.25 ± 1.28	1765 ± 52
	Weighted average of $^4\overline{\mathrm{He}}$ and ^{4}He		
0-10	$(0.71 \pm 0.13 \pm 0.07) \cdot 10^{-6}$	–	1765 ± 52

For the preliminary ^{3}He the centrality intervals are 0-10 %, 10-40 % and 40-90 %. The $\mathrm{d}N/\mathrm{d}y$, $\langle p_{\mathrm{T}} \rangle$ and $\langle \mathrm{d}N_{\mathrm{ch}}/\mathrm{d}\eta_{\mathrm{lab}} \rangle$ are stated in table 5.3.

Table 5.3: $\mathrm{d}N/\mathrm{d}y$ and $\langle p_{\mathrm{T}} \rangle$ of ^{3}He (taken from [70]). Also stated is the mean charged-particle multiplicity $\langle \mathrm{d}N_{\mathrm{ch}}/\mathrm{d}\eta_{\mathrm{lab}} \rangle$ in the different centrality intervals [69].

Centrality (%)	$\mathrm{d}N/\mathrm{d}y$	$\langle p_{\mathrm{T}} \rangle$ (GeV/c)	$\langle \mathrm{d}N_{\mathrm{ch}}/\mathrm{d}\eta_{\mathrm{lab}} \rangle$
0-10	$(2.70 \pm 0.13 \pm 0.59) \cdot 10^{-4}$	3.06 ± 0.35	1765 ± 52
10-40	$(1.45 \pm 0.07 \pm 0.28) \cdot 10^{-4}$	2.84 ± 0.29	826 ± 20
40-90	$(3.18 \pm 0.30 \pm 0.59) \cdot 10^{-5}$	1.99 ± 0.16	132.44 ± 10

One can see in figure 5.4(a) that the larger the charged-particle multiplicity, the larger the $\mathrm{d}N/\mathrm{d}y$. It is basically following a linear trend.

Figure 5.4(b) shows the $\langle p_{\mathrm{T}} \rangle$ of antitriton and ^{3}He as a function of charged-particle multiplicity. It is first increasing at small multiplicities and then saturating at larger multiplicities following the trend of other charged particles [68].

Figure 5.4(c) shows the $\langle p_{\mathrm{T}} \rangle$ of pions, kaons, protons, deuterons, antitritons, ^{3}He and $^4\overline{\mathrm{He}}$ versus the mass of the particles in central Pb–Pb collisions (0-10 % centrality interval) fitted with a straight line. The fit is with a slope of 1.05 ± 0.03 approximately proportional to the particles' mass with an offset of 0.41 ± 0.02. This is compatible with a common flow velocity of all particles. The newly measured $^4\overline{\mathrm{He}}$ data point extends this spectrum to higher masses.

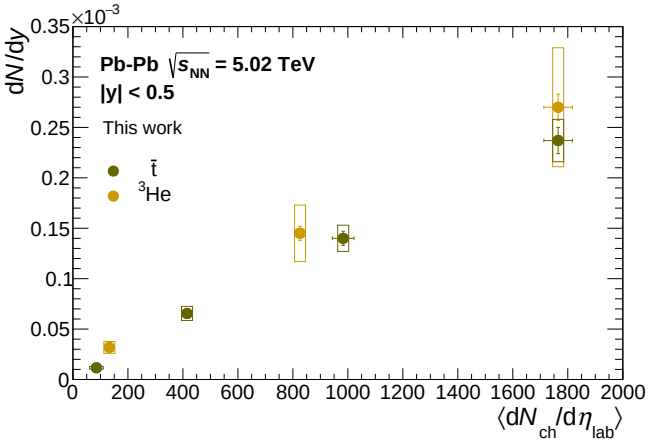

(a) $\mathrm{d}N/\mathrm{d}y$ versus charged-particle multiplicity.

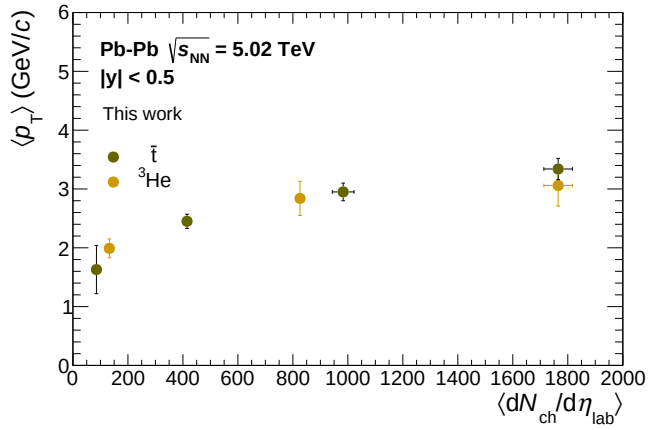

(b) $\langle p_{\mathrm{T}} \rangle$ versus charged-particle multiplicity.

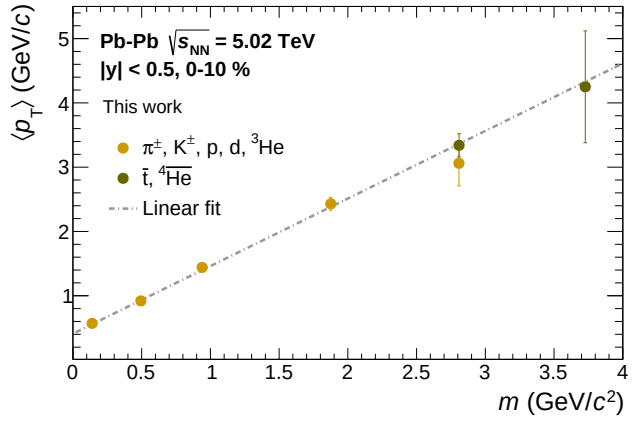

(c) $\langle p_{\mathrm{T}} \rangle$ versus mass.

Figure 5.4: Extracted $\mathrm{d}N/\mathrm{d}y$ (top) and $\langle p_{\mathrm{T}} \rangle$ (middle) from the Blast-Wave fits of antitritons and ^{3}He versus charged-particle multiplicity. Also shown is the $\langle p_{\mathrm{T}} \rangle$ of π, K and several nuclei in the 0-10 % centrality interval versus their mass with a linear fit (bottom).

5.4 Comparison of (anti)tritons with (anti)^{3}He

There is an ALICE preliminary measurement of ^{3}He and $^3\overline{\text{He}}$ [70, 71] in the Pb–Pb data set at $\sqrt{s_{\text{NN}}} = 5.02$ TeV from 2015. Figure 5.5(a) shows this measurement together with the (anti)triton p_{T} spectra. The preliminary (anti)^{3}He p_{T} spectra have been extracted in 3 centrality intervals, 0-10 %, 10-40 % and 40-90 %. (Anti)^{3}He can be measured with the TPC alone, as it has a charge of two and thus, like ^{4}He, a larger energy loss in the TPC compared to the particles with charge one. Therefore the spectra can be extracted up to much larger p_{T}.

As triton and ^{3}He have similar masses, it is expected that they are produced in about the same amount. In the overlap region of the 0-10 % centrality interval (anti)triton (magenta) and (anti)^{3}He (red) p_{T} spectra are compatible with each other. In the 10-40 % centrality interval of the (anti)^{3}He (dark blue) the spectra are lying between the 10-30 % (light green) and 30-50 % (yellow) centrality interval of the (anti)tritons, a little bit closer to the 10-30 % centrality interval. In the most peripheral centrality interval of both nuclei the p_{T} spectra (light blue and dark green) are also compatible with each other, while the (anti)^{3}He spectra are a bit higher.

In figure 5.5(b) the antiparticle-to-particle ratios of (anti)triton and (anti)^{3}He in the different centrality intervals are shown. They are basically fluctuating around one, as expected at the LHC, where the baryochemical potential is basically zero.

Figure 5.5(c) shows the (anti)triton and $^3\overline{\text{He}}$ p_{T} spectra in the 0-10 % centrality interval with BW fits. One of the BW functions is fitted to the (anti)triton data points only. It is the same that is also shown in figure 5.3(a). The other BW fit is using the (anti)triton and $^3\overline{\text{He}}$ data points together. One can see that the fits are basically on top of each other. In table 5.4 the fit parameters as well as the $\mathrm{d}N/\mathrm{d}y$ and $\langle p_{\text{T}} \rangle$ of the fit to (anti)triton and $^3\overline{\text{He}}$ combined are stated. $\mathrm{d}N/\mathrm{d}y$ and $\langle p_{\text{T}} \rangle$ are within uncertainties in agreement with the BW fit only to (anti)triton (see table 5.2). T_{kin} is a bit smaller, as the fit is slightly more narrow, β_{max} and n basically stayed the same (see table 5.1).

Table 5.4: Fit parameters, $\mathrm{d}N/\mathrm{d}y$ and $\langle p_{\text{T}} \rangle$ of the Blast-Wave fit of (anti)tritons and $^3\overline{\text{He}}$ fitted together.

(Anti)tritons + $^3\overline{\text{He}}$				
Centrality (%)	β_{max}	T_{kin} (MeV)	n	*norm*
0-10	0.87 ± 0.004	107 ± 0.002	0.64 ± 0.04	$(4.0 \pm 1.6) \cdot 10^8$
	$\mathrm{d}N/\mathrm{d}y$		$\langle p_{\text{T}} \rangle$ (GeV/c)	
	$(2.26 \pm 0.07 \pm 0.26) \cdot 10^{-4}$		3.32 ± 0.11	

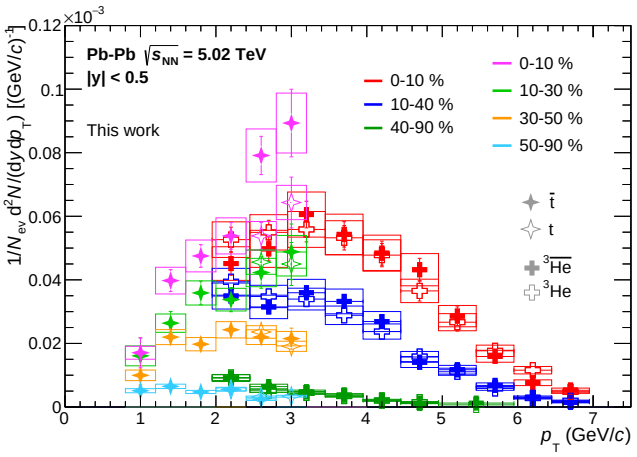

(a) p_{T} spectra in all centrality intervals.

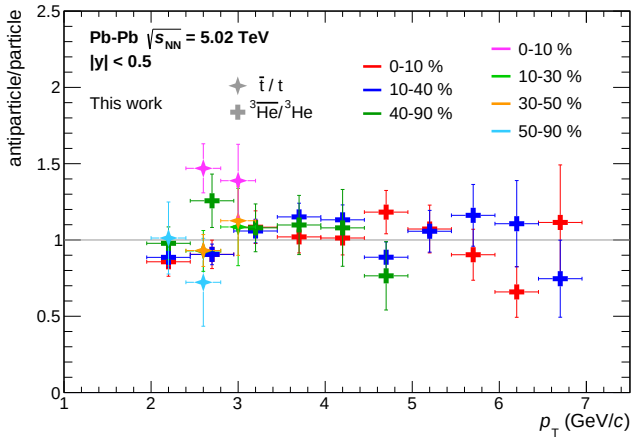

(b) Antiparticle-to-particle ratio.

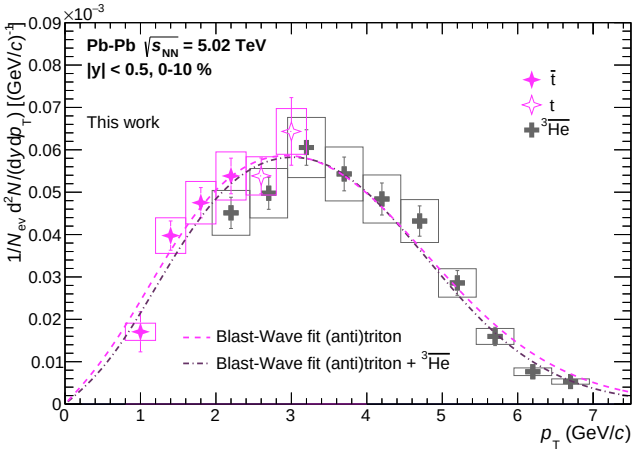

(c) Comparison of the (anti)triton BW fit to a BW fit of (anti)triton with ALICE preliminary $^3\overline{\mathrm{He}}$ [70, 71] combined in the 0-10 % centrality interval.

Figure 5.5: Comparison of (anti)triton to ALICE preliminary (anti)^{3}He [70, 71].

The agreement of the p_{T} spectra of (anti)triton and (anti)^{3}He is also a check of isospin symmetry in particle production which is expected to be restored at the LHC. The only difference between triton and ^{3}He is one neutron that is replaced with a proton, which are isospin partners (see also subsection 5.7.2). Usually isospin symmetry is only tested through charged pions. Figure 5.6(c) shows the ratios of $\bar{\mathrm{t}}$ to $^3\overline{\mathrm{He}}$ and t to ^{3}He p_{T} spectra in the overlapping region in the 0-10 % centrality interval. The (anti)^{3}He p_{T} spectra have been rebinned before to the bins of the (anti)triton analysis using a Blast-Wave fit as weight (see figures 5.6(a) and 5.6(b)). The $\bar{\mathrm{t}}$ to $^3\overline{\mathrm{He}}$ ratio is slightly above one, especially in the last two p_{T} bins. The t to ^{3}He ratio is in good agreement with one.

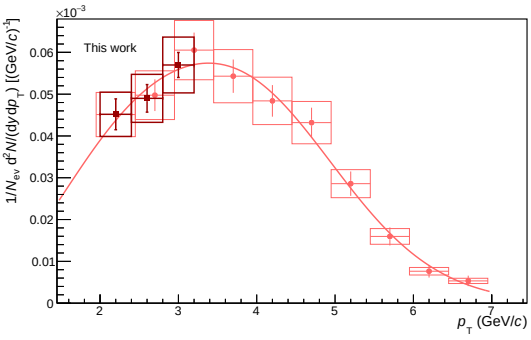

(a) Fitted and rebinned $^3\overline{\mathrm{He}}$ p_{T} spectrum to the $\bar{\mathrm{t}}$ bins.

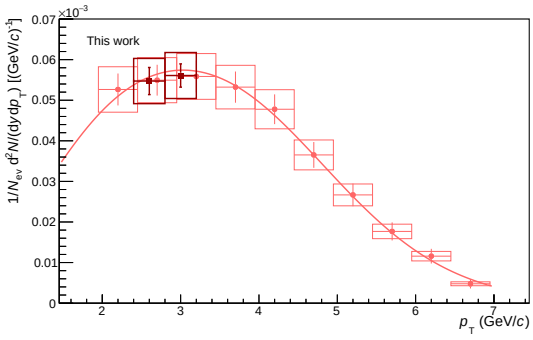

(b) Fitted and rebinned ^{3}He p_{T} spectrum to the t bins.

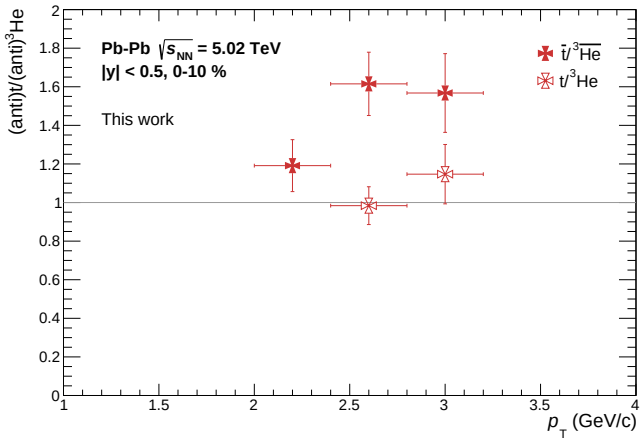

(c) Ratio of (anti)triton to (anti)^{3}He p_{T} spectra in the overlapping region.

Figure 5.6: Fitted and rebinned (anti)^{3}He p_{T} spectra [70, 71] (top) and ratio of (anti)triton to (anti)^{3}He p_{T} spectra in the 0-10 % centrality interval.

5.5 Combined Blast-Wave fit

The p_{T} spectra of several particle species, namely π, K, p [68], d and ^{3}He, have been fitted together with the $\bar{\mathrm{t}}$ and $^4\overline{\mathrm{He}}$ with a combined Blast-Wave fit, where all fit parameters except for the particle mass and the normalization are identical for all spectra. In figure 5.7(a) one can see that the fit describes all particle spectra quite well. This is even emphasized in figure 5.7(b), where the ratio of the data to the fit is shown. It means that all particles follow a common radial flow field with mean common flow velocity $\langle\beta\rangle$ and freeze-out temperature T_{kin} that can be extracted from the fit. The fit parameters are listed in table 5.5. In figure 5.7(a) one can also see that antitriton and ^{3}He are compatible with each other as it should be because of their similar mass. At high p_{T}, the spectra of the lighter particles cannot be described by the Blast-Wave fit, this is expected as at high p_{T} the spectral shape is dominated by high-p_{T} processes, like jets.

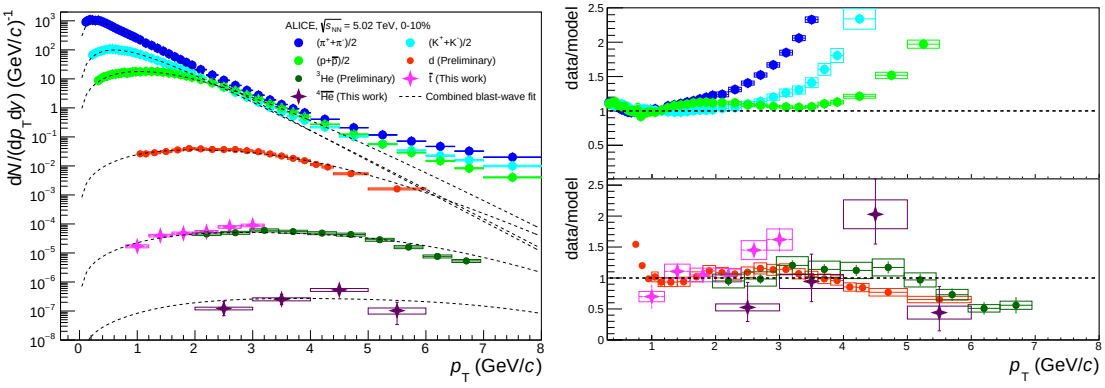

(a) p_{T} spectra.

(b) Ratio data over model.

Figure 5.7: Combined Blast-Wave fit of several particle species, including $\bar{\mathrm{t}}$ and $^4\overline{\mathrm{He}}$, in Pb–Pb collisions at $\sqrt{s_{\mathrm{NN}}} = 5.02\,\mathrm{TeV}$ in the 0-10 % centrality interval.

Table 5.5: Fit parameters of the combined Blast-Wave fit.

Particle	$\langle\beta\rangle$ (β_{max})	T_{kin} (MeV)	n	norm
π	0.661 ± 0.003 (0.895 ± 0.025)	98 ± 1	0.71 ± 0.02	$(7.36 \pm 0.31) \cdot 10^5$
K				$(1.34 \pm 0.09) \cdot 10^6$
p				$(1.49 \pm 0.16) \cdot 10^7$
d				$(2.76 \pm 0.55) \cdot 10^8$
^{3}He				$(3.88 \pm 1.12) \cdot 10^9$
t				$(3.72 \pm 1.13) \cdot 10^9$
^{4}He				$(1.30 \pm 0.51) \cdot 10^{11}$

5.6 Thermal model fit

The p_{T}-integrated production yields $\mathrm{d}N/\mathrm{d}y$ of different particle species, extracted from individual Blast-Wave fits, have been compared with four different variants of the thermal model. The fit is done using the Thermal-FIST package [72]. The comparison includes light (anti)particles and hyperons as well as light (anti)(hyper)nuclei (see figure 5.8). The antitriton and (anti)^{4}He yields are shown on the right most positions. The red open circles represent the data, while the different lines represent the models. μ_{B} was fixed to zero in all models (similar as in [19, 73, 74]). In the lower panel the deviation of the data to the models is shown in units of σ (standard deviation). Overall one can say that the models are in quite good agreement with the measured production yields over several orders of magnitude. For most models and most particles the deviation is less than $2\,\sigma$. However, there are also outliers where the deviation is up to $4\,\sigma$. In case of the antitriton most models have a deviation of only $1\,\sigma$. For the ^{4}He the deviation between the models to the data point is even smaller and has a value of about $0.5\,\sigma$ for all models. In case of the $^4\overline{\mathrm{He}}$ a discrepancy is visible between the data point and the models. However, as the uncertainty of the data point is quite large, the deviation is still only $2.5\,\sigma$.

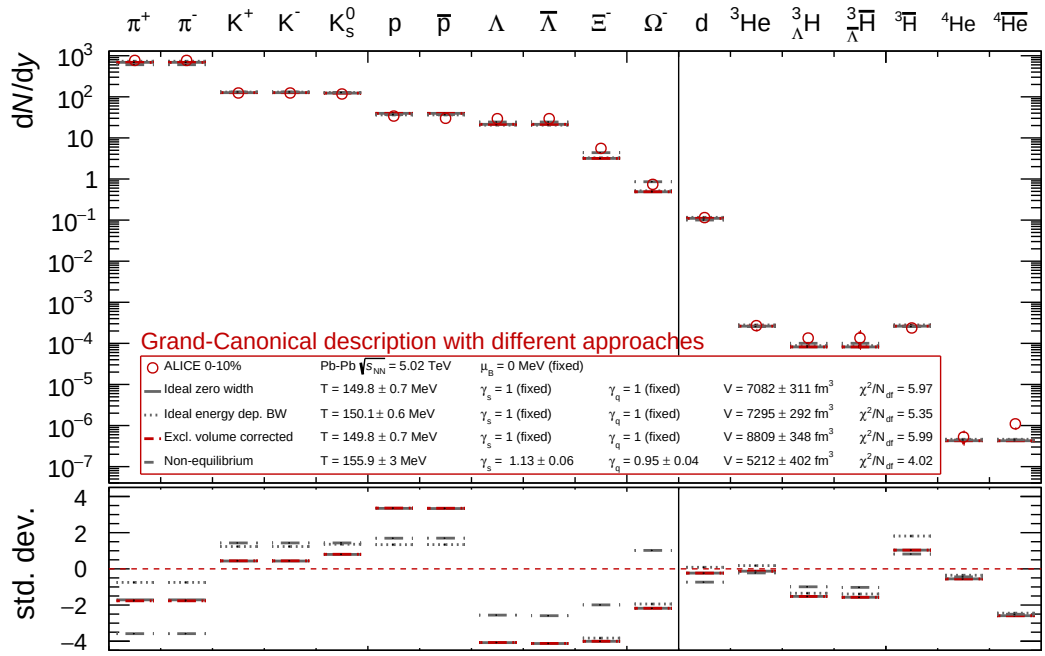

Figure 5.8: p_{T}-integrated production yields $\mathrm{d}N/\mathrm{d}y$ of different particle species, including $\overline{\mathrm{t}}$ and $^4\overline{\mathrm{He}}$, in Pb–Pb collisions at $\sqrt{s_{\mathrm{NN}}} = 5.02\,\mathrm{TeV}$ in the 0-10 % centrality interval fitted with four implementations of the thermal model.

The *Ideal zero width* model was mentioned earlier in this work as HRG (see figure 1.9). It assumes that the particles are point like and don't interact with each other. The HRG does not describe the protons very well [73, 75, 76].

The *Ideal energy dependent Breit-Wigner (BW)* model takes the widths of the resonances into account. So, the resonances can contribute differently according to their mass. This results in a better description of the protons and pions [72, 73, 77, 78].

The *Excluded volume corrected* model assumes a volume with 0.3 fm radius for all particles, which means there is an effective interaction between the particles [23, 24].

In the *Non-equilibrium* model the particles are point like. This model has two more parameters that allow non-equilibrium between u and d quarks (γ_{q}) and s quarks (γ_{s}), which are stated in the legend of the plot [79, 80, 81].

The chemical freeze-out temperature extracted from the fits is around 150 MeV for all models except for the non-equilibrium model, where it is 156 MeV. The extracted source volume is between 5212 and 8809 fm^3. T_{ch} and V for the different model variants are also stated in the legend of the plot.

5.7 Baryochemical potential and isospin

In this section the baryochemical potential and the isospin are calculated from the ratios shown in figures 5.2 and 5.6(c), respectively.

5.7.1 Baryochemical potential

The extracted antiparticle-to-particle ratios (figure 5.2) can be used to determine the baryochemical potential μ_{B}. In most thermal model fits μ_{B} is set to zero at the LHC as it is expected that particles and antiparticles are produced equally. Without fixing μ_{B} a thermal model fit to the produced particle yields at $\sqrt{s_{\mathrm{NN}}} = 5.02$ TeV results in a μ_{B} of -0.2 MeV$\pm$2.2 MeV [82]. This value is in good agreement with zero.

By assuming the temperature is constant as a function of centrality, the baryochemical potential can be calculated from the antiparticle-to-particle ratios according to the following formulae [83]:

$$\frac{n_{\bar{\mathrm{t}}}}{n_{\mathrm{t}}} = \exp(-6\mu_{\mathrm{B}}/T) \tag{5.1}$$

for (anti)tritons and accordingly

$$\frac{n_{\overline{^4\mathrm{He}}}}{n_{^4\mathrm{He}}} = \exp(-8\mu_{\mathrm{B}}/T) \tag{5.2}$$

for (anti)^{4}He. For the temperature a value of 150 MeV, which is the result from the thermal model fits in section 5.6, was used for all centrality intervals. For the values of the ratios a constant fit to the ratios in the different p_{T} bins was performed. This was done for all centrality intervals individually. In table 5.6 the results from the constant fits and the calculated baryochemical potentials are stated.

Table 5.6: Antiparticl-to-particle ratios and calculated μ_{B} for (anti)tritons and (anti)^{4}He.

(Anti)tritons		
Centrality (%)	antiparticle-to-particle ratio	μ_{B} (MeV)
0-10	1.44 ± 0.13	$-9.2\,^{+2.4}_{-2.2}$
10-30	0.96 ± 0.12	$0.96\,^{+3.28}_{-2.90}$
30-50	0.97 ± 0.09	$0.89\,^{+2.59}_{-2.35}$
50-90	0.90 ± 0.18	$2.74\,^{+5.69}_{-4.63}$
(Anti)^{4}He		
0-10	1.46 ± 0.60	$-7.1\,^{+7.4}_{-6.5}$

Except for the (anti)tritons in the 0-10 % centrality interval, the values are in the uncertainties in good agreement with the fit to all particles and no particularity, like for example an excessive production of antimatter with respect to matter, is recognizable like is expected in some older predictions [84, 85].

5.7.2 Isospin

As mentioned already, the ratio of (anti)triton to (anti)^{3}He (see figure 5.6(c)) is closely connected to the isospin symmetry. As at the LHC no experiments are able to measure neutrons at midrapidity, the only possibility to test isospin symmetry is to use mirror nuclei that have the same number of nucleons A, but different number of protons Z and neutrons N. Isospin means here the third component I_3 of the isospin vector. It is defined as $0.5 \cdot (n_u - n_d)$, so the difference between u and d quark content. As the difference between the quark content of proton and neutron is exactly one u quark that is replaced by a d quark the difference between proton and neutron production has to be measured. However, in the most variants of the thermal model not the isospin but directly the charge-chemical potential μ_{Q} is utilized. μ_{Q} and $\mu_{\mathrm{I_3}}$ can be converted in each other via the Gell-Mann-Nishijima-formula ($Q = I_3 + 0.5(B + S)$), where Q is the charge number, B the baryon number and S the strangeness [86, 87].

The Q to B ratio in Pb–Pb collisions is initially fixed to about 0.4 (82/208). This is besides the conservation laws an additional important constraint in the thermal model description of particle production in heavy-ion collisions. As already mentioned, in heavy-

ion collisions the grand-canonical ensemble is used. Therefore the chemical potentials are necessary to conserve the associated quantum numbers on average. μ_{Q} and μ_{S} are fixed by conservation laws. In a typical fit μ_{Q} results in -0.1 MeV. This value is mainly determined by the charged pions, which also only differ in their quark content by one d versus one u quark. Table 5.7 shows the (anti)t to (anti)^{3}He ratios determined by a constant fit to the ratios of the single p_{T} bins in figure 5.6(c), as well as the determined values of μ_{Q} from a thermal model fit. Using the antiparticle ratio to determine μ_{Q} results in a quite high μ_{Q}, which leads to extreme tension in the description of the particle abundances ($\chi^2/\mathrm{NDF} = 10.9$!). This is due to the large antitriton yield in these p_{T} bins. However, using the particle ratios the result is in agreement with all expectations, which means in this case isospin symmetry is definitely granted.

Table 5.7: (Anti)t to (anti)^{3}He ratios and μ_{Q}.

(Anti)particles	ratio	μ_{Q} (MeV)
$\overline{\mathrm{t}}/\overline{^3\mathrm{He}}$	1.40 ± 0.09	49.7 ± 9.2
$\mathrm{t}/^3\mathrm{He}$	1.03 ± 0.08	5.0 ± 12.1

The pure mass difference of triton and ^{3}He of only 529.5255 keV ($\mathrm{m_t}$ = 2808.92113298 MeV, $\mathrm{m_{^3He}}$ = 2808.3916074 MeV) leads at a temperature of 150 MeV to a difference in their productions of maximal 0.35 %. Thus, a difference of 3 % and more cannot be explained by the mass difference but rather by the baryochemical or charge-chemical potential.

5.8 Ratio of production yields

The ratio of the integrated production yield $\mathrm{d}N/\mathrm{d}y$ for $A = 3$ nuclei (triton and ^{3}He) over the proton yield has been studied as a function of mean charged-particle multiplicity ($\langle \mathrm{d}N_{\mathrm{ch}}/\mathrm{d}\eta \rangle$) for different collision systems and center-of-mass energies (see figure 5.9). This means on the left of the plot the pp collisions are located and going to larger $\langle \mathrm{d}N_{\mathrm{ch}}/\mathrm{d}\eta \rangle$ the p–Pb, peripheral Pb–Pb and on the right the central Pb–Pb collisions can be found. The four dark magenta markers are the four centrality intervals of the antitritons. Overall a clear trend can be observed, showing an increasing behaviour with increasing multiplicity from pp to p–Pb collisions and a saturation at high multiplicities (Pb–Pb collisions). This trend can be rather well described by both, coalescence [88] and thermal [77] models. The thermal model is shown for two different correlation volumes, in which all quantum numbers are conserved explicitly (black solid and dashed lines). The coalescence model is shown as two-body and three-body coalescence (magenta and

orange lines, respectively). In two-body coalescence, the coalescence happens between a deuteron and a proton or neutron for ^{3}He or triton, respectively. In three-body coalescence, the coalescence happens between two protons and one neutron or two neutrons and one proton. The antitriton points are closer to the coalescence model. However, at high multiplicities, like in Pb–Pb collisions, there is no difference between two-body and three-body coalescence. So, no statement can be made about this with the antitriton data points.

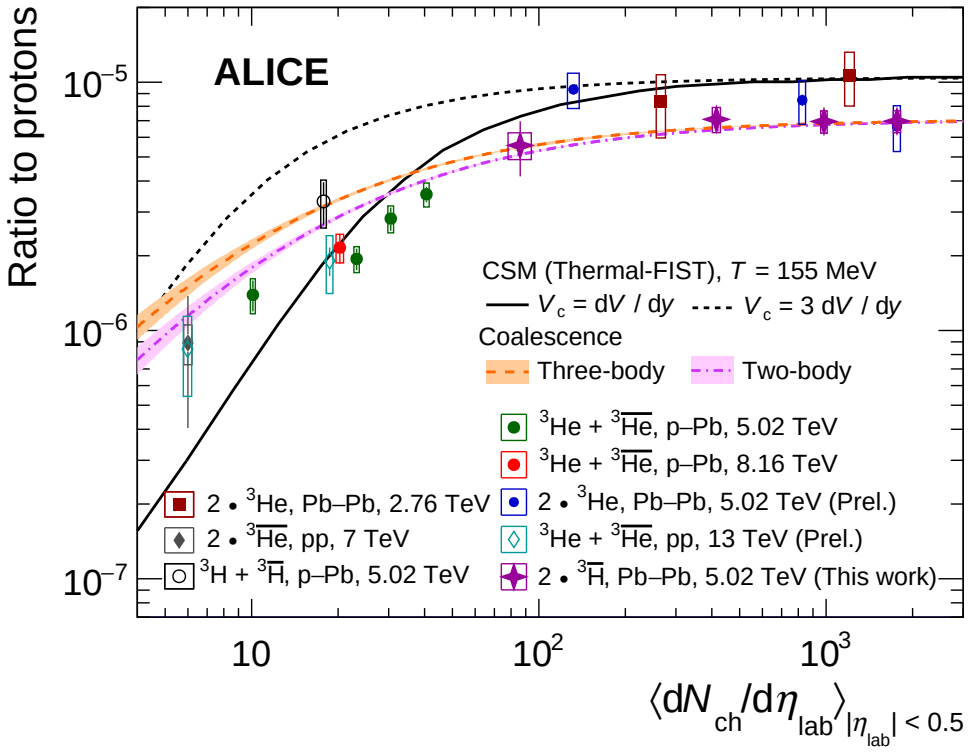

Figure 5.9: Ratio of p_{T}-integrated production yield $\mathrm{d}N/\mathrm{d}y$ for triton and ^{3}He (A=3 nuclei) over the proton yield versus mean charged-particle multiplicity. The data is compared to theoretical model predictions [88, 77].

5.9 Coalescence parameters

The determination of the coalescence parameters was explained in section 5.9. B_3 and B_4 are shown versus p_{T}/A in figures 5.10(a) and 5.10(b), respectively. As was mentioned earlier, the coalescence parameter is related to the probability to form a nucleus. One can see that the B_3 is larger for peripheral collisions and smallest for the most central

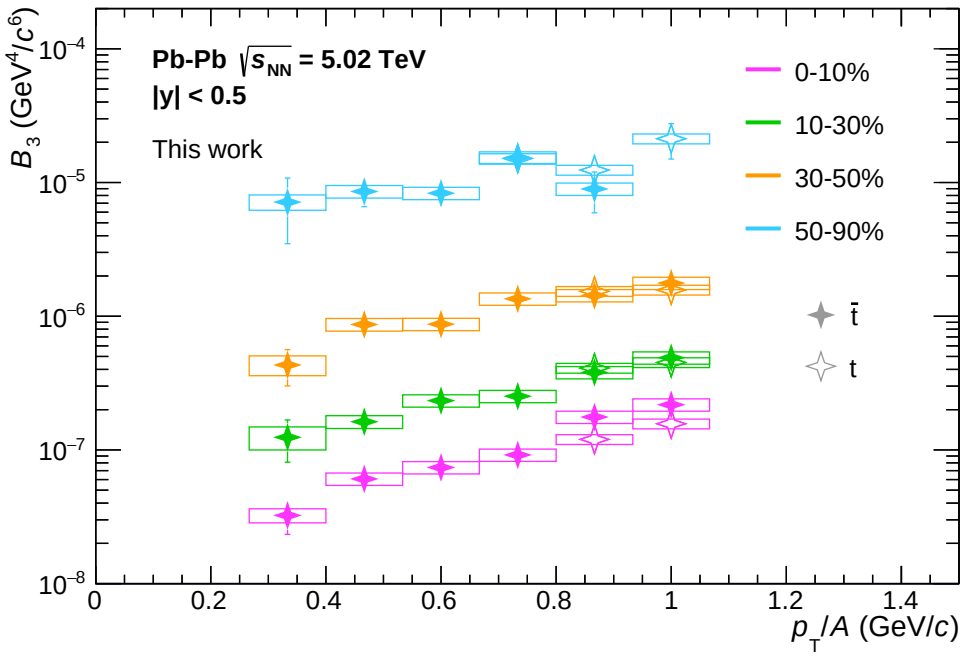

(a) B_3.

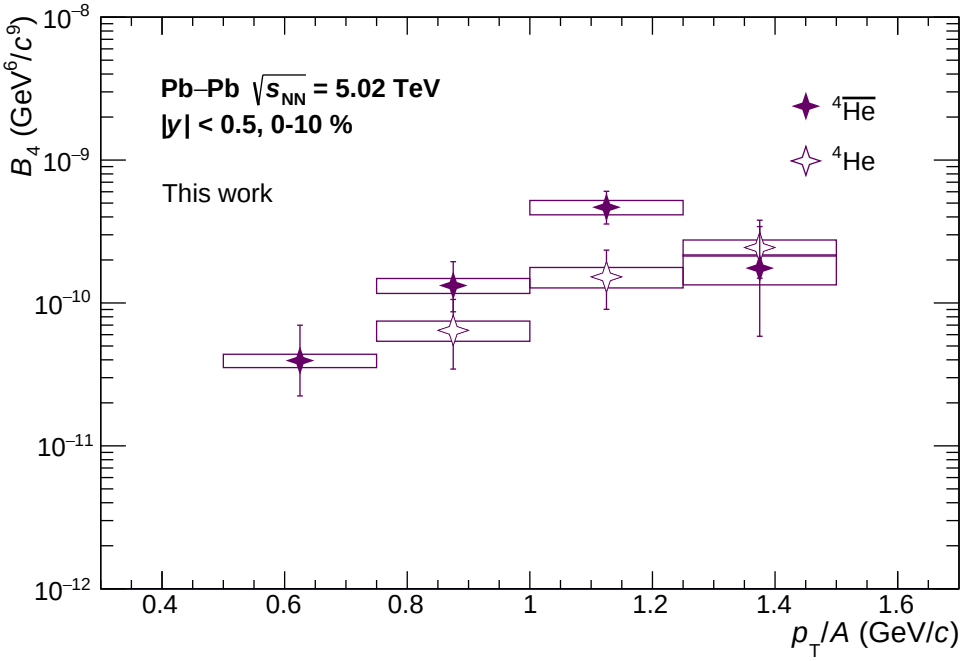

(b) B_4.

Figure 5.10: Coalescence parameters B_3 of (anti)tritons and B_4 of (anti)^{4}He versus transverse momentum.

collisions. This can be explained with the size of the source. In peripheral collisions the source size is smaller than in central collisions, so it is easier for the nucleons to come close to each other than it is in central collisions, where the source size is much larger. It can also be observed that the B_A is rising with p_{T}/A, as higher p_{T} particles are originating from a smaller region of the source [27].

The B_4 is about three orders of magnitude smaller than the B_3 at central collisions. It is obvious that the probability to form a nucleus is decreasing with the number of nucleons it is built of. Also the B_4 is rising with p_{T}.

The measured coalescence parameters were compared to coalescence and statistical-hadronization models [26]. B_3 and B_4 are plotted versus multiplicity for a certain p_{T}/A.

In figure 5.11(a) the B_3 of the antitritons at 2.2 GeV/c versus charged-particle multiplicity compared to models is shown. The mean charged-particle multiplicities for the four centrality intervals are stated in table 5.2. The data points are closer to the BW+GSI-Heidelberg model than to the coalescence model. However, the models are both close to each other.

In figure 5.11(b) the weighted averaged B_4 of $^4\overline{\mathrm{He}}$ and ^{4}He at 3.5 GeV/c compared to the models is shown. In the publication the models are shown at $p_{\mathrm{T}}/A = 0.75\,\mathrm{GeV}/c$ but in order to match the binning of the (anti)^{4}He data points they where calculated at $p_{\mathrm{T}}/A = 0.875\,\mathrm{GeV}/c$ for the comparison. The data point is lying a bit above both models and is closer to the BW+GSI-Heidelberg.

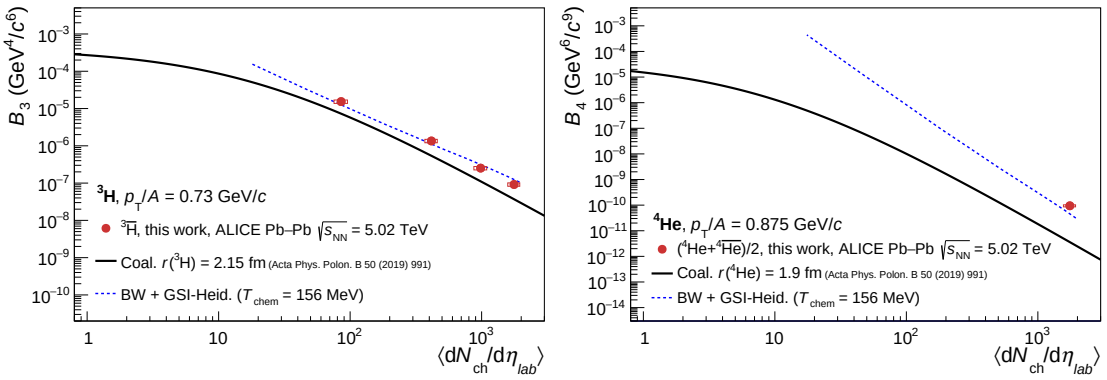

(a) B_3 of antitritons at $p_{\mathrm{T}}/A = 0.73$ GeV/c.

(b) B_4 of $^4\overline{\mathrm{He}}$ and ^{4}He averaged at $p_{\mathrm{T}}/A = 0.875\,\mathrm{GeV}/c$.

Figure 5.11: Measured coalescence parameters versus charged-particle multiplicity compared to coalescence and BW + GSI-Heidelberg models.

6 Outlook – Future ALICE running at high rate

The presented results for anti(triton) and (anti)^{4}He production in Pb–Pb collisions are still substantially limited by the available event statistics. In the upcoming, soon starting, Run 3 data-taking period of the LHC the interaction rate in Pb–Pb collisions will be increased to 50 kHz. It is planned to gather at least a factor 100 more data with respect to Run 2, of which the (anti)triton and (anti)^{4}He analyses will highly benefit. The statistical uncertainties will be decreased significantly and it will probably even be possible to extract the (anti)^{4}He p_{T} spectra in more peripheral centrality intervals and extend the analysis to even rarer objects.

The planned high interaction rates made some major upgrades of the ALICE detector setup irremissible, as was briefly discussed in subsection 3.3.5. One of the major upgrades was the exchange of the TPC's readout chambers, which took place in 2019 during Long Shutdown 2. The MWPCs with gating grid (see subsection 3.3.2 (3)) were much too slow and a solution had to be found to allow for a continuous readout of the heavy-ion collisions. A solution that prevented the ions produced in the amplification process to flow back in the drift volume, where they would lead to space charges and thus distortions of the otherwise highly uniform electric drift field. But it had to be a solution without gating grid.

The new readout chambers exploit a completely different technique for the gas amplification than the former ones. Instead of MWPCs stacks of four GEM foils are utilized. Therefore an extensive R&D program was necessary to characterize and test the GEM-based readout for the first ever built large-size GEM TPC. As part of this R&D program, in the beginning of this doctoral study, a systematic investigation of ion backflow and energy resolution in quadruple GEM stacks using different types of GEM foils was performed.

A GEM foil is a 50 μm thick insulating Kapton layer with 5 μm thick copper electrodes on both sides, where a voltage difference of some hundred volts can be applied. In the foil there are holes with a diameter of 70 μm. Due to the high electric fields in the holes gas amplification occurs. The distance of these holes depends on the type of the GEM foil.

Measurements with *Standard* (S), *Large-Pitch* (LP) and *Small-Pitch* (SP) GEM foils have been performed. In a *Standard* GEM foil the distance of the holes is 140 μm. LP foils have a hole distance of 280 μm, SP foils of 90 μm. Figure 6.1(a) shows an electron microscope picture of a standard GEM foil. The holes are arranged in hexagonal shape.

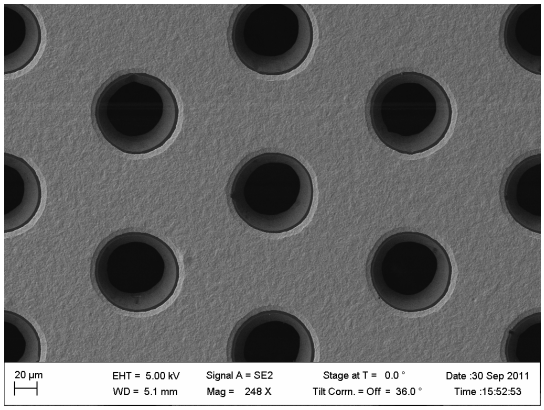

(a) Electron microscope picture of a standard GEM foil.

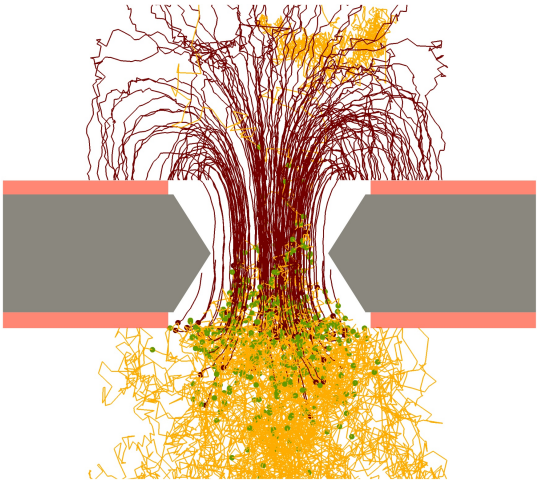

(b) Garfield/Magboltz simulation of the gas amplification in a GEM hole.

Figure 6.1: Picture of a GEM foil (left) and simulation of the gas amplification process (right) [48].

Figure 6.1(b) shows a Garfield/Magboltz simulation of the gas amplification process inside a GEM hole. GEM foils have intrinsic ion-blocking capabilities. The electrons are flowing in one direction and the ions created in the amplification process are flowing back. This is the so called ion backflow (IBF). One can see in the simulation, that some field lines and thus ions end on the top electrode. However, many are also flowing back in the drift volume. The advantage of GEM foils is that several can be arranged on top of each other. In such a stack a high field can be applied below the GEM foil to extract as many electrons as possible and a low field can be applied above, so as many field lines as possible end on the upper electrode. By a combination of different GEM foils and settings of GEM voltages and electric fields between the GEMs the amplification is distributed between several layers. The goal is that as many electrons as possible pass the foils in one direction while as little as possible ions pass in the other direction.

However, a stack of GEM foils does not block the ions as efficient as a gating grid. It was found that one percent of back-drifting ions into the TPC's drift volume at a gas gain of 2000 is tolerable, as the resulting space-charge distortions are less than 10 cm

and can be calibrated later with sufficient precision [48]. At the same time the energy resolution has to be good enough to preserve the excellent particle identification of the TPC via $\mathrm{d}E/\mathrm{d}x$.

To perform the measurements a dedicated mini TPC test setup was utilized. Figure 6.2(a) shows an exploded view of this setup. It has an anode pad readout that is lying on ground potential. Above, the four GEM foils are positioned. The foils are turned by 90° with respect to the previous one to prevent an exact alignment of the holes, which would increase the amount of back drifting ions. This is possible due to the hexagonal arrangement of the GEM holes. It also makes the measurements reproducible and not dependent on slight shifts of the foils' positions in the setup as the holes are always randomly misaligned. Above the GEM foils the drift volume is located. A field cage with three field stripes ensures a homogeneous drift field. On top the cathode is situated. Everything is housed in a gas tight aluminum vessel. The GEM electrodes, field stripes and the cathode are lying on successively increasing negative potential. There are two high voltage sockets in the aluminum box for each GEM foil, three for the field cage and one for the cathode. In the middle part of the aluminum body two gas connections are installed to enable a gas flow through the vessel. A ^{55}Fe gamma source can be attached to a flange on the side of the body.

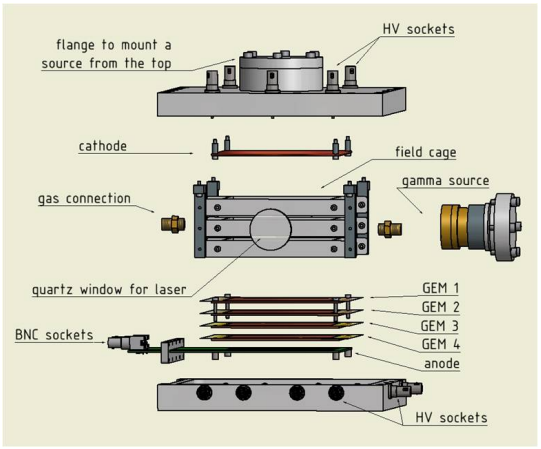

(a) Exploded view of the GEM TPC test setup.

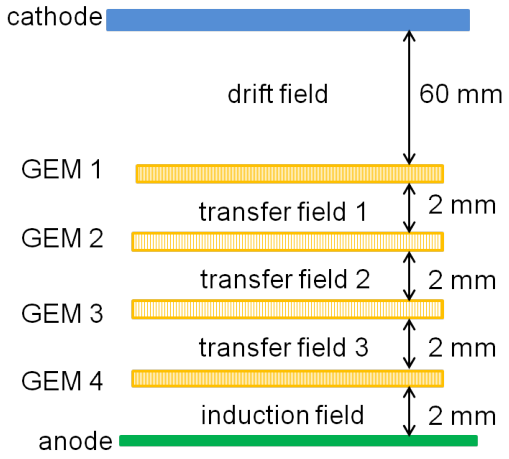

(b) Schematic diagram of a stack of four GEM foils.

Figure 6.2: Mini GEM TPC test setup.

Figure 6.2(b) shows a schematic diagram of the GEM stack. On the top one can see the cathode. Below there is the drift region which is 60 mm long. Afterwards the first

GEM is located. There is a distance of 2 mm between each GEM foil, as well as between the last GEM and the readout anode. The GEMs are numbered from 1 to 4 starting with the GEM closest to the drift volume. The fields between the foils are called transfer fields 1 to 4, also starting from the one closest to the drift volume. Transfer field 4, between GEM 4 and the anode, is also called induction field.

The chamber was flushed with Ne-CO_2-N_2 (90-10-5), as it was found in previous measurements, that Ar-CO_2 (90-10) as drift gas results in a much worse energy resolution in quadruple GEM stacks [89]. The gamma radiation from the source ionizes the gas in the drift volume and the created electrons drift towards the GEMs, where they are amplified. The drift field is set to 400 V/cm as this is the drift field of the ALICE TPC. The amplified electrons are measured on the anode, while the back drifting ions are measured on the cathode. The ratio of these two currents is the IBF:

$$IBF = \frac{I_{\text{cathode}}}{I_{\text{anode}}} \tag{6.1}$$

The anode current was measured with a Keithley electrometer, which determined the voltage drop relative to ground potential. To measure the small cathode currents an especially for this purpose designed picoamperemeter was used, as the cathode was lying on a high voltage of up to more than 6000 V. To measure the energy resolution of the ^{55}Fe peak the signal of one anode pad was directed via a pre amplifier and an amplifier to an ADC. Then it was displayed graphically and fitted with a Gaussian function. With peak position and full width at half maximum (FWHM) the energy resolution was calculated.

The goal of the measurements was to receive an IBF smaller than 1 % and at the same time an energy resolution of the ^{55}Fe peak $\sigma(^{55}\text{Fe})$ of at least 12 %. Therefore the GEM voltages and transfer fields between the GEMs, as well as the GEM foil types could be varied. With GEM voltage the voltage difference between the GEM's top and bottom electrode is meant. As known from previous measurements, IBF and energy resolution show opposing trends [89]. Therefore a compromise between both had to be found such that both criteria are satisfied.

Seven different quadruple GEM configurations were characterized. Transfer fields 1 (E_{T1}) and 4 (E_{T4}) were kept at 4000 V/cm, as this showed the best performance. This makes sense, as after the first GEM a large transfer field is favourable to extract as many electrons as possible coming from the drift volume to not lose too much information, which results in a bad energy resolution. After the last GEM foil no ions are produced anymore, so the electrons just have to be transferred as efficient as possible to the readout anode. On trend it is better to have most of the amplification in the lower GEM foils, as the possibility for the created ions is then larger to get caught by a GEM further up.

However, one has to be careful not to lose too much energy resolution, if the voltages of the first two GEMs are too low. At the same time a LP foil on first position is very detrimental and also leads to a bad energy resolution, as then too many field lines from the drift field end on the top electrode of GEM 1.

Systematic scans of transfer field 2 (E_{T2}) and transfer field 3 (E_{T3}) between 100 and 4000 V/cm have been performed for the different GEM configurations to find the setting where IBF and energy resolution show the best result. The voltages of GEM 1 (U_{GEM1}) and GEM 2 (U_{GEM2}) were kept constant for these scans. GEM 3 and GEM 4 voltages (U_{GEM3} and U_{GEM4}) were adjusted to obtain a gas gain of 2000 by keeping the ratio at 0.8.

After the working point for the transfer fields was found, they were fixed at this values and the GEM 1 and GEM 2 voltages were scanned determining IBF and energy resolution.

The statistical uncertainties on the measurements are negligible. The systematic uncertainty is about 5 % on the IBF, coming from the reading error of the anode current on the Keithley electrometer, but mainly of the small cathode current on the picoamperemeter. The systematic uncertainty on the energy resolution is about 2 %, which is ascribed to slight fluctuations in the peak position and width.

Figure 6.3 shows a scan of E_{T2} and E_{T3} exemplarily for the S-LP-LP-S GEM configuration. On the left plot one can see the IBF, on the right the energy resolution. U_{GEM1} was fixed at 270 V and U_{GEM2} at 230 V. For this configuration the working point for the transfer fields is lying in the lower right corner, where the IBF is 0.65 % and the energy resolution 12.6 %. This means $E_{T2} = 4000$ V/cm and $E_{T3} = 100$ V/cm.

Figure 6.4 shows a scan of E_{T2} and E_{T3} for the S-S-LP-SP GEM configuration. U_{GEM1} and U_{GEM2} were fixed at 230 V. For this configuration the working point for the transfer fields is lying in the upper left corner, where the IBF is 0.81 % and the energy resolution 12.7 %. So, $E_{T2} = 100$ V/cm and $E_{T3} = 4000$ V/cm shows the best performance.

In table 6.1 the optimized transfer-field settings determined from the E_{T2}-E_{T3} scans for the different GEM configurations are stated. One can see that the GEM foil on the second position (i.e. S or LP) determines the E_{T2}-E_{T3} scan. In the case that GEM 2 is a LP foil a large E_{T2} and small E_{T3} is favored and in the case that GEM 2 is a S foil vice versa.

Afterwards U_{GEM1}-U_{GEM2} scans have been performed, as shown in figure 6.5 exemplarily for the S-LP-S-S configuration. One can see that small GEM 1 and GEM 2 voltages result in the best IBF (0.33 %), as most of the amplification is done in the lower GEM layers, where the created ions can be blocked by the GEMs further up. However, this

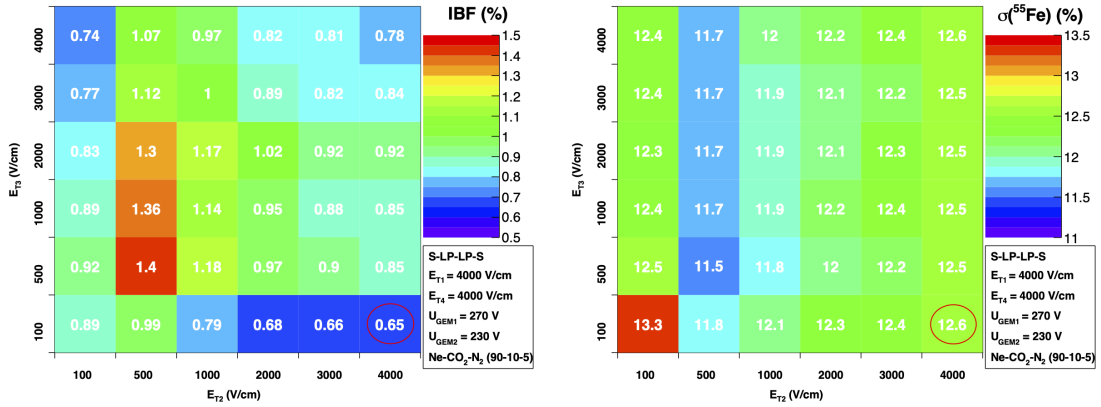

(a) IBF. (b) $\sigma(^{55}\mathrm{Fe})$.

Figure 6.3: Scan of transfer field 2 and 3 for the S-LP-LP-S GEM configuration.

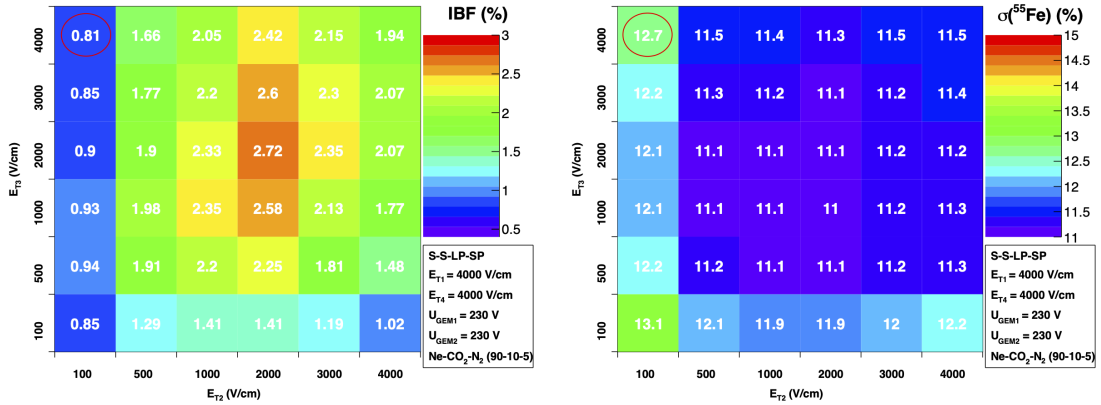

(a) IBF. (b) $\sigma(^{55}\mathrm{Fe})$.

Figure 6.4: Scan of transfer field 2 and 3 for the S-S-LP-SP GEM configuration.

also results in a bad energy resolution (17.6 %) as too much information of the electrons coming from the drift volume gets lost. Nevertheless, there are also voltage settings that meet the requirements, i.e. the IBF is below 1 % and the energy resolution below 12 %.

This can be visualized better by plotting IBF versus energy resolution, as can be seen in figure 6.6 for the seven characterized GEM configurations. Each curve represents a GEM 1 voltage scan at a fixed GEM 2 voltage. From the U_{GEM1}-U_{GEM2} scans one gets several of these curves for each GEM configuration, but in figure 6.6 only the best one for each configuration is shown. One can see that an operational point where the energy

Table 6.1: Optimized transfer-field settings for the different GEM configurations determined from the E_{T2}-E_{T3} scans. Also stated is the GEM 4 voltage, i.e. the highest voltage in the stack.

GEM config.	E_{T1} (V/cm)	E_{T2} (V/cm)	E_{T3} (V/cm)	E_{T4} (V/cm)	U_{GEM4} (V)
S-LP-LP-S	4000	4000	100	4000	353
S-LP-LP-SP	4000	4000	100	4000	361
S-S-LP-SP	4000	100	4000	4000	342
S-S-LP-S	4000	100	4000	4000	337
S-LP-S-S	4000	4000	100	4000	371
S-LP-S-SP	4000	4000	100	4000	376
S-S-S-S	4000	100	4000	4000	394

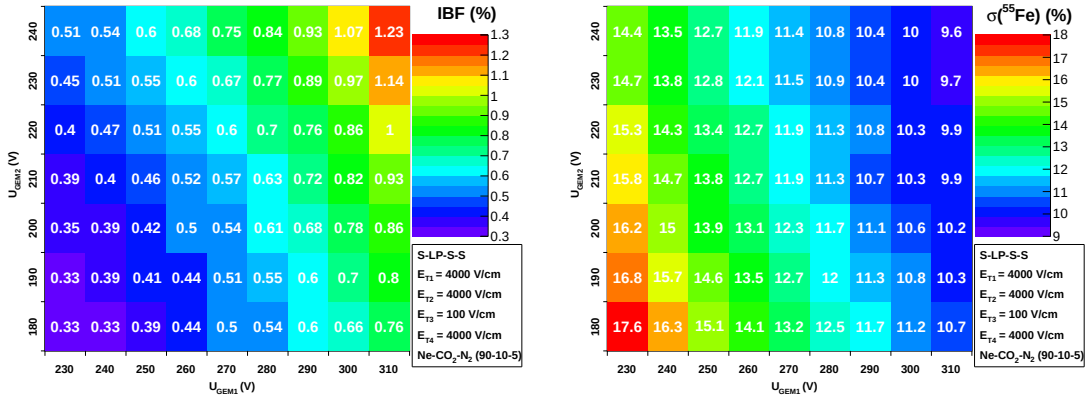

(a) IBF.

(b) $\sigma(^{55}\text{Fe})$.

Figure 6.5: Scan of GEM 1 and GEM 2 voltage for the S-LP-S-S GEM configuration.

resolution is about 12 % and the IBF is between 0.5 and 1 % can be found with various quadruple GEM configurations. The lowest IBF of below 0.6 % at 12 % energy resolution is provided by the S-LP-S-S configuration, though.

In table 6.1 the GEM 4 voltage of the voltage setting with the best IBF at an energy resolution of about 12 % is shown for each configuration. The GEM 4 voltage is the highest voltage in the GEM stack and a measure for the high-voltage stability of the system. One can see that for the systems with better IBF and σ performance in figure 6.6 the GEM 4 voltage is usually higher than for the systems with larger IBF, thus they presumably have a higher discharge probability.

The GEM configuration that is finally used in the upgraded ALICE TPC, is the S-LP-LP-S configuration. It is shown in black in figure 6.6 and well fulfilling the requirements

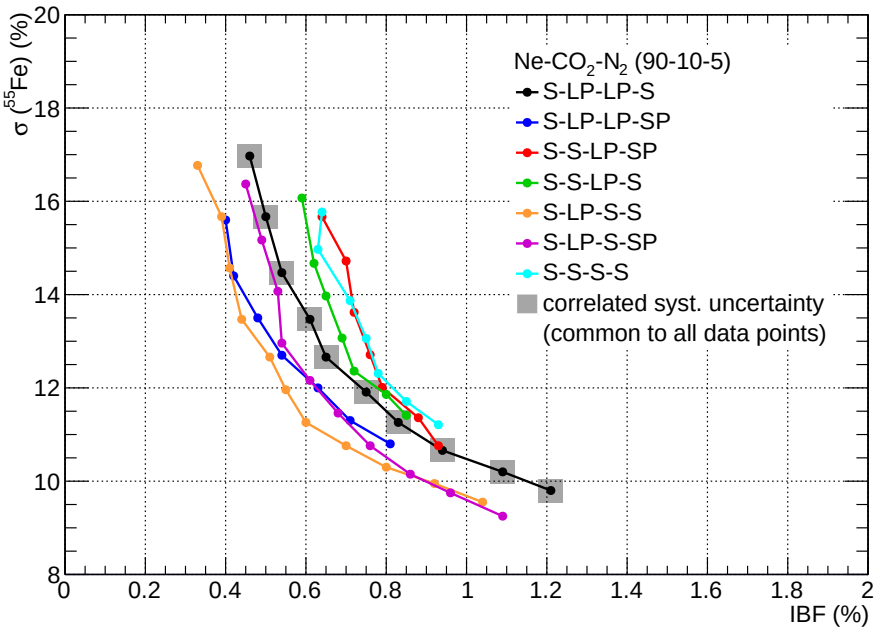

Figure 6.6: IBF versus energy resolution for the different GEM configurations. Each curve shows a GEM 1 voltage scan with fixed GEM 2 voltage. GEM 3 and GEM 4 voltages are adjusted to obtain a gain of 2000, by keeping their ratio at 0.8.

with an IBF of about 0.7 % at an energy resolution of 12 %.

There are three configurations that show a better performance in figure 6.6, however, they all have a larger GEM 4 voltage than the S-LP-LP-S configuration. In addition, two of the configurations employ a SP foil. SP foils have a smaller hole distance of only 90 μm and are not suitable for serial production of large size foils, which are needed for the ALICE TPC. The S-LP-S-S configuration looks very promising, though. At lower GEM 4 voltages it still showed better IBF values than the S-LP-LP-S configuration, so it could have been the better choice.

However, at the time of these measurements for the S-LP-LP-S configuration already detailed stability and discharge probability studies had been performed [90]. Thus it was decided to stay with this configuration, which also showed a very good performance.

The high-voltage settings for the optimal operation in the ALICE TPC feature a low transfer field 3 of 100 V/cm and a high transfer field 2. That this yields the best performance was also the result of this characterization (see figure 6.3). The ions that are produced in GEM 4 are mainly captured on the GEM 4 top electrode, due to the low field above. The two LP foils in the middle of the stack with misaligned holes, as they

are turned by 90° with respect to each other, further block the ions from drifting back in the drift volume. The transfer fields 1, 2 and 4, however, are set to 3500 V/cm instead of 4000 V/cm. The reason for that is an improvement of the stability of the system. As the absolute high voltages of GEM stack and field cage up to the high-voltage electrode (cathode) are successively increasing, lower transfer fields in the GEM stack also result in lower overall voltages. At the same time, a decrease of the these transfer fields only slightly deteriorates the IBF. In the case of E_{T2} reducing the field from 4000 to 3000 V/cm only results in an increase of the IBF by less than 2 %, as can be seen in figure 6.3.

The quadruple-GEM-stack readout-chambers were successfully installed in the ALICE TPC during LS2 [90] and in October 2021 the first data with stable proton-proton beams of the upgraded LHC at a center-of-mass energy of 900 GeV was taken. The TPC showed an excellent performance, being the first ever built large-scale GEM TPC featuring continuous readout. In figure 6.7 one of the first event displays of the upgraded TPC with continuous readout is shown.

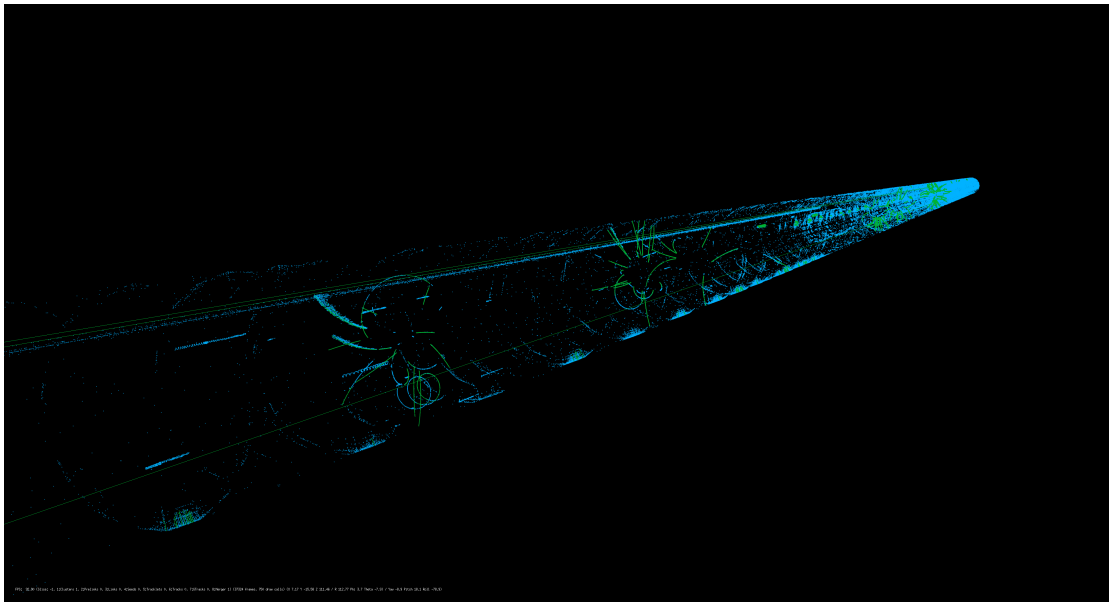

Figure 6.7: Event display of the GEM TPC with continuous readout.

In figure 6.8 the first performance figure of the upgraded GEM TPC can be seen showing the specific energy loss during the proton-proton pilot beam versus momentum. One can see that the different particle species are nicely separated and the desired $\mathrm{d}E/\mathrm{d}x$ resolution was reached.

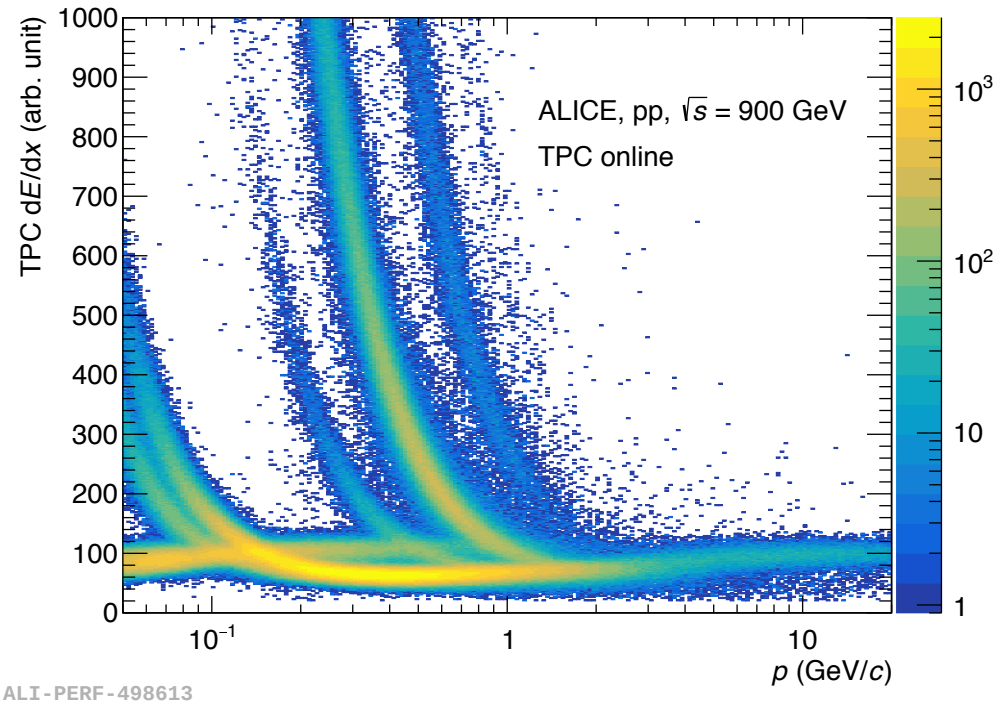

Figure 6.8: Specific energy loss versus momentum in the upgraded GEM TPC during the first pilot beam of the upgraded LHC in October 2021 [91].

7 Summary and conclusion

Shortly after the Big Bang a hot and dense medium, the quark-gluon plasma, filled the universe for a few microseconds. The QGP is a state of matter under extreme conditions, where quarks and gluons, the fundamental particles, are deconfined. The theory that describes strongly-interacting matter is the quantum chromodynamics which is part of the standard model of particle physics. The only possibility to create a QGP in the laboratory are heavy-ion collisions at ultrarelativistic energies. As also in the lab the QGP lives very shortly, it cannot be examined directly. Nevertheless, there are various observables that can be studied in the final state of the collisions. By comparing the data to model calculations, conclusions about the properties of the QGP can be drawn. The understanding today is that the QGP expands and cools down and when the critical temperature T_{c} is reached a crossover phase transition from the QGP to a hadron gas takes place. Shortly after, at the chemical freeze-out temperature T_{ch}, the inelastic interactions between the hadrons stop and the yields are fixed. Afterwards the particles still interact elastically until, at the kinetic freeze-out temperature T_{kin}, also the p_{T} spectra are fixed.

In a single heavy-ion collision thousands of particles are created. An experiment that is dedicated to measure particles created in heavy-ion collisions is ALICE at the Large Hadron Collider at CERN. The LHC is the largest particle accelerator in the world and reached up to now the highest center-of-mass energies of 5.02 TeV per nucleon-nucleon pair in Pb–Pb collisions. ALICE is equipped with a set of different particle detectors, working together and employing various techniques to obtain excellent tracking and particle-identification capabilities over a broad range of momentum to measure thousands of particles with high efficiency.

Among these particles are also light nuclei, however, they are produced very rarely. The amount of produced particles scales with the particle mass. In Pb–Pb collisions at the LHC an exponential decrease of the yield of light (anti)nuclei by a factor $\frac{1}{330}$ is observed by adding each additional nucleon. This factor is called penalty factor. In pp collisions the penalty factor is even $\frac{1}{1000}$. The abundances of particle species provide information about the particle-production mechanism at the transition from the QGP to a hadron gas. Light nuclei are of special interest as their size is a significant fraction of the

size of the created QGP and their binding energy is up to two orders of magnitude lower than the temperatures that govern the hadronic phase. So, it is still not understood how they can survive under these harsh conditions. There are two classes of models that describe the production of light (anti)nuclei, the statistical-hadronization model – also called thermal model – and the coalescence model. In the thermal model light (anti)nuclei are produced at the chemical freeze-out in statistical equilibrium with all other particles and the production depends exponentially on the particle mass. In the coalescence model nuclei are formed at the kinetic freeze-out by protons and neutrons that are nearby in space and have similar velocities. Here, the production depends on the size of the nuclei and the fireball. In this work comparisons of the data to both models were performed.

For this work about 270 million Pb–Pb collisions at $\sqrt{s_{\mathrm{NN}}} = 5.02\,\mathrm{TeV}$ measured by the ALICE collaboration in November 2018 were analyzed. The production of (anti)triton and (anti)^{4}He was studied. Due to their large mass both nuclei, but especially the (anti)^{4}He, are produced very rarely. So, the size of the available data set is very crucial. For this reason the analysis, that was first done in the Pb–Pb data set from 2015 was redone with the 2018 data set. In the complete data set from 2015 only 16 $^4\overline{\mathrm{He}}$ nuclei were identified. They are shown in an ALICE performance figure of the 2015 data set (figure 3.6). In the data set from 2018 about a factor ten more events in central Pb–Pb collisions were recorded. This made it possible to extract the first ever measured $^4\overline{\mathrm{He}}$ transverse-momentum spectrum. Also the first (anti)triton and ^{4}He transverse-momentum spectra in Pb–Pb collisions at the LHC were extracted.

The key aspect of these analyses is the particle identification to separate the light nuclei from the significantly more often produced other particles. In the TPC the specific energy loss of the particles is measured. At low momenta the different particle species are separated from each other, but from about $2\,\mathrm{GeV}/c$ the particles with a charge of one merge due to the relativistic rise and cannot be distinguished from each other in the TPC anymore. Therefore in addition the time-of-flight measurement is used, after the particles are selected in the TPC, to determine their mass. In the TOF measurement the (anti)triton signal is sitting on a huge background coming from mismatched tracks to the time measurement. Therefore the (anti)triton p_{T} spectra could only be extracted up to about $3\,\mathrm{GeV}/c$, which is also about the maximum of the p_{T} distribution. The (anti)triton spectra were extracted in four centrality intervals.

The (anti)^{4}He p_{T} spectra were only measured in the 0-10 % most central collisions as the recorded number of events were much smaller in the more peripheral centrality intervals. Due to its charge of two the (anti)^{4}He has a four times higher energy loss in the

TPC and is thus well separated from the particles with a charge of one. Nevertheless, also here the TOF measurement was necessary to distinguish the (anti)^{4}He from the (anti)^{3}He.

All p_{T} spectra, (anti)triton and (anti)^{4}He, were fitted with the Blast-Wave model and the kinetic freeze-out temperature and the expansion velocity of the fireball were extracted. In addition, the Blast-Wave fits were used to extrapolate to lower and higher p_{T} and determine the p_{T} integrated production yields $\mathrm{d}N/\mathrm{d}y$ and the mean transverse momentum $\langle p_{\mathrm{T}} \rangle$. For (anti)tritons both are increasing with collision centrality. In central Pb–Pb collisions two to three antitritons are produced every 10,000 collisions, and about one $^4\overline{\mathrm{He}}$ every 1,000,000 collisions. The $\langle p_{\mathrm{T}} \rangle$ is rising with particle mass and is thus larger for (anti)^{4}He than for (anti)triton.

The (anti)triton spectra, $\mathrm{d}N/\mathrm{d}y$ and $\langle p_{\mathrm{T}} \rangle$ were also compared to the ALICE preliminary (anti)^{3}He results and were found to be in good agreement as expected due to their similar mass.

A combined Blast-Wave fit of the p_{T} spectra of light particles up to light nuclei, namely π, K, p, d, ^{3}He, t, and ^{4}He, was performed. All p_{T} spectra including the light nuclei are described very well with a kinetic freeze-out temperature of $T_{\mathrm{kin}} = 98 \pm 1\,\mathrm{MeV}$ and an expansion velocity of the fireball of $\langle \beta \rangle = 0.661 \pm 0.003$ in central Pb–Pb collisions.

The p_{T}-integrated production yields $\mathrm{d}N/\mathrm{d}y$ of various particle species have been compared to different variants of the thermal model. The yields are described very well over nine orders of magnitude from the abundantly produced pions to the rarely produced (anti)^{4}He yielding a chemical freeze-out temperature of about 150 MeV for most models. The antitriton yield is described rather well. Also the ^{4}He yield is described very well, while the comparison to $^4\overline{\mathrm{He}}$ yields a $2.5\,\sigma$ discrepancy.

From the antiparticle-to-particle ratios of (anti)triton and (anti)^{4}He the baryochemical potential was calculated. Except for the (anti)tritons in the 0-10 % centrality interval, all ratios are compatible with one and the resulting baryochemical potentials are compatible with zero as expected at the LHC.

With the ratios of (anti)triton to (anti)^{3}He the isospin symmetry was cross-checked. Using the particle ratio the isospin symmetry is well conserved whereas the antiparticle ratio reveals a discrepancy due to the large antitriton yield in two p_{T} bins.

Also the ratio of the p_{T}-integrated production yield of nuclei to the proton yield in the same collision system and center-of-mass energy can be studied and compared to predictions of thermal and coalescence models. This was done for $A = 3$ nuclei (triton and ^{3}He) as a function of mean charged-particle multiplicity for different collision systems and centrality intervals. The overall trend of the data – first rising at low multiplicities

and then saturating at high multiplicities – is described by both models, so no model can be excluded so far. However, the antitriton-to-proton ratio is closer to the coalescence model.

Finally, coalescence parameters B_3 and B_4, which are related to the probability to form a nucleus via coalescence, were calculated. For (anti)tritons the coalescence parameters are smaller for central collisions – where the source size is larger – than for peripheral collisions. This makes sense, as in a small source volume the probability for the nucleons to come close to each other should be larger. The coalescence parameter of (anti)^{4}He is much smaller than the B_3, as it is less likely to form a nucleus the more nucleons are involved. Also B_3 and B_4 were compared to thermal and coalescence models. Here the data is a bit closer to the thermal model, but the overall trend is described by both models.

At the end of this thesis an outlook to the recently finalized TPC upgrade project was given. In the upcoming and very soon starting LHC Run 3 period the interaction rate will be increased to 50 kHz in Pb–Pb collisions. This will make it possible to gather more than 100 times the amount of data that was recorded in Run 2. The (anti)triton and (anti)^{4}He measurements will highly benefit from this gain in statistics. To cope with these high collision rates some major upgrades of the ALICE detector setup were irremissible. One of these upgrades was the exchange of the TPC's MWPCs with gating grid for quadruple-GEM-based readout-chambers which allow for a continuous readout. As the upgraded ALICE TPC is the first ever built large-scale GEM TPC, an extensive R&D program was necessary the characterize and test the GEM-based readout. As part of this R&D program in the beginning of this doctoral study a systematic investigation of ion backflow and energy resolution in quadruple GEM stacks using different types of GEM foils was performed on a dedicated mini TPC test setup. The aim was to reach an IBF of below 1 % at an energy resolution of at least 12 %. As these are competing requirements, a compromise had to be found in an extensive optimization campaign. It was possible to identify voltage settings for several GEM configurations, where both requirements were satisfied.

Bibliography

[1] P. Braun-Munzinger and J. Wambach. The Phase Diagram of Strongly-Interacting Matter. *Rev. Mod. Phys.*, 81:1031–1050, 2009.

[2] R. Vogt. *Ultrarelativistic Heavy-Ion Collisions*. Elsevier Science B.V., 2007.

[3] K. Fukushima and T. Hatsuda. The phase diagram of dense QCD. *Rept. Prog. Phys.*, 74:014001, 2011.

[4] J. Pochodzalla et al. Probing the nuclear liquid-gas phase transition. *Phys. Rev. Lett.*, 75:1040–1043, 1995.

[5] U. Heinz. 'RHIC serves the perfect fluid': Hydrodynamic flow of the QGP. In *Workshop on Extreme QCD*, pages 3–12, 2005.

[6] ALICE Collaboration. Centrality determination of Pb-Pb collisions at $\sqrt{s_{NN}} = 2.76$ TeV with ALICE. *Phys. Rev. C*, 88(4):044909, 2013.

[7] J. Bartke. *Introduction to Relativistic Heavy Ion Physics*. World Scientific Publishing, 2008.

[8] J. Jung. Dielectron production in pp collisions at $\sqrt{s} = 13\,\text{TeV}$ measured in a dedicated low magnetic-field setting with ALICE. Master's thesis, Goethe University Frankfurt, 2019.

[9] ALICE Collaboration. Glauber fit VZERO. `https://alice-figure.web.cern.ch/node/162`, 2012. ALICE Figure Repository.

[10] P. Braun-Munzinger and B. Dönigus. Loosely-bound objects produced in nuclear collisions at the LHC. *Nucl. Phys. A*, 987:144–201, 2019.

[11] E. Schnedermann, J. Sollfrank, and U. Heinz. Thermal phenomenology of hadrons from 200A GeV S+S collisions. *Phys. Rev. C*, 48:2462–2475, 1993.

[12] ALICE Collaboration. Production of light nuclei and anti-nuclei in pp and Pb-Pb collisions at energies available at the CERN Large Hadron Collider. *Phys. Rev. C*, 93(2):024917, 2016.

[13] P. Zyla et al. Review of Particle Physics. *PTEP*, 2020(8):083C01, 2020.

[14] X. Wang. *Quark–Gluon Plasma 5*. World Scientific Publishing, 2016.

[15] A. Bazavov et al. Equation of state in $(2+1)$-flavor QCD. *Phys. Rev. D*, 90:094503, 2014.

[16] A. Bazavov et al. Chiral crossover in QCD at zero and non-zero chemical potentials. *Phys. Lett. B*, 795:15–21, 2019.

[17] S. Borsanyi et al. QCD crossover at finite chemical potential from lattice simulations. *Phys. Rev. Lett.*, 125:052001, 2020.

[18] STAR Collaboration. Observation of the antimatter helium-4 nucleus. *Nature*, 473:353, 2011.

[19] ALICE Collaboration. Production of ^{4}He and $^4\overline{\mathrm{He}}$ in Pb–Pb collisions at $\sqrt{s_{\mathrm{NN}}}$=2.76 TeV at the LHC. *Nucl. Phys. A*, 971:1–20, 2018.

[20] A. Andronic, P. Braun-Munzinger, J. Stachel, and H. Stocker. Production of light nuclei, hypernuclei and their antiparticles in relativistic nuclear collisions. *Phys. Lett. B*, 697:203–207, 2011.

[21] P. Braun-Munzinger, K. Redlich, and J. Stachel. Particle production in heavy ion collisions. 2003. Appeared in Quark Gluon Plasma 3, eds. R.C. Hwa and Xin-Nian Wang, World Scientific Publishing.

[22] A. Andronic, P. Braun-Munzinger, K. Redlich, and J. Stachel. Hadron yields in central nucleus-nucleus collisions, the statistical hadronization model and the QCD phase diagram. *Acta Phys. Pol. B Proc. Suppl.*, 14:341–351, 2021.

[23] A. Andronic, P. Braun-Munzinger, and J. Stachel. Thermal hadron production in relativistic nuclear collisions: The Hadron mass spectrum, the horn, and the QCD phase transition. *Phys. Lett. B*, 673:142–145, 2009. [Erratum: Phys.Lett.B 678, 516 (2009)].

[24] A. Andronic, P. Braun-Munzinger, K. Redlich, and J. Stachel. Decoding the phase structure of QCD via particle production at high energy. *Nature*, 561(7723):321–330, 2018.

[25] F. Bellini and A. Kalweit. Testing production scenarios for (anti-)(hyper-)nuclei and exotica at energies available at the CERN Large Hadron Collider. *Phys. Rev. C*, 99(5), 2019.

[26] F. Bellini and A. Kalweit. Testing production scenarios for (anti-)(hyper-)nuclei with multiplicity-dependent measurements at the LHC. *Acta Phys. Pol. B*, 50(6):991, 2019.

[27] R. Scheibl and U. Heinz. Coalescence and flow in ultrarelativistic heavy ion collisions. *Phys. Rev. C*, 59:1585–1602, 1999.

[28] Minutes. Projet de Procès-verbal. 6th Session of the European Council for Nuclear Research. 1953. The document CERN/GEN/10 supersedes CERN/0052.

[29] E. Mobs. The CERN accelerator complex - 2019. Complexe des accélérateurs du CERN - 2019. 2019. General Photo.

[30] NobelPrize.org. Nobel Prize Outreach AB 2021. The nobel prize in physics 1984. `https://www.nobelprize.org/prizes/physics/1984/summary/`, 2021. [Online; accessed 29-October-2021].

[31] NobelPrize.org. Nobel Prize Outreach AB 2021. The nobel prize in physics 1992. `https://www.nobelprize.org/prizes/physics/1992/press-release/`, 2021. [Online; accessed 29-October-2021].

[32] ATLAS Collaboration. Observation of a new particle in the search for the Standard Model Higgs boson with the ATLAS detector at the LHC. *Phys. Lett. B*, 716:1–29, 2012.

[33] CMS Collaboration. Observation of a New Boson at a Mass of 125 GeV with the CMS Experiment at the LHC. *Phys. Lett. B*, 716:30–61, 2012.

[34] NobelPrize.org. Nobel Prize Outreach AB 2021. The nobel prize in physics 2013. `https://www.nobelprize.org/prizes/physics/2013/prize-announcement/`, 2021. [Online; accessed 29-October-2021].

[35] CERN. The birth of the web. `https://home.cern/science/computing/birth-web`, 2021. [Online; accessed 29-October-2021].

[36] L. R. Evans and P. Bryant. LHC Machine. *JINST*, 3:S08001. 164 p, 2008. This report is an abridged version of the LHC Design Report (CERN-2004-003).

[37] CERN. The large hadron collider — CERN accelerating science. `https://home.cern/science/accelerators/large-hadron-collider`, 2020. [Online; accessed 26-August-2020].

[38] CERN. Cryogenics: Low temperatures, high performance — CERN accelerating science. `https://home.cern/science/engineering/cryogenics-low-temperatures-high-performance`, 2020. [Online; accessed 27-August-2020].

[39] CERN. Accelerating: Radiofrequency cavities — CERN accelerating science. `https://home.cern/science/engineering/accelerating-radiofrequency-cavities`, 2020. [Online; accessed 26-August-2020].

[40] CERN. A vacuum as empty as interstellar space — CERN accelerating science. `https://home.cern/science/engineering/vacuum-empty-interstellar-space`, 2020. [Online; accessed 27-August-2020].

[41] Wikipedia. Large hadron collider — Wikipedia, die freie Enzyklopädie. `https://de.wikipedia.org/w/index.php?title=Large_Hadron_Collider&oldid=201051750`, 2020. [Online; Stand 21. August 2020].

[42] CERN. Cern's accelerator complex — CERN accelerating science. `https://home.cern/science/accelerators/accelerator-complex`, 2020. [Online; accessed 27-August-2020].

[43] CERN. The low energy ion ring — CERN accelerating science. `https://home.cern/science/accelerators/low-energy-ion-ring`, 2020. [Online; accessed 28-August-2020].

[44] A. Beuret et al. The LHC Lead Injector Chain. (LHC-Project-Report-776. CERN-LHC-Project-Report-776):4 p, 2004. revised version submitted on 2004-09-23 14:33:06.

[45] CERN. Lhc report: make way for the heavy ions — CERN accelerating science. `https://home.cern/news/news/accelerators/lhc-report-make-way-heavy-ions`, 2018. [Online; accessed 02-September-2020].

[46] ALICE Collaboration. The ALICE experiment at the CERN LHC. *Journal of Instrumentation*, 3(08):S08002–S08002, 2008.

[47] ALICE Collaboration. 3D ALICE Schematic RUN2 - with Description. `https://alice-figure.web.cern.ch/node/11218`, 2017. ALICE Figure Repository.

[48] ALICE Collaboration. Technical Design Report for the Upgrade of the ALICE Time Projection Chamber. 2014.

[49] ALICE Collaboration. ALICE DCal: An Addendum to the EMCal Technical Design Report Di-Jet and Hadron-Jet correlation measurements in ALICE. 2010.

[50] ALICE Collaboration. Calibration of the photon spectrometer PHOS of the ALICE experiment. *JINST*, 14(05):P05025, 2019.

[51] A. Tello. AD, the ALICE diffractive detector. *AIP Conference Proceedings*, 1819:040020, 2017.

[52] M. Broz et al. Performance of ALICE AD modules in the CERN PS test beam. 2020.

[53] W. Blum, W. Riegler, and L. Rolandi. *Particle Detection with Drift Chambers*. 1611-1052. Springer-Verlag, 2. edition, 2008.

[54] ALICE Collaboration. ITS pureSA dEdx VsP PbPb502. `https://alice-figure.web.cern.ch/node/9866`. ALICE Figure Repository.

[55] ALICE Collaboration. TOF Beta vs Momentum performance in Pb-Pb at 5.02 TeV (LHC15o). `https://alice-figure.web.cern.ch/node/9150`. ALICE Figure Repository.

[56] F. Sauli. GEM: A new concept for electron amplification in gas detectors. *Nucl. Instrum. Meth. A*, 386(2):531–534, 1997.

[57] ALICE Collaboration. Technical Design Report for the Upgrade of the ALICE Inner Tracking System. *Journal of Physics G: Nuclear and Particle Physics*, 41(8):087002, 2014.

[58] X. Wang and M. Gyulassy. HIJING: A Monte Carlo model for multiple jet production in pp, pA and AA collisions. *Phys. Rev.*, D44:3501–3516, 1991.

[59] R. Brun, F. Carminati, and S. Giani. GEANT Detector Description and Simulation Tool. *Program Library Long Write-up W5013*, 1994.

[60] S. Agostinelli et al. GEANT4: A Simulation toolkit. *Nucl. Instrum. Meth.*, A506:250–303, 2003.

[61] V. Uzhinsky, J. Apostolakis, A. Galoyan, G. Folger, V. Grichine, et al. Antinucleus-nucleus cross sections implemented in Geant4. *Phys. Lett. B*, 705:235–239, 2011.

[62] J. Heinrich. Coverage of Error Bars for Poisson Data. *CDF note*, 2003. CDF-6438.

[63] R. Barlow. Systematic errors: Facts and fictions. In *Conference on Advanced Statistical Techniques in Particle Physics*, 2002.

[64] ALICE Data Preparation Group. Analysis Object Tools - Systematic uncertainties on TPC-ITS matching in various Run-2 data samples. `https://twiki.cern.ch/twiki/bin/view/ALICE/AliDPGtoolsTrackSystematicUncertaintyBookkeping`.

[65] P. Larionov, M. Colocci, A. Kalweit, and M. Puccio. Measurement of $^3\overline{\mathrm{He}}$ inelastic cross-section in Pb-Pb collisions. `https://alice-notes.web.cern.ch/node/1106`, 2021. ALICE Analysis Note.

[66] A. Calivà. Private communication. July 2021.

[67] I. Vorobyev. Private communication. June 2021.

[68] ALICE Collaboration. Production of charged pions, kaons, and (anti-)protons in Pb-Pb and inelastic *pp* collisions at $\sqrt{s_{NN}} = 5.02$ TeV. *Phys. Rev. C*, 101(4):044907, 2020.

[69] ALICE Collaboration. Centrality dependence of the charged-particle multiplicity density at midrapidity in Pb-Pb collisions at $\sqrt{s_{\mathrm{NN}}} = 5.02$ TeV. *Phys. Rev. Lett.*, 116(22):222302, 2016.

[70] M. Puccio, S. Bufalino, and M. Masera. (Anti–)Nuclei production in Pb–Pb collisions at $\sqrt{s_{NN}} = 5.02$ TeV. `https://alice-notes.web.cern.ch/node/626`, 2017. ALICE Analysis Note.

[71] M. Puccio. Production of (anti-)(hyper-)nuclei at LHC energies with ALICE. *EPJ Web Conf.*, 171:14009, 2018.

[72] V. Vovchenko and H. Stoecker. Thermal-FIST: A package for heavy-ion collisions and hadronic equation of state. *Comput. Phys. Commun.*, 244:295–310, 2019.

[73] B. Dönigus. Light nuclei in the hadron resonance gas. *Int. J. Mod. Phys. E*, 29(05):2040001, 2020.

[74] M. Floris. Hadron yields and the phase diagram of strongly interacting matter. *Nucl. Phys. A*, 931:103–112, 2014.

[75] S. Wheaton and J. Cleymans. THERMUS: A Thermal model package for ROOT. *Comput. Phys. Commun.*, 180:84–106, 2009.

[76] S. Wheaton and J. Cleymans. Statistical-thermal model calculations using THERMUS. *J. Phys. G*, G31:S1069–S1074, 2005.

[77] V. Vovchenko, B. Dönigus, and H. Stoecker. Multiplicity dependence of light nuclei production at LHC energies in the canonical statistical model. *Phys. Lett. B*, 785:171–174, 2018.

[78] V. Vovchenko, M. Gorenstein, and H. Stoecker. Finite resonance widths influence the thermal-model description of hadron yields. *Phys. Rev. C*, 98(3):034906, 2018.

[79] G. Torrieri, S. Steinke, W. Broniowski, W. Florkowski, J. Letessier, et al. SHARE: Statistical hadronization with resonances. *Comput. Phys. Commun.*, 167:229–251, 2005.

[80] G. Torrieri, S. Jeon, J. Letessier, and Johann Rafelski. SHAREv2: Fluctuations and a comprehensive treatment of decay feed-down. *Comput. Phys. Commun.*, 175:635–649, 2006.

[81] M. Petran, J. Letessier, J. Rafelski, and G. Torrieri. SHARE with CHARM. *Comput. Phys. Commun.*, 185:2056–2079, 2014.

[82] B. Dönigus. Private communication. October 2021.

[83] J. Cleymans, S. Kabana, I. Kraus, H. Oeschler, K. Redlich, and N. Sharma. Antimatter production in proton-proton and heavy-ion collisions at ultrarelativistic energies. *Phys. Rev. C*, 84:054916, 2011.

[84] U. Heinz, P. Subramanian, H. Stoecker, and W. Greiner. Formation of Antimatter Clusters in the Hadronization Phase Transition. *J. Phys. G*, 12:1237, 1986.

[85] W. Greiner. Fundamental issues in the physics of elementary matter: Cold valleys and fusion of superheavy nuclei - hypernuclei - antinuclei - correlations in the vacuum. *AIP Conf. Proc.*, 597(1):3, 2001.

[86] D. Griffiths. *Introduction to Elementary Particles (2nd ed.)*. Wiley-VCH, 2008.

[87] P. Braun-Munzinger, K. Redlich, and J. Stachel. *invited review in: R.C. Hwa, X.N. Wang Eds., Quark Gluon Plasma, vol. 3, World Scientific Publishing,* . World Scientific Publishing, 2003. arXiv:nucl-th/0304013.

[88] K. Sun, C. Ko, and B. Dönigus. Suppression of light nuclei production in collisions of small systems at the Large Hadron Collider. *Phys. Lett. B*, 792:132–137, 2019.

[89] E. Bartsch. Charakterisierung einer GEM-basierten Auslese für die ALICE TPC. Master's thesis, Goethe University Frankfurt, 2014.

[90] ALICE TPC Collaboration. The upgrade of the ALICE TPC with GEMs and continuous readout. *JINST*, 16(03):P03022, 2021.

[91] ALICE Collaboration. ALICE TPC dE/dx performance - Online QC - Pilot beams 2021. `https://alice-figure.web.cern.ch/node/20827`. ALICE Figure Repository.